iScience

CellPress
OPEN ACCESS

Article

Overexpression of the schizophrenia risk gene C4 in PV cells drives sex-dependent behavioral deficits and circuit dysfunction

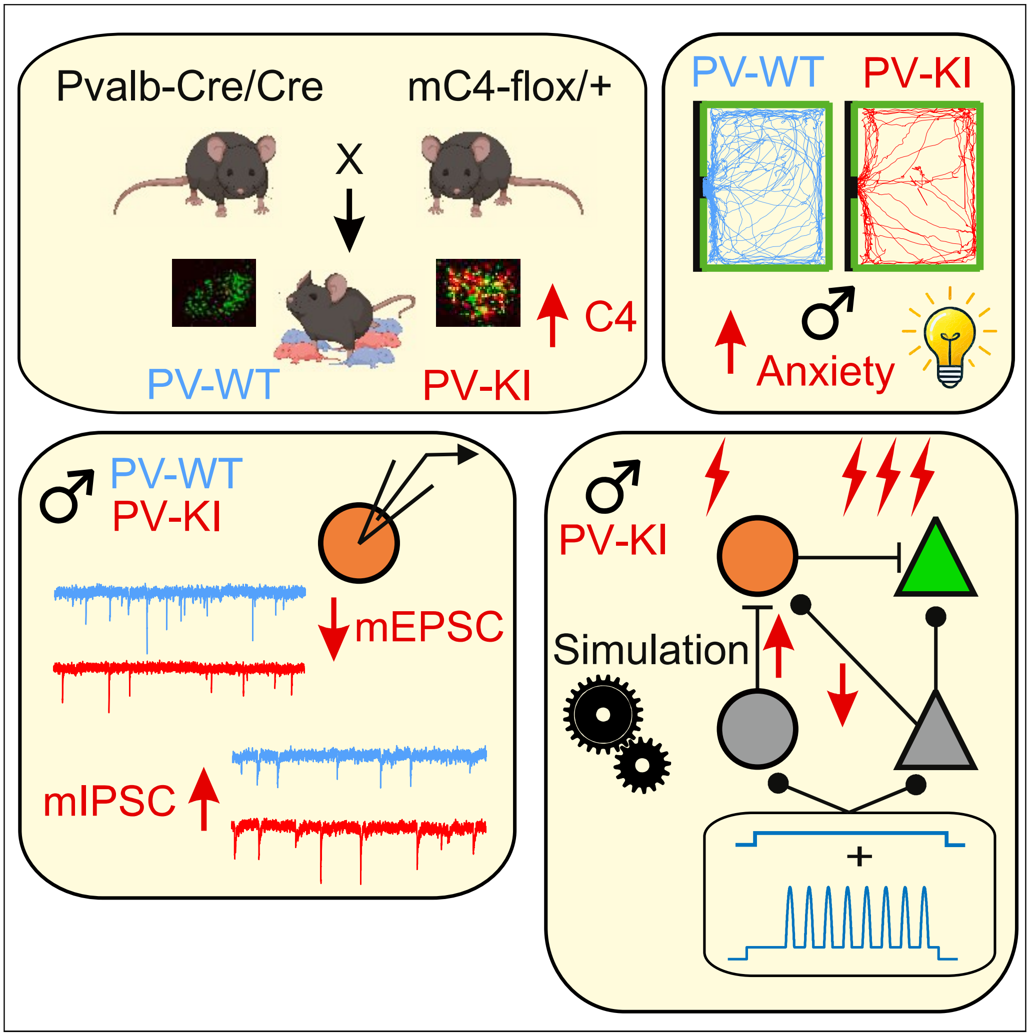

Luke A. Fournier, Rhushikesh A. Phadke, Maria Salgado, ..., Nicole M. Padró Luna, Kamal Sen, Alberto Cruz-Martín

alberto.cruzmartin@cuanschutz.edu

Highlights

- A novel mouse line permits the conditional overexpression (OE) of the SCZ risk gene, C4
- PV cell-specific OE of C4 drives anxiety-like behavior in male but not female mice
- Behavioral deficits accompanied reduced excitation and increased inhibition to PV cells
- Computational model exhibits hyperactivity and disrupted neural communication

Fournier et al., iScience *27*, 110800
September 20, 2024
https://doi.org/10.1016/j.isci.2024.110800

iScience

CellPress
OPEN ACCESS

Article

Overexpression of the schizophrenia risk gene C4 in PV cells drives sex-dependent behavioral deficits and circuit dysfunction

Luke A. Fournier,[1] Rhushikesh A. Phadke,[2] Maria Salgado,[1] Alison Brack,[2] Jian Carlo Nocon,[3,4,5,6]
Sonia Bolshakova,[1,7] Jaylyn R. Grant,[8,9] Nicole M. Padró Luna,[9,10] Kamal Sen,[3,4,5,6]
and Alberto Cruz-Martín[1,2,11,12,13,14,*]

SUMMARY

Fast-spiking parvalbumin (PV)-positive cells are key players in orchestrating pyramidal neuron activity, and their dysfunction is consistently observed in myriad brain diseases. To understand how immune complement pathway dysregulation in PV cells drives disease pathogenesis, we have developed a transgenic line that permits cell-type specific overexpression of the schizophrenia-associated *C4* gene. We found that overexpression of mouse *C4* (*mC4*) in PV cells causes sex-specific alterations in anxiety-like behavior and deficits in synaptic connectivity and excitability of PFC PV cells. Using a computational model, we demonstrated that these microcircuit deficits led to hyperactivity and disrupted neural communication. Finally, pan-neuronal overexpression of mC4 failed to evoke the same deficits in behavior as PV-specific mC4 overexpression, suggesting that perturbations of this neuroimmune gene in fast-spiking neurons are especially detrimental to circuits associated with anxiety-like behavior. Together, these results provide a causative link between C4 and the vulnerability of PV cells in brain disease.

INTRODUCTION

Cortical parvalbumin (PV)-positive fast-spiking cells are a distinct class of inhibitory neurons characterized by their expression of the Ca^{2+}-binding protein, PV.[1–3] Their unique biophysical properties allow them to drive potent, precise inhibition, effectively controlling the temporal dynamics of the excitatory and inhibitory inputs[4–6] that support critical brain functions.[7–9] At a network level, PV cells are responsible for generating and regulating gamma oscillations,[10] 30–80 Hz rhythmic fluctuations in brain activity that correlate with cognitive performance[11–13] and are impaired in anxiety disorders,[14] schizophrenia (SCZ),[15,16] and Alzheimer's disease (AD).[17,18] Besides controlling the temporal dynamics of excitation and inhibition and orchestrating oscillatory activity, PV neuron activity tightly regulates cortical maturation during critical developmental windows.[19–21]

Despite significant progress in understanding PV cell function in the healthy and diseased brain, it remains to be determined how specific genetic alterations associated with neuropsychiatric disorders lead to the dysfunction of inhibitory microcircuits. It is also unclear whether particular circuitry or synaptic inputs underlying the function of PV cells are susceptible to disease-associated genetic alterations. For example, in postmortem tissue of patients with SCZ, the density of excitatory synapses is decreased on PV cells with concomitant downregulation of PV and other inhibitory markers,[22–25] suggesting that excitatory drive to fast-spiking cells is compromised in this brain disorder. Moreover, SCZ-associated genetic alterations have been found to disrupt the molecular machinery underlying feedforward excitatory inputs to PV neurons,[26–28] suggesting these particular connections are susceptible to genetic perturbations.

---

[1] Neurobiology Section in the Department of Biology, Boston University, Boston, MA, USA
[2] Molecular Biology, Cell Biology & Biochemistry Program, Boston University, Boston, MA, USA
[3] Neurophotonics Center, Boston University, Boston, MA, USA
[4] Center for Systems Neuroscience, Boston University, Boston, MA, USA
[5] Hearing Research Center, Boston University, Boston, MA, USA
[6] Department of Biomedical Engineering, Boston University, Boston, MA, USA
[7] Bioinformatics MS Program, Boston University, Boston, MA, USA
[8] Biological Sciences, Eastern Illinois University, Charleston, IL, USA
[9] The Summer Undergraduate Research Fellowship (SURF) Program, Boston University, Boston, MA, USA
[10] Biology Department, College of Natural Sciences, University of Puerto Rico, Rio Piedras Campus, San Juan, PR, USA
[11] Department of Anesthesiology, University of Colorado Anschutz Medical Campus, Aurora, CO, USA
[12] NeuroTechnology Center (NTC), University of Colorado Anschutz Medical Campus, Aurora, CO, USA
[13] Neuroscience Graduate Program, University of Colorado Anschutz Medical Campus, Aurora, CO, USA
[14] Lead contact
*Correspondence: alberto.cruzmartin@cuanschutz.edu

https://doi.org/10.1016/j.isci.2024.110800

The association between the major histocompatibility complex (MHC) and SCZ could provide a link between immune dysfunction and the disruption of molecular mechanisms that regulate the wiring of synaptic circuits.[29–32] In support of this, Sekar et al.[33] showed that mice that lack *C4b* (*mouse C4*, *mC4*), which in humans is harbored in the MHC locus, exhibit deficits in the developmental refinement of retinogeniculate synapses. Furthermore, Comer et al.[34] demonstrated that increasing levels of the human (*C4A*) and mouse *C4* homologs in layer (L) 2/3 pyramidal neurons (PYRs) of the medial prefrontal cortex (mPFC)—a brain region associated with the pathology of SCZ[35–37] and other neuropsychiatric conditions[38–40]—led to pathological synaptic loss during early postnatal development and social behavioral deficits in mice. This research and similar investigations that also find C4-driven loss of excitatory synapses[41,42] suggest a link between immune dysfunction and brain disorders, particularly SCZ, through the role of the MHC and its impact on synaptic development and plasticity.

As a consequence of their unique properties and role in controlling network function, PV cells exhibit high metabolic demands, which make them vulnerable to oxidative stress and neuroimmune dysregulation[43–47]; these pathological processes are linked to brain disorders.[48–50] Therefore, determining the molecular pathways through which immune imbalances can impact PV neuron function offers significant potential for unraveling neurodevelopmental disease etiology. Despite this, there is a notable gap in the availability of models to determine how neuroimmune dysfunction alters specific brain circuitry. In the same vein, alterations in the complement pathway have been linked to the pathology of brain disorders.[51] However, it remains an open question whether particular brain cell types are especially vulnerable to complement dysfunction.

Here, we developed and validated a novel mouse line that permits cell-type specific overexpression of mC4 (mC4-OE). Utilizing this unique knock in transgenic mouse, we demonstrate that increased mC4 levels in PV cells (PV-mC4-OE) drive pathological anxiety-like behaviors in male, but not female mice. In both sexes, PV-mC4-OE led to changes in a subclass of social interaction, indicating that elevated expression of this immune gene in fast-spiking cells disrupts the circuitry governing social behaviors. We used electrophysiology to show that excitatory and inhibitory inputs to mPFC PV cells are altered with increased levels of mC4 in male, but not female mice, mirroring the sexually dimorphic anxiety-like behavior.

Elevated mC4 in PV neurons had differing impacts on cortical cell excitability: hypoexcitability in male fast-spiking cells and PYRs, as opposed to enhanced excitability in female fast-spiking cells. In contrast to PV-cell-specific effects of mC4-OE, increased mC4 levels in all neurons had no effects on anxiety-like behavior nor the excitatory drive to PV neurons, supporting the vulnerability of C4 perturbations specifically in this susceptible cell type. Finally, using a computational model, we demonstrated that deficits in the PV-mC4-OE-driven inhibitory microcircuit disrupt model pyramidal neuron communication and cause hyperexcitability within the male model network, illustrating how the interaction of cellular and synaptic traits generates complex sex-dependent neural network deficits in disease states.

In summary, our results show that mC4 dysregulation in PV neurons led to alterations in anxiety-like behavior in male mice, which were associated with mPFC circuit dysfunction. Our results provide crucial insights into the molecular interplay between cell-type-specific increased levels of mC4, defects in mPFC circuitry, and abnormal behavior associated with the prefrontal cortex.

RESULTS

A novel transgenic mouse line permits PV cell-specific overexpression of complement component 4

We generated a tunable conditional transgenic mouse based on a design by Dolatshad et al.[52] to reliably drive overexpression (OE) of mC4 (mC4-OE) in specific cell types, and to incorporate genetic recombination switches that allow the conversion of different OE alleles for tunable transgene expression (Figure 1A). Comer et al.[34] showed that mPFC neurons in postnatal day (P) 30 control mice express low levels of *C4b* transcript, which were not present in tissue from *C4b* knock-out mice.[53]

To achieve specific OE of mC4 in parvalbumin (PV)-positive cells (PV-mC4-OE) under the strong CAG promoter,[54,55] we crossed PV-Cre mice with the conditional mC4-OE KI mouse line, mC4-KI mice (Figures 1A and 1B). We generated litters that consisted of a mixture of pups that either inherited the floxed mC4-KI allele and thus overexpressed mC4 specifically in PV cells (PV-mC4-KI or KI) or did not inherit the floxed mC4-KI allele and were used as a wild type littermate control (PV-mC4-WT, or WT) (Figure 1B). To control for effects of Cre-recombinase expression,[56,57] we crossed homozygous PV-Cre mice to heterozygous mC4-KIs to obtain Cre recombinase expression in all offspring (Figure 1B). We focused on a P40-60 temporal window, roughly equivalent to the young-adult life stage that immediately precedes SCZ symptom onset.[58] PV-mC4-OE did not lead to observable health or locomotor deficits, as measured via weight (Figure 1C) and distance traveled (Figure 1D). Moreover, the density of PV cells was not significantly changed in PV-mC4-KI mice, compared to controls (Figures 1E–1G).

Next, we used multiplex fluorescence *in situ* hybridization (M-FISH) in the mPFC of WT and KI mice (Figures 1H–1L). At P21, we observed a significant increase in the number of *mC4* mRNA puncta in PV cells in PV-mC4-KI mice, indicating reliable mC4-OE in this interneuron type (Figure 1I). We did not observe an increase in *mC4* puncta in neighboring somatostatin (SST)-positive cells and non-PV- non-SST-expressing cells ("Other"), suggesting that our genetic approach led to specific mC4-OE in PV cells (Figure 1I). In PV-mC4-KI mice, the number of *mC4* puncta in PV cells was not different between P21 and 65 (Figures 1I and 1J), indicating that we achieved stable OE across development. Additionally, other cell types did not show differences in *mC4* expression compared to WT mice, indicating cell-type-specific maintenance of the OE into adulthood (Figures 1I and 1J). Finally, quantification of *PV* mRNA puncta revealed that PV-mC4-OE did not drive any significant changes in the number of *PV* puncta per cell at either P21 (Figure 1K) or P65 (Figure 1L), suggesting that *PV* expression was not altered by increased levels of mC4 in this cell type.

In summary, we have developed and validated a novel conditional mouse model that, when combined with cre-driver lines, facilitates the study of distinct cellular sources of mC4 overexpression. These results also indicate that we can reliably and specifically overexpress mC4 in PV cells and that transgenic mice are devoid of gross motor or health defects.

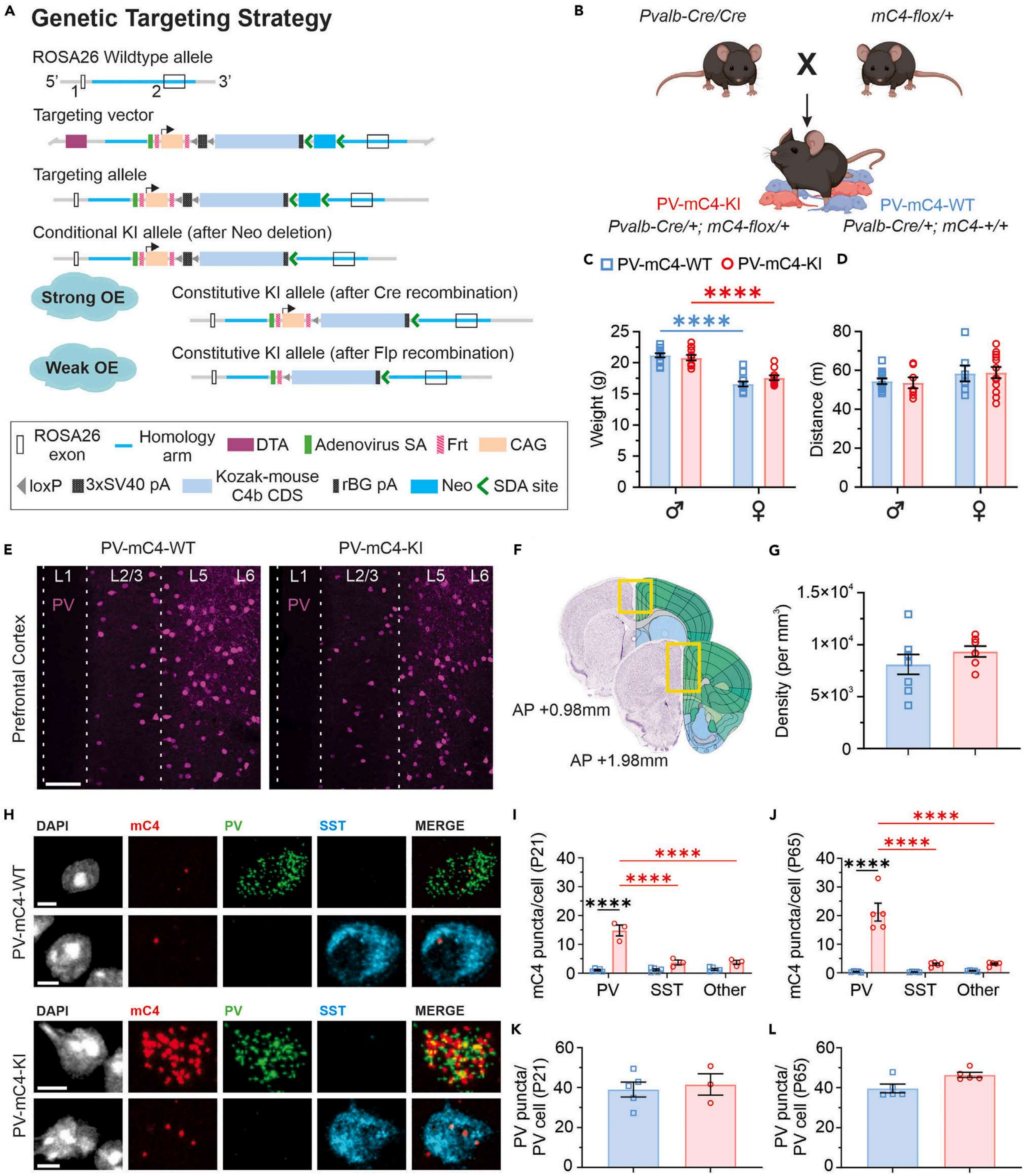

Figure 1. A novel transgenic mouse line permits PV cell-specific overexpression of complement component 4

(A) Genetic strategy. Positive selection marker (*Neo*), self-deletion anchor (SDA) sites. Diphtheria toxin A (DTA) sites. The constitutive KI allele can be obtained after Cre- or Flp-mediated recombination, yielding relatively strong or weak OE of mC4, respectively.

(B) Breeding scheme.

Figure 1. *Continued*

(C) Increased levels of mC4 in PV cells did not alter mouse weights compared to controls (condition x sex: $F[_{1,44}] = 3.204$, $p = 0.0803$. Condition: $F[_{1,44}] = 0.6311$, $p = 0.4312$. Sex: $F[_{1,44}] = 103.2$, ****$p < 0.0001$. Post-test: WT vs. KI males, $p = 0.9793$, WT, $N = 13$, KI, $N = 12$; females, $p = 0.3947$, WT, $N = 12$, KI, $N = 11$). For both WT and KI mice, males weighed more than females (WT males vs. females, ****$p < 0.0001$, KI males vs. females, ****$p < 0.0001$).

(D) OE of mC4 in PV cells did not impact the distance traveled in an open field (condition x sex: $F[_{1,34}] = 0.04903$, $p = 0.8261$. Condition: $F[_{1,34}] = 0.004672$, $p = 0.9459$. Sex: $F[_{1,34}] = 2.657$, $p = 0.1123$. Males: WT, $N = 12$, KI, $N = 7$. Females: WT, $N = 7$, KI, $N = 12$).

(E) Representative confocal images of PV cells (*magenta*) in mouse mPFC in P55-74 WT (*left*) and KI (*right*) animals, *scale bar*, 100 μm. L, layer.

(F) mPFC PV cell density, yellow box. Bregma coordinates. AP, anterior-posterior axis.

(G) No difference in PV cell density between WT and KI (Mann-Whitney test, $p = 0.2319$, WT, $N = 8$, KI $N = 7$).

(H, *top two rows*) Representative confocal images (40x) of a PV (first row) and somatostatin (SST) cell (second row) in a WT mouse. (H, *bottom two rows*) Representative confocal images (40x) of a PV (first row) and SST cell (second row) in a KI mouse. For all rows in H, *left to right*: DAPI (*gray*), mC4 (*red*), PV (*green*), SST (*cyan*), merged image without DAPI. *scale bar*, 5 μm.

(I) In P21 KI mice, *mC4* was overexpressed in PV, but not in SST or all other DAPI-labeled cells. (Condition x cell-type: $F[_{2,18}] = 41.62$, ****$p < 0.0001$. Condition: $F[_{1,18}] = 113.7$, ****$p < 0.0001$. Cell-type: $F[_{2,18}] = 38.22$, ****$p < 0.0001$. Post-test: WT vs. KI: PV, ****$p < 0.0001$, SST, $p = 0.1793$, neighboring non-PV cell or non-SST cell [Other], $p = 0.2166$). In P21 KI mice, *mC4* expression was significantly greater in PV cells than in SST cells (PV vs. SST, ****$p < 0.0001$) and all other DAPI-labeled cells (PV vs. Other, ****$p < 0.0001$). P21 WT, $N = 5$, KI, $N = 3$.

(J) In P65 mice, *mC4* was overexpressed in PV, but not in SST or all other DAPI-labeled cells (condition x cell-type: $F[_{2,24}] = 33.42$, ****$p < 0.0001$. Condition: $F[_{1,24}] = 66.63$, ****$p < 0.0001$. Cell-type: $F[_{2,24}] = 32.59$, ****$p < 0.0001$. Post-test: WT vs. KI: PV, ****$p < 0.0001$, SST, $p = 0.6948$, Other, $p = 0.7839$). In P65 KI mice, *mC4* expression was significantly greater in PV cells than in SST cells (PV vs. SST, ****$p < 0.0001$) and all other DAPI-labeled cells (PV vs. Other, ****$p < 0.0001$). P65 WT, $N = 5$, KI, $N = 5$.

(K and L) No differences in PV expression between groups. (P21: WT vs. KI: Mann-Whitney test, $p = 0.7857$; P65: WT vs. KI: Mann-Whitney test, $p = 0.0952$). For all plots, *N* represents mice. PV-mC4-WT (WT): blue squares, PV-mC4-KI (KI): red circles. All statistics,*$p < 0.05$, **$p < 0.01$, ***$p < 0.001$, ****$p < 0.0001$, two-way ANOVA, unless otherwise stated. Mean ± SEM shown.

PV-specific mC4-OE causes an increase in anxiety-like behavior in male mice

Anxiety and mood disorders are highly prevalent in SCZ patients, manifesting during the early stages of the illness and prior to episodes of psychosis.[59–62] To determine if PV-mC4-OE drives changes in anxiety-like behavior in P40-60 young adult mice, we used a behavioral battery, yielding a robust and reliable measure of behavior[63] (Figure 2A). To assess arousal levels, we measured the time spent by mice in a field's anxiogenic regions, namely the open or lighted areas (Figure 2B).

In the elevated zero maze (EZM), we observed no differences in the amount of time spent in the open arms between groups, suggesting that mice with increased mC4 expression in PV neurons did not display an overall change in anxiety-like behavior, relative to WT controls (Figure 2C). However, when we separated these data by sex, we observed a 46% reduction in the amount of time that KI males spent in the open arms, suggestive of a sexually dimorphic anxiety-like deficit (Figure 2D). In contrast, we did not see such change in the behavior of KI female mice, relative to their WT controls (Figure 2D). In the light-dark box (LDB), we observed a significant reduction in the time the PV-mC4-KIs spent in the light zone, again indicative of an increased anxiety-like response (Figure 2E). Separation of the data by sex did not reveal the same sexual dimorphism as observed in the EZM (Figure 2F). Lastly, in the novelty-suppressed feeding assay (NSF), we observed no change in the latency to feed between groups (Figure 2G). Despite this, much like the EZM, there was a significant increase in anxiety-like behavior in the KI male mice, observed via a 91% increase in the latency to feed, but no such changes were observed in the PV-mC4-KI females (Figure 2H). We performed the NSF in a safer environment, a mouse cage, where mice are exposed to bedding and can navigate close to the cage wall. In the cage NSF, we did not observe differences in the latency to feed between the groups (Figure S1), suggesting that the NSF in the novel environment is anxiety-inducing and that the male KI mice, indeed, have increased anxiety-like behavior levels.

To describe the anxiety-like behavior of mice in response to PV-mC4-OE, we used a z-scoring approach that effectively tracks the performance of each mouse across all three behavioral assays, yielding a single score for each mouse, termed its Z-Anxiety score.[63] We observed that the Z-Anxiety score of KI mice was increased in comparison to the control group (Figure 2I). However, we discovered that overall heightened anxiety-like behavior is solely driven by a significant increase in the Z-Anxiety of PV-mC4-KI male mice (Figure 2J). In support of this, female KI mice did not exhibit an increased Z-Anxiety score compared to the WT controls (Figure 2J). In summary, PV-mC4-OE causes sex-dependent behavioral changes, with male KI mice exhibiting increased anxiety-like behavior relative to WT controls.

Increased levels of mC4 in PV cells disrupt active but not passive social behaviors

We employed a naturalistic, freely moving interaction assay between experimental mice and a novel, juvenile, sex-matched CD-1 stimulus mouse to determine whether increased levels of mC4 in fast-spiking cells led to social behavioral changes (Figure 3). First, both male and female KI mice spent a similar time interacting with a novel object as their WT counterparts (Figures 3A and 3B), suggesting that PV-mC4-OE does not alter novelty-seeking behaviors or general motivation.

Immediately following the object interaction assay, the object was replaced with a stimulus mouse (Figure 3C). Interactions between WT or KI mice and the stimulus mouse were divided into one of five sub-classes (Figure 3C). Of all interaction sub-classes, experimental mice engaged in the active (active: experimental mouse initiating the interaction vs. passive: stimulus mouse initiating the interaction) snout-rear interaction (snout-ano-genital interactions) the most frequently, comprising half of all interaction time across all groups (Figure 3C,

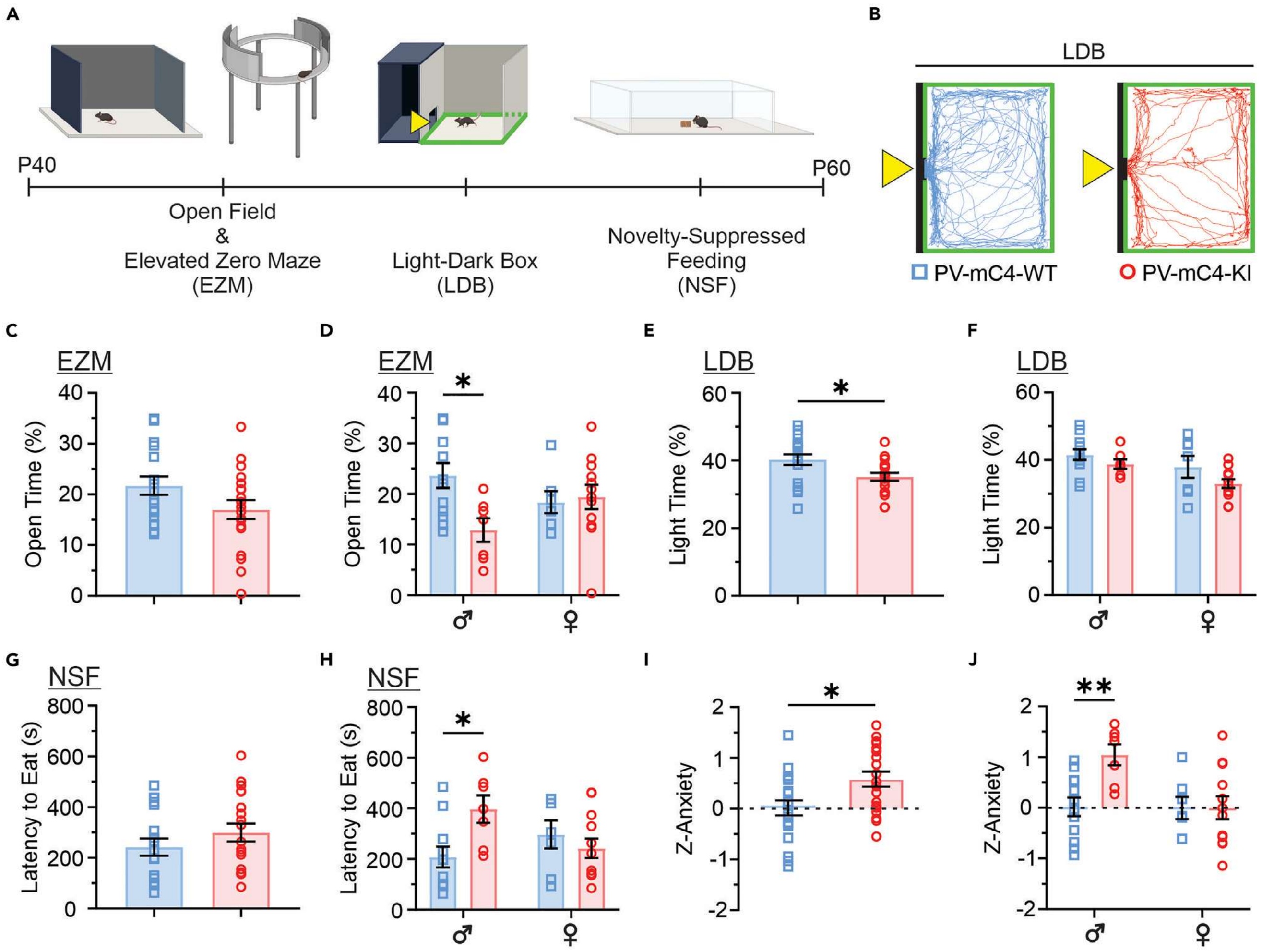

Figure 2. PV-specific mC4-OE causes an increase in anxiety-like behavior in male mice

(A) Timeline of behavioral assays. Mice were tracked in the light zone, represented by a green outline (B).

(B) Representative trajectories of WT (*blue*) and KI (*red*) mice in the light zone of the LDB (colored traces). Yellow triangle, entrance to the light zone.

(C) Percent time spent in the open arms of the EZM did not differ between WT and KI mice (Mann-Whitney test, *p* = 0.1912).

(D) Decreased time in the EZM open arms in male but not female KIs relative to WTs. (Condition x sex: $F[_{1,34}]$ = 5.324, **p* = 0.0273. Condition: $F[_{1,34}]$ = 3.579, *p* = 0.0671. Sex: $F[_{1,34}]$ = 0.06062, *p* = 0.8070. Post-test: WT vs. KI males, **p* = 0.0109, females, *p* = 0.9474).

(E) KI mice spent less time in the light zone of the LDB compared to WT mice (*t* test with Welch's correction, **p* = 0.0130).

(F) No sex-dependent differences in LDB light zone time between groups (condition x sex: $F[_{1,34}]$ = 0.3253, *p* = 0.5722. Condition: $F[_{1,34}]$ = 4.137, **p* = 0.0498. Sex: $F[_{1,34}]$ = 6.147, **p* = 0.0183. Post-test: WT vs. KI males, *p* = 0.5211, females, *p* = 0.1430).

(G) Latency to feed in the NSF did not differ between groups (unpaired *t*-test, *p* = 0.1964).

(H) Increase in the latency to feed for KI males compared to WT controls (condition x sex: $F[_{1,33}]$ = 6.718, **p* = 0.0141. Condition: $F[_{1,33}]$ = 2.061, *p* = 0.1606. Sex: $F[_{1,33}]$ = 0.4862, *p* = 0.4905. Post-test: WT vs. KI males, **p* = 0.0159, females, *p* = 0.6584).

(I) Increase in the Z-Anxiety of KI mice relative to WTs (unpaired *t*-test, **p* = 0.0114).

(J) Compared to WT controls, there was an increase in the Z-Anxiety of KI male but not KI female mice. (Condition x sex: $F[_{1,34}]$ = 5.209, **p* = 0.0289. Condition: $F[_{1,34}]$ = 5.325, **p* = 0.0272. Sex: $F[_{1,34}]$ = 5.756, **p* = 0.0221. Post-test: WT vs. KI males, ***p* = 0.0053, females, *p* = 0.9998). For all plots, *N* represents mice. PV-mC4-WT (WT): blue squares, *N* = 12 males, *N* = 7 females. PV-mC4-KI (KI): red circles, *N* = 7 males, *N* = 12 females. For all statistics,**p* < 0.05, ***p* < 0.01, two-way ANOVA, unless otherwise stated. Mean ± SEM shown.

percentages). Notably, PV-mC4-KI mice engaged less in active interactions than controls (Figure S2A); this reduction was driven by a 24% decrease in active snout-rear interaction (Figure 3D). These results indicate that increased levels of mC4 in PV cells lead to a reduction in snout-ano-genital interactions. Unlike the dimorphic nature of the anxiety-like behavior, deficits in sociability affected KI mice of both sexes (Figure 3D).

We observed more active than passive interactions by the experimental mice, which suggest that the experimental mice initiated more social interactions than the stimulus mice (Figures 3C and S2A). Furthermore, we did not notice any changes in passive interactions,

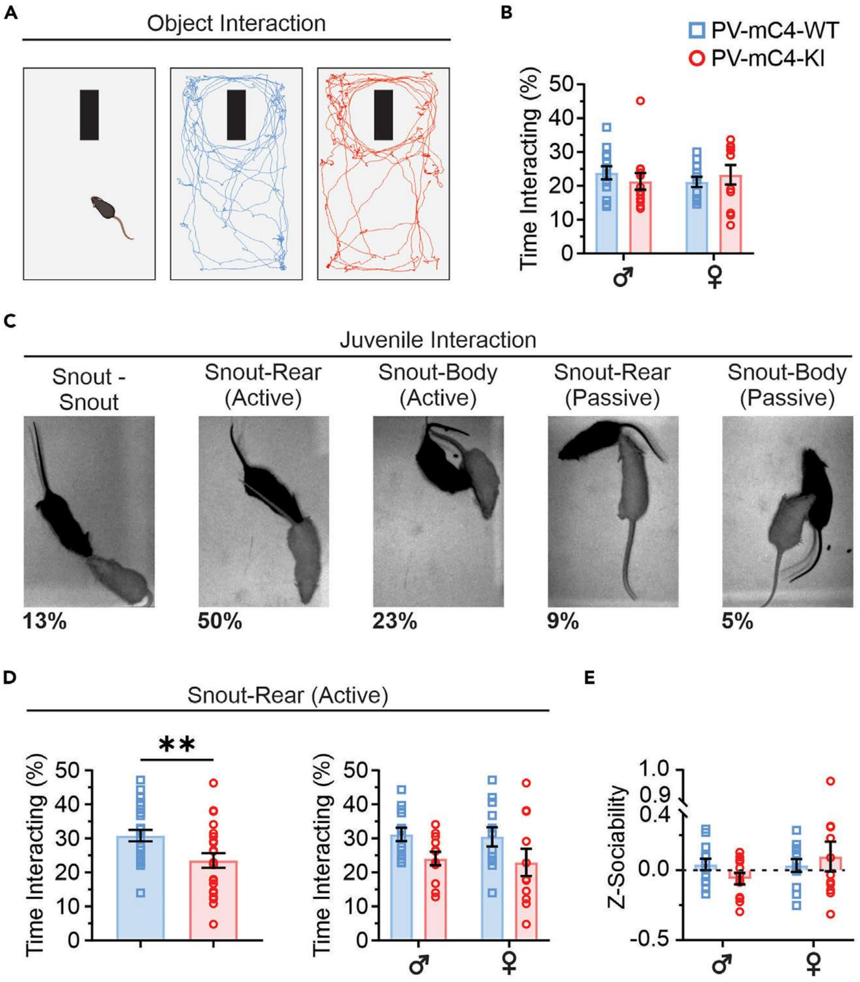

Figure 3. Increased levels of mC4 in PV cells disrupts active but not passive social behaviors

(A) Object interaction task (*left*). Representative trajectories of WT (*middle*, *blue*) and KI (*right*, *red*) exploring a novel object (*black rectangle*).

(B) KI mice explored the novel object as much as WT controls (condition x sex: F[$_{1,44}$] = 1.068, *p* = 0.3072. Condition: F[$_{1,44}$] = 0.008471, *p* = 0.9271. Sex: F[$_{1,44}$] = 0.02598, *p* = 0.8727).

(C) Representative images of interaction sub-classes. *Active*, experimental mouse engaging the stimulus mouse; *passive*, stimulus mouse engaging the experimental mouse. Percentage of each sub-class of behavior is in the following text.

(D) *Left*: relative to WT controls, KI mice spent less time engaged in the active snout-rear interaction type (*t* test with Welch's correction, ***p* = 0.0099). *Right*: there were no sex-related differences in active-snout-rear interaction between groups (condition x sex: F[$_{1,44}$] = 0.007274, *p* = 0.9324. Condition: F[$_{1,44}$] = 7.127, **p* = 0.0106. Sex: F[$_{1,44}$] = 0.1121, *p* = 0.7394. Post-test: WT vs. KI males, *p* = 0.1325, females, *p* = 0.1218).

(E) There was no change in Z-sociability in either KI male or female mice (condition x sex: F[$_{1,44}$] = 1.808, *p* = 0.1857. Condition: F[$_{1,44}$] = 0.09738, *p* = 0.7565. Sex: F[$_{1,44}$] = 1.507, *p* = 0.2261). For all plots, *N* represents mice. PV-mC4-WT (WT): blue squares, *N* = 13 males, *N* = 12 females. PV-mC4-KI (KI): red circles, *N* = 12 males, *N* = 11 females. All statistics,**p* < 0.05, ***p* < 0.01. Mean ± SEM shown.

indicating that stimulus mice behaved similarly when interacting with both groups (Figure S2). In the remaining interaction sub-classes, which were less frequent than the active snout-rear interaction, WT and KI mice interacted similarly with the stimulus mouse (Figures S2B–S2I).

Computing a Z-Sociability score that accounts for all five interaction sub-classes did not reveal a broad deficit in sociability (Figure 3E). Separately, in a three-chamber assay of sociability, a more restricted paradigm, PV-mC4-OE did not alter the social preference of PV-mC4-KIs, relative to WTs (Figure S3), suggesting all experimental animals preferred to interact with a mouse rather than an object. Our results also suggest that the freely moving interaction assay allowed us to capture the complex behavioral phenotype that OE mice exhibit.

Although female PV-mC4-KI mice did not exhibit changes in anxiety-like behavior, they had decreased social interactions as part of the KI group (Figure 3D), indicating that the mechanisms driving the pathology in the anxiety-like and social behaviors in response to PV-mC4-OE likely function independently. Overall, these results suggest that increased levels of mC4 in PV cells disrupt the circuits that underlie emotional and social behavior in mice.

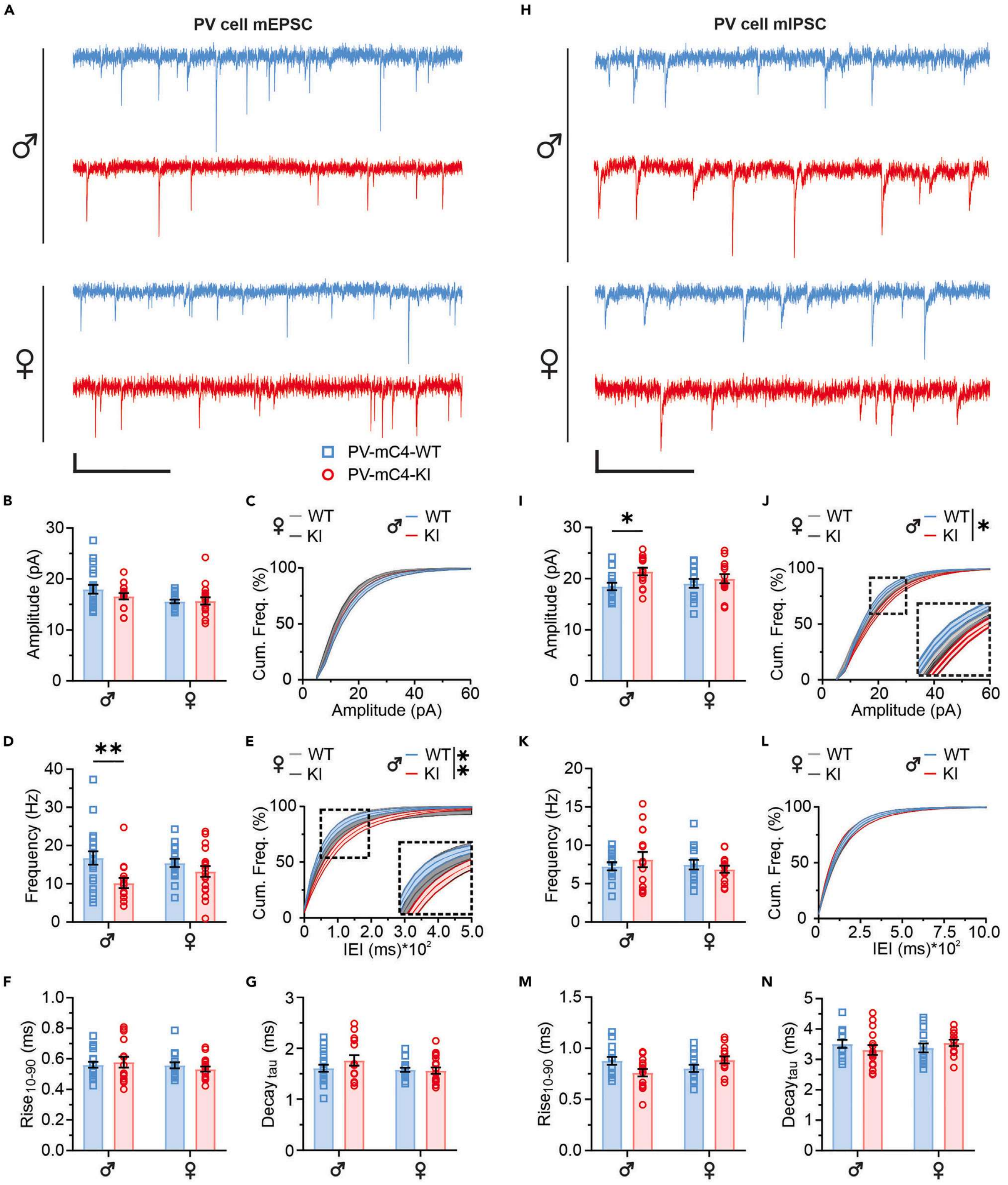

Figure 4. Sex-related difference in excitatory-inhibitory dynamics in mPFC PV cells with increased levels of mC4 in PV cells

(A) Representative 1 s voltage-clamp traces of mEPSCs recorded in PV cells of P40-60 WT (*blue*) and KI (*red*) mice, *scale bar*, 250 ms, 10 pA.

(B) No change in mEPSC amplitude in KI mice, compared to controls (condition x sex: $F[_{1,66}] = 1.111$, $p = 0.2956$. Condition: $F[_{1,66}] = 0.7845$, $p = 0.3790$. Sex: $F[_{1,66}] = 5.552$). *$p = 0.0214$. Post-test: WT vs. KI males, $p = 0.3225$, females, $p = 0.9910$).

Figure 4. *Continued*

(C) No shift in the cumulative frequency distribution of mEPSC amplitudes in KI mice (Kolmogorov-Smirnov test, WT vs. KI males, $p = 0.5758$, females, $p = 0.7810$).

(D) mC4-OE led to a decrease in mEPSC frequency in KI male mice, but not KI female mice (condition x sex: $F[_{1,66}] = 2.138$, $p = 0.1485$. Condition: $F[_{1,66}] = 8.979$, $^{**}p = 0.0038$. Sex: $F[_{1,66}] = 0.3501$, $p = 0.5561$. Post-test: WT vs. KI males, $^{**}p = 0.0051$, females, $p = 0.4809$).

(E) Increased mC4 expression caused a rightward shift in the distribution of mEPSC inter-event-intervals (IEIs) of PV cells in KI male mice, but not KI female mice (Kolmogorov-Smirnov test, males $^{**}p = 0.0059$, females, $p = 0.3079$).

(F) mEPSC $\text{Rise}_{10\text{-}90}$ was not impacted in KI mice, relative to WT controls (condition x sex: $F[_{1,66}] = 0.8620$, $p = 0.3566$. Condition: $F[_{1,66}] = 0.02164$, $p = 0.8835$. Sex: $F[_{1,66}] = 1.121$, $p = 0.2935$).

(G) mEPSC $\text{Decay}_{\text{tau}}$ was not changed in KI mice (condition x sex: $F[_{1,66}] = 1.426$, $p = 0.2367$. Condition: $F[_{1,66}] = 0.9701$, $p = 0.3282$. Sex: $F[_{1,66}] = 2.700$, $p = 0.1051$).

(H) Representative 1 s voltage clamp traces of mIPSCs recorded in PV cells of P40-60 WT (*blue*) and KI (*red*) mice, *scale bar*, 250 ms, 10 pA.

(I) mIPSC amplitude was increased in KI male, but not KI female mice (condition x sex: $F[_{1,53}] = 1.557$, $p = 0.2176$. Condition: $F[_{1,53}] = 5.831$, $^{*}p = 0.0192$. Sex: $F[_{1,53}] = 0.2637$, $p = 0.6097$. Post-test: WT vs. KI males, $^{*}p = 0.0232$, females, $p = 0.6599$).

(J) Increased expression of mC4 caused a rightward shift in the distribution of mIPSC amplitudes in KI male mice (Kolmogorov-Smirnov test, WT vs. KI males, $^{*}p = 0.0404$, females, $p = 0.9048$).

(K) mIPSC frequency was not changed in KI mice (condition x sex: $F[_{1,53}] = 1.117$, $p = 0.2954$. Condition: $F[_{1,53}] = 0.04095$, $p = 0.8404$. Sex: $F[_{1,53}] = 0.5669$, $p = 0.4548$).

(L) No shift in the distribution of mIPSC IEIs of KI mice (Kolmogorov-Smirnov test, WT vs. KI, males $p = 0.4149$, females, $p = 0.9988$).

(M) Relative to controls, there were no changes in mIPSC $\text{Rise}_{10\text{-}90}$ with increased levels of mC4 in PV cells (condition x sex: $F[_{1,53}] = 7.666$, $^{**}p = 0.0077$. Condition: $F[_{1,53}] = 0.2031$, $p = 0.6541$. Sex: $F[_{1,53}] = 0.4950$, $p = 0.4848$. Post-test: WT vs. KI males, $p = 0.0507$, females $p = 0.2079$).

(N) mIPSC $\text{Decay}_{\text{tau}}$ was not changed in KI mice (condition x sex: $F[_{1,53}] = 1.708$, $p = 0.1969$. Condition: $F[_{1,53}] = 0.01747$, $p = 0.8953$. Sex: $F[_{1,53}] = 0.1166$, $p = 0.7341$). PV-mC4-WT (WT): blue squares. PV-mC4-KI (KI): red circles. For all plots, N represents cells. mEPSC WT: $N = 20$ males, $N = 17$ females; mEPSC KI: $N = 15$ males, $N = 18$ females. mIPSC WT: $N = 14$ males, $N = 14$ females; mIPSC KI: $N = 15$ males, $N = 14$ females. For all statistics, $^{*}p < 0.05$, $^{**}p < 0.01$, two-way ANOVA used, unless otherwise stated. Mean ± SEM shown.

Sex-related differences in excitatory-inhibitory dynamics in mPFC PV cells with increased levels of mC4 in PV cells

To determine whether PV-mC4-OE changed the connectivity of circuits in the mPFC, we performed whole-cell voltage-clamp recordings in acute brain slices. Specifically, we first recorded miniature excitatory post-synaptic currents (mEPSCs) in PV neurons in layer (L) 2/3 of the mPFC in P40-60 mice (Figures 4A–4G), the same temporal window within which we identified behavioral deficits in response to PV-mC4-OE. Though we observed no change in PV cell mEPSC amplitude in PV-mC4-KI mice (Figures 4A–4C), we observed a 39% reduction in mEPSC frequency specifically in KI male mice (Figure 4D). In contrast, there were no changes in PV cell mEPSC frequency in the KI females (Figure 4D). In support of this, there was a rightward shift in the frequency distribution of inter-event-intervals (IEIs) in PV neurons in PV-mC4-KI males, but not females (Figure 4E), suggesting that PV-mC4-OE leads to a decrease in excitatory drive to this fast-spiking neuron. Finally, PV-mC4-OE did not alter the $\text{Rise}_{10\text{-}90}$ or $\text{Decay}_{\text{tau}}$ of mEPSCs recorded in PV cells (Figures 4F and 4G), suggesting that increased levels of mC4 did not alter the kinetics of the PV cell postsynaptic response.

Previous studies have shown that a decrease in synapses underlies the C4 hypoconnectivity phenotype in pyramidal cells.[34,41] We tested this by staining for bassoon and postsynaptic density 95 (PSD95), markers of presynaptic and excitatory postsynaptic structures, respectively, and analyzed colocalization patterns in the soma of PV cells (Figure S4). Using this approach, we observed clear instances of colocalization of pre-with postsynaptic markers, suggesting putative excitatory synapses in the soma of PV cells (Figure S4A). However, we did not see differences in the density of putative excitatory synapses—colocalized bassoon and PSD95 clusters—with overexpression of mC4 in PV cells compared to controls (Figure S4B). Additionally, increased levels of mC4 in PV cells did not cause sex-specific differences in the density of putative excitatory synapses (Figure S4C). This suggests that increased levels of mC4 in PV cells did not cause alterations in synaptic density. Instead, it points toward other mechanisms underlying the reduction in mEPSC frequency, such as changes in the probability of release. Alternatively, our immunohistochemical assay might not be sensitive enough to capture changes in the density of synapses in PV cells with mC4 overexpression.

To determine if PV-mC4-OE impacted the inhibitory drive to PV neurons, we recorded miniature inhibitory postsynaptic currents (mIPSCs) in this inhibitory cell type (Figures 4H–4N). Using a high-chloride internal recording solution with a chloride reversal potential of −13 mV yielded inward mIPSCs when recording at −70 mV (Figure 4H). The recordings revealed that PV-mC4-OE drove a 16% increase in the amplitude of PV cell mIPSCs (Figure 4I) and a rightward shift in the distribution of mIPSC amplitudes (Figure 4J), specifically in male, but not female mice, suggesting that inhibitory inputs are increased in PV cells in male PV-mC4-KI mice. Additionally, we observed no changes in mIPSC frequency (Figures 4K and 4L), $\text{Rise}_{10\text{-}90}$ (Figure 4M), or $\text{Decay}_{\text{tau}}$ (Figure 4N) between groups.

Taken together, these results suggest that PV-mC4-OE drives sex-dependent alterations in PV cell excitatory and inhibitory connections, mirroring the sexually dimorphic changes in anxiety-like behavior. The combined effects of reduced excitation and increased inhibition to PV cells in KI male mice suggest hypoactivity of mPFC inhibitory circuits in response to increased levels of mC4 in fast-spiking cells.

PV-specific mC4-OE leads to opposing changes in the excitability of PV cells in male and female mice

We evaluated the passive and active properties of both mPFC L2/3 PV cells (Figures 5A–5E; Tables S1 and S2) and PYRs (Figures 5F–5J; Tables S3 and S4). To accomplish this, we injected steps of hyperpolarizing and depolarizing current pulses and recorded the membrane voltage (V_m) changes. Changes in excitability of PV neurons in male and female mice in response to PV-mC4-OE diverged: while there was a significant decrease in PV cell spike frequency in KI male mice relative to WT males (Figures 5A and 5B), we observed a significant

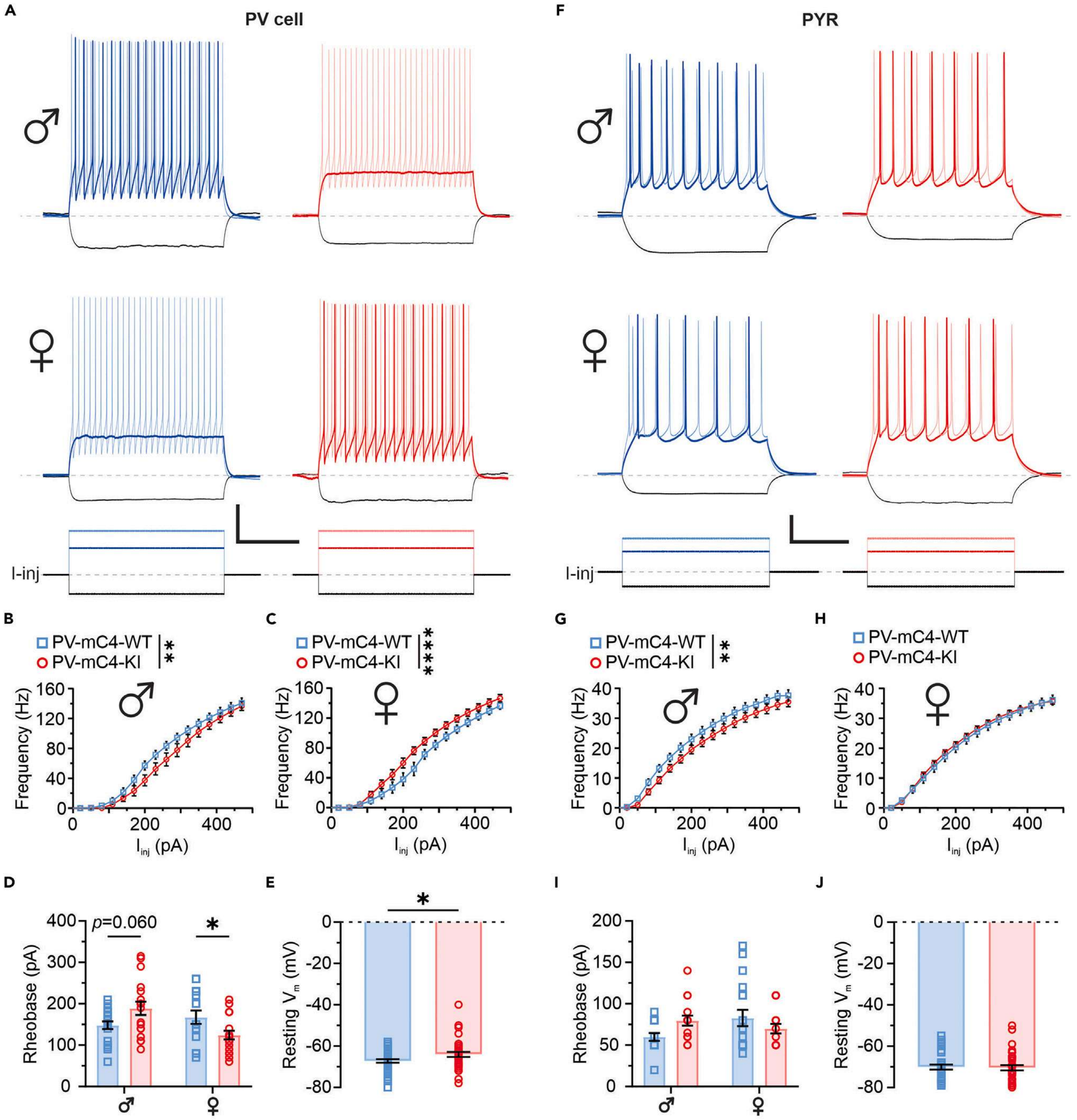

Figure 5. PV-specific mC4-OE leads to opposing changes in excitability of PV cells in male and female mice

(A) Representative recordings of PV cells injected with −100 (*black*), 140 (*darker colored shade*), and 230 pA (*lighter colored shade*) of current from WT (*blue*) and KI (*red*) mice, *scale bar*, 200 ms, 200 pA/20 mV. Baseline V_m, −65 mV.

(B) PV cells in KI male mice spike less than PV cells in WT male mice (repeated measure [RM] two-way ANOVA, condition x current: $F_{[24,840]} = 1.941$, $^{**}p = 0.0045$. Condition: $F_{[1,35]} = 1.989$, $p = 0.1672$. Current: $F_{[1.656,57.95]} = 416.4$, $^{****}p < 0.0001$).

(C) mC4-OE led to a significant increase in the excitability of PV cells in KI female mice, relative to controls (RM two-way ANOVA, condition x current: $F_{[24,816]} = 3.428$, $^{****}p < 0.0001$. Condition: $F_{[1,34]} = 4.178$, $^{*}p = 0.0488$. Current: $F_{[1.719,58.46]} = 568.3$, $^{****}p < 0.0001$).

(D) Rheobase of PV cells was decreased in KI female mice, relative to controls (condition x sex: $F_{[1,69]} = 10.23$, $^{**}p = 0.0021$. Condition: $F_{[1,69]} = 0.008666$, $p = 0.9261$. Sex: $F_{[1,69]} = 2.932$, $p = 0.0913$. Post-test: WT vs. KI males, $p = 0.0596$, females, $^{*}p = 0.0472$).

(E) PV-mC4-OE drove a shift in PV cell resting membrane voltage toward a more depolarized V_m (*t* test with Welch's correction, $^{*}p = 0.0356$).

Figure 5. ***Continued***

(F) Representative recordings of PYRs injected with −100 (*black*), 140 (*darker colored shade*), and 230 pA (*lighter colored shade*) from WT (*blue*) and KI (*red*) mice, *scale bar*, 200 ms, 200 pA/20 mV.

(G) OE of mC4 significantly decreased the spike frequency of PYRs in KI male mice, relative to controls (RM two-way ANOVA, condition x current: $F[_{24,696}] = 1.975$, $^{**}p = 0.0038$. Condition: $F[_{1,29}] = 2.646$, $p = 0.1147$. Current: $F[_{1.350,39.15}] = 619.8$, $^{****}p < 0.0001$).

(H) No differences in the excitability of PYRs in females between groups (RM two-way ANOVA, condition x current: $F[_{24,816}] = 0.2813$, $p = 0.9998$. Condition: $F[_{1,34}] = 0.1154$, $p = 0.7361$. Current: $F[_{1.467,49.89}] = 810.0$, $^{****}p < 0.0001$).

(I) No change in PYR rheobase (condition x sex: $F[_{1,63}] = 5.148$, $^{*}p = 0.0267$. Condition: $F[_{1,63}] = 0.2332$, $p = 0.6308$. Sex: $F[_{1,63}] = 0.8369$, $p = 0.3638$. Post-test: WT vs. KI males, $p = 0.1262$, females, $p = 0.3502$).

(J) No change in PYR resting V_m in KI mice, compared to controls (Mann-Whitney test, $p = 0.6464$). For all plots, *N* represents cells. PV-mC4-WT (WT): blue squares. PV-mC4-KI (KI): red circles. PV cell WT: $N = 19$ males, $N = 17$ females; PV cell KI: $N = 18$ males, $N = 19$ females. PYR WT: $N = 15$ males, $N = 18$ females; PYR KI: $N = 16$ males, $N = 18$ females. For all statistics,$^{*}p < 0.05$, $^{**}p < 0.01$, two-way ANOVA, unless otherwise stated. Mean ± SEM shown.

increase in the spike frequency of PV cells in female KI mice, compared to WT females (Figures 5A and 5C). This increase in excitability in PV cells in KI females was also accompanied by a 26% reduction in their rheobase, another indication of increased excitability (Figure 5D). Finally, we observed a significant shift toward a more depolarized resting membrane voltage in KI mice overall (Figure 5E; Tables S1 and S2). These results suggest that there is a sex-dependent divergence in the fast-spiking cell's excitability with higher mC4 levels in PV cells.

Though mC4-OE is limited to PV cells in this mouse model, it is possible that disruption in the activity of PV cells may elicit compensatory changes in PYRs. To this end, we recorded the membrane voltage response as before, now in mPFC L2/3 PYRs (Figures 5F–5J). Similar to PV neurons, in male mice, PV-mC4-OE drove a reduction in the spike frequency of PYRs (Figures 5F and 5G). Unlike PV cells, we observed no changes in spike frequency in the PYRs of KI female mice (Figures 5F and 5H). Moreover, PV-mC4-OE did not alter the rheobase (Figure 5I) or resting membrane voltage (Figure 5J) of PYRs. These results indicate that PV-mC4-OE induced changes in PYR excitability in male mice.

Overall, increased mC4 levels in PV cells caused sexually dimorphic effects on the excitability of cortical cells. Fast-spiking cells and PYRs in males showed a decrease in excitability, while fast-spiking cells in females exhibited hyperexcitability. This divergent outcome suggests that the male and female mouse brain respond to complement dysfunction in opposing ways.

PV-specific mC4-OE does not significantly change the synaptic drive of mPFC PYRs

We recorded mEPSCs (Figures S5A–S5E) and mIPSCs (Figures S5F–S5J) in L2/3 mPFC PYRs. PV-mC4-OE did not lead to changes in PYR mEPSC amplitude (Figure S5B) or frequency (Figure S5C) compared to controls. While the $\text{Rise}_{10\text{-}90}$ of the mEPSCs in PYRs was also not altered in PV-mC4-KI mice (Figure S5D), PV-mC4-OE caused a 14% reduction in $\text{Decay}_{\text{tau}}$ of the mEPSCs in KI female, but not KI male mice (Figure S5E), suggesting a change in receptor subunit composition in PYRs[64] or a change in the location of excitatory synapses along its somatodendritic axis.[65,66] Finally, PV-mC4-OE did not induce changes in PYR mIPSC amplitude (Figure S5G), frequency (Figure S5H), or kinetics (Figures S5I and S5J) relative to controls. The findings indicate that PV-mC4-OE does not significantly change the synaptic drive to mPFC PYRs.

No changes in anxiety-like behavior or excitatory drive to PV cells with pan-neuronal overexpression of mC4

Next, we crossed the mC4-KI mouse to the BAF53b-Cre transgenic mouse line[67] that expresses Cre recombinase under the control of the mouse *Actl6b* gene promoter to drive mC4-OE in all neurons (PanN-mC4-OE). The expression of the BAF53b gene in neurons can first be detected during embryonic day 12.5 in the brain and spinal cord.[68] Using a similar breeding strategy as with the PV-mC4-KI mice, litters consisted of a mix of mice that inherited the floxed mC4-KI allele and thus overexpressed mC4 in all neurons (PanN-mC4-KI), or littermates that did not inherit the floxed mC4-KI allele, and thus were effectively WT (PanN-mC4-WT) (Figure 6A, *top*). This manipulation drove overexpression of *mC4* in neurons (Rbfox3-positive DAPI-labeled cells), as well as weaker overexpression in other non-neuronal cells (Rbfox3-negative DAPI-labeled cells (Figure S6). This suggests we could drive overexpression in Rbfox3-positive neurons, although this manipulation was not entirely specific to this cell type. Alternatively, it is possible that the Rbfox3 mRNA probes are not completely cell-type specific.

We employed the same assays—the EZM, LDB, and NSF—to test anxiety-like behavior in P40-60 PanN-mC4-WT and PanN-mC4-KI mice (Figure 6A, *bottom*). First, OE of mC4 in all neurons did not alter the distance traveled compared to controls (Figures 6B and 6C), suggesting that PanN-mC4-KI mice exhibited intact locomotion. Moreover, compared to controls, we did not observe any deficit in anxiety-like behavior in PanN-mC4-KI mice in the EZM (Figures 6D and 6E), LDB (Figures 6F and 6G), or NSF (Figures 6H and 6I). Also, we did not observe any increase in Z-Anxiety in PanN-mC4-KI mice (Figure 6J), nor in either sex specifically (Figure 6K). Taken together, PanN-mC4-OE does not drive anxiety-like behavior in mice.

To determine if PanN-mC4-OE drove similar changes in the excitatory drive to PV cells as did PV-mC4-OE, we recorded mEPSCs in PV cells in PanN-mC4-WT and PanN-mC4-KI animals of both sexes (Figure S7). We observed no changes in the amplitude (Figures S7A and S7B), frequency (Figure S7C), or kinetics (Figures S7D and S7E) of mEPSCs recorded in the PV cells of PanN-mC4-KI mice, relative to PanN-mC4-WT mice. These experiments suggest that excitatory circuits to PV cells are especially susceptible to cell-type specific overexpression of mC4.

We have demonstrated that increased levels of mC4 in PV neurons resulted in a strong, sex-specific anxiety-like phenotype not observed in pan-neuronal mC4 overexpressors. In line with this result, the functional excitatory hypoconnectivity observed in PV cells of PV-mC4-KI males

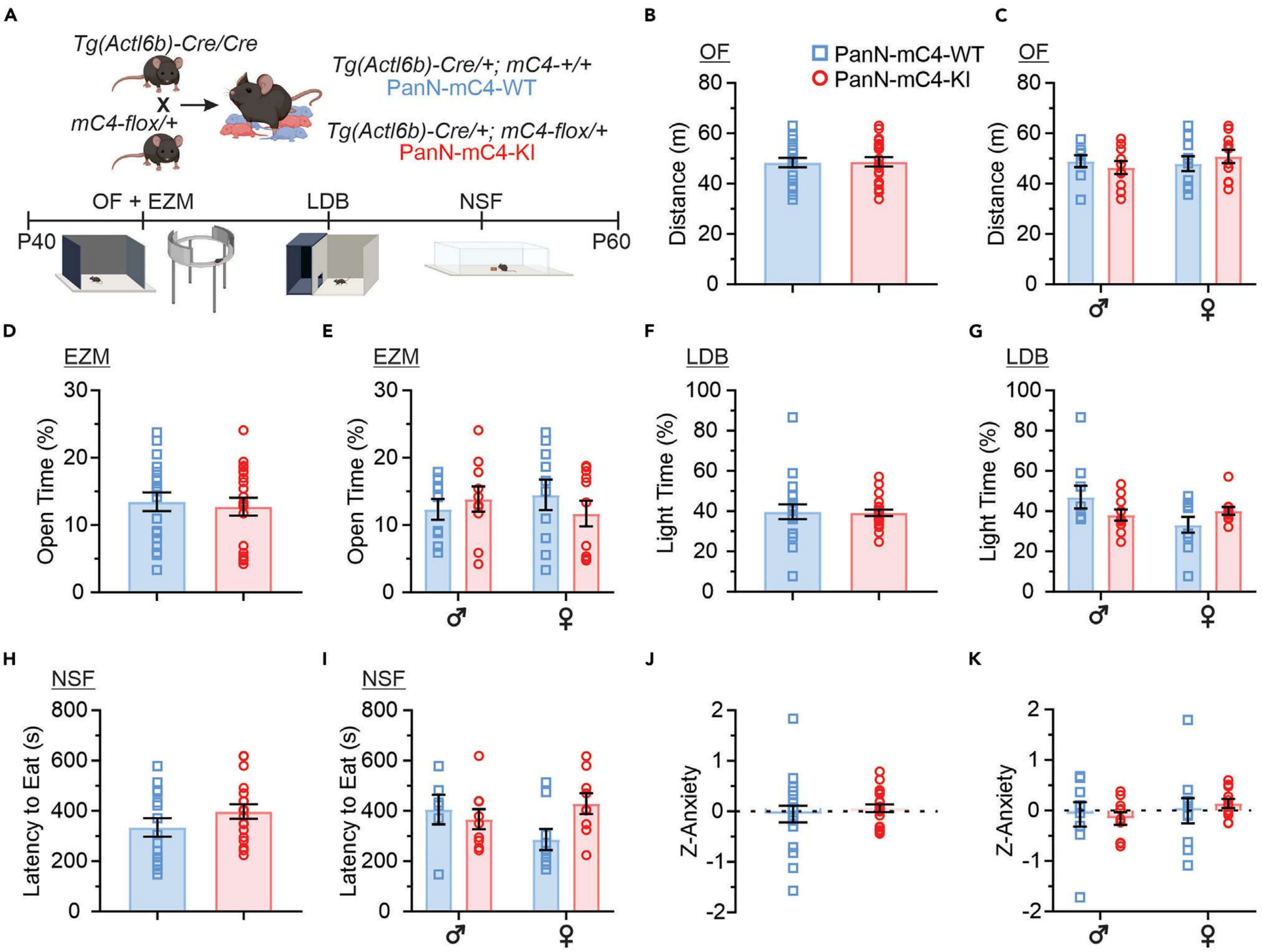

Figure 6. No changes in anxiety-like behavior with pan-neuronal overexpression of mC4

(A) Mouse breeding (*top*) and anxiety behavioral battery (*bottom*) as in Figure 2.

(B and C) Pan-neuronal mC4 overexpression does not alter locomotion (B: *t* test, *p* = 0.9092. C: condition x sex: F[$_{1,36}$] = 1.039, *p* = 0.3148. Condition: F[$_{1,36}$] = 0.00415, *p* = 0.9490. Sex: F[$_{1,36}$] = 0.4105, *p* = 0.5258).

(D and E) No change in time spent in the open arms of the EZM with pan-neuronal mC4 overexpression (D: Mann-Whitney test, *p* = 0.6487. E: condition x sex: F[$_{1,36}$] = 1.225, *p* = 0.2757. Condition: F[$_{1,36}$] = 0.1021, *p* = 0.7512. Sex: F[$_{1,36}$] = 0.00008, *p* = 0.9928).

(F and G) Time spent in the light zone of the LDB was not altered by pan-neuronal mC4 overexpression (F: Mann-Whitney test, *p* = 0.9360. G: Condition x Sex: F[$_{1,36}$] = 4.620, **p* = 0.0384. Condition: F[$_{1,36}$] = 0.07082, *p* = 0.7917. Sex: F[$_{1,36}$] = 2.552, *p* = 0.1189. Post-test: WT vs. KI males, *p* = 0.1977, females, *p* = 0.3281).

(H and I) Overexpression of mC4 in neurons did not alter the latency to feed in the NSF (H: *t* test, *p* = 0.1761. I: Condition x Sex: F[$_{1,29}$] = 4.093, *p* = 0.0524. Condition: F[$_{1,29}$] = 1.328, *p* = 0.2586. Sex: F[$_{1,29}$] = 0.4055, *p* = 0.5293).

(J and K) Increased levels of mC4 in neurons did not lead to drastic changes in overall anxiety-like behavior, as measured with Z-anxiety scores. (J: *t* test with Welch's correction, *p* = 0.5358. K: Condition x Sex: F[$_{1,36}$] = 0.3797, *p* = 0.5416. Condition: F[$_{1,36}$] = 0.03077, *p* = 0.8617. Sex: F[$_{1,36}$] = 1.008, *p* = 0.3221). For all plots, *N* represents mice. PanN-mC4-WT: blue squares, *N* = 9 males, *N* = 10 females. PanN-mC4-KI: red circles, *N* = 10 males, *N* = 11 females. For all statistics, **p* < 0.05, two-way ANOVA, unless otherwise stated. Mean ± SEM shown.

was not observed in response to PanN-mC4-OE. Together, these results suggest that specific complement changes in PV cells lead to developmental dysfunction of inhibitory circuits that are especially detrimental.

Disrupted neural communication and hyperexcitability in a network model of male mice with increased levels of mC4 in PV cells

We used a computational model to determine how PV-mC4-driven deficits in connectivity and excitability of PYRs and PV cells contribute to circuit-level abnormalities in a simulated network. Utilizing the DynaSim toolbox,[69] we developed four networks with identical architecture (Figure 7A) representing the experimental conditions—WT and KI male, and WT and KI female groups. The electrophysiological properties of individual PYRs and PV cells—and their connectivity to one another—were matched to the experimental data (Tables S5 and S6).

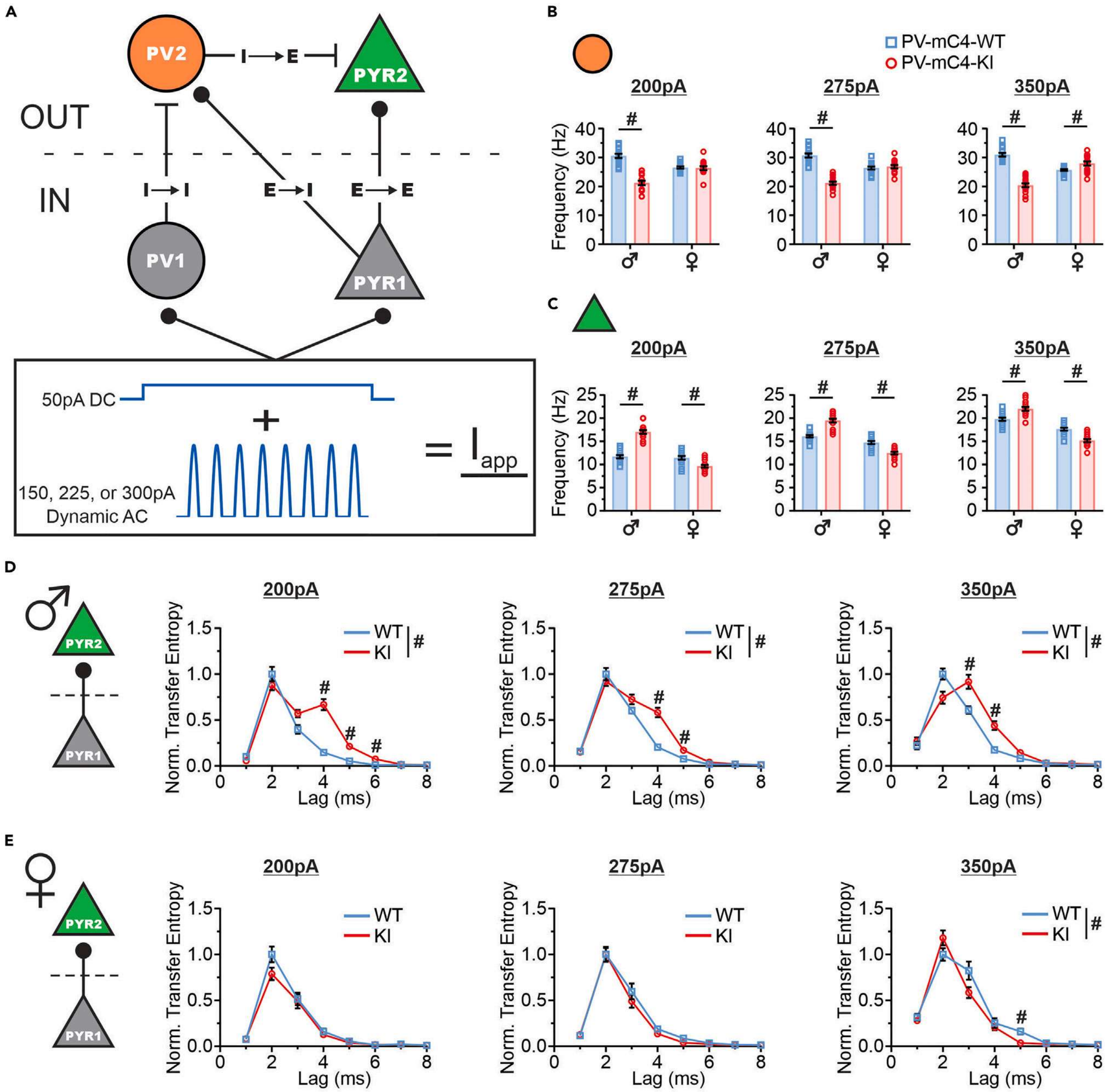

Figure 7. Disrupted neural communication and hyperexcitability in a network model of male mice with increased levels of mC4 in PV cells

(A) Network architecture and applied current (I_{app}).

(B) The firing rate of PV2 in WT and KI networks at peak I_{app} of 200 pA (*left*, condition x sex: $F_{[1,56]} = 49.79$, ****$p < 0.0001$. Condition: $F_{[1,56]} = 54.23$, ****$p < 0.0001$. Sex: $F_{[1,56]} = 0.7170$, $p = 0.4007$. Post-test: WT vs. KI males, ****$p < 0.0001$, females, $p = 0.9706$), 275 pA (*middle*, condition x sex: $F_{[1,56]} = 71.87$, ****$p < 0.0001$. Condition: $F_{[1,56]} = 58.30$, ****$p < 0.0001$. Sex: $F_{[1,56]} = 1.390$, $p = 0.2434$. Post-test: WT vs. KI males, ****$p < 0.0001$, females, $p = 0.8010$), and 350 pA (*right*, condition x sex: $F_{[1,56]} = 114.7$, ****$p < 0.0001$. Condition: $F_{[1,56]} = 47.97$, ****$p < 0.0001$. Sex: $F_{[1,56]} = 3.473$, $p = 0.0676$. Post-test: WT vs. KI males, ****$p < 0.0001$, females, *$p = 0.0195$).

(C) The firing rate of PYR2 in WT and KI networks at peak I_{app} of 200 pA (*left*, condition x sex: $F_{[1,56]} = 98.21$, ****$p < 0.0001$. Condition: $F_{[1,56]} = 24.10$, ****$p < 0.0001$. Sex: $F_{[1,56]} = 113.4$, ****$p < 0.0001$. Post-test: WT vs. KI males, ****$p < 0.0001$, females, **$p = 0.0016$), 275 pA (*middle*, condition x sex: $F_{[1,56]} = 74.29$, ****$p < 0.0001$. Condition: $F_{[1,56]} = 2.972$, $p = 0.0902$. Sex: $F_{[1,56]} = 163.2$, ****$p < 0.0001$. Post-test: WT vs. KI males, ****$p < 0.0001$, females, ****$p < 0.0001$), and 350 pA (*right*, condition x sex: $F_{[1,56]} = 44.10$, ****$p < 0.0001$. Condition: $F_{[1,56]} = 0.1087$, $p = 0.7429$. Sex: $F_{[1,56]} = 162.9$, ****$p < 0.0001$. Post-test: WT vs. KI males, ****$p < 0.0001$, females, ****$p < 0.0001$).

(D) Plots showing the average transfer entropy (TE) at each delay (lag) of PYR1 onto PYR2 in male WT (*blue*) and male KI (*red*) networks at peak I_{app} of 200 pA (*left*, condition x lag: $F_{[7,196]} = 15.72$, ****$p < 0.0001$. Condition: $F_{[1,28]} = 45.51$, ****$p < 0.0001$. Lag: $F_{[2.031,56.86]} = 172.5$, ****$p < 0.0001$), 275 pA (*middle*, condition x lag:

Figure 7. *Continued*

$F_{[7,196]}$ = 8.938, *****p* < 0.0001. Condition: $F[_{1,28}]$ = 38.25, *****p* < 0.0001. Lag: $F[_{2.768,\ 77.52}]$ = 223.9, *****p* < 0.0001), and 350 pA (*right*, condition x lag: $F_{[7,196]}$ = 9.861, *****p* < 0.0001. Condition: $F_{[1,28]}$ = 32.48, *****p* < 0.0001. Lag: $F_{[2.687,75.22]}$ = 149.7, *****p* < 0.0001).

(E) Plots showing the average transfer entropy (TE) at each delay (lag) of PYR1 onto PYR2 in female WT (*blue*) and female KI (*red*) networks at peak I_{app} of 200 pA (*left*, condition x lag: $F_{[7,196]}$ = 1.576, *p* = 0.1446. Condition: $F_{[1,28]}$ = 6.672, **p* = 0.0153. Lag: $F_{[1.772,49.61]}$ = 121.6, *****p* < 0.0001), 275 pA (*middle*, condition x lag: $F_{[7,196]}$ = 0.4033, *p* = 0.8995. Condition: $F_{[1,28]}$ = 14.14, ****p* = 0.0008. Lag: $F_{[1.484,41.55]}$ = 127.9, *****p* < 0.0001), and 350 pA (*right*, condition x lag: $F_{[7,196]}$ = 3.124, ***p* = 0.0038. Condition: $F_{[1,28]}$ = 13.92, ****p* = 0.0009. Lag: $F_{[1.985,55.57]}$ = 135.6, *****p* < 0.0001). PV-mC4-WT (WT) network: blue squares. PV-mC4-KI (KI) network: red circles. *N* represents simulations. *N* = 15 for all networks. For all statistics, **p* < 0.05, ***p* < 0.01, ****p* < 0.001, *****p* < 0.0001, two-way ANOVA (B and C) or repeated-measure two-way ANOVA with multiple comparisons (D and E). Mean ± SEM shown. For all plots, "#" indicates all *p* < 0.05.

Specifically, we first established unique models of PV and PYR cells for each group using our experimental data (Table S5). To determine if these model cells accurately reflected the experimental data, we compared the frequency vs. current (FI) curves of each model cell against its equivalent experimental cell (Figure S8). In all cases, the model cells accurately approximated their experimental counterpart.

We hypothesized that downstream PYR in KI males would become hyperactive as a function of reduced inhibition. In support of this, in the output layer of the male KI neural network model we observed a significant decrease in the firing rate (FR) of PV2 (Figure 7B) and a significant increase in PYR2 FR (Figure 7C) at all three peak values of the applied current (I_{app}), compared to the male WT network. This suggests that in the network model, increased levels of mC4 in male PV model cells cause decreased activity of this fast-spiking model neuron, driving hyperactivity of PYR model cells.

To determine if the changes associated with PV-mC4-OE disrupt neuronal communication, we measured the transfer entropy (TE) of the direct PYR1 → PV2 (Figures S9A–S9C) and PYR1 → PYR2 (Figures 7D and 7E) connections. Specifically, we first investigated the likelihood that a spike in PYR1 would cause a spike in PV2 (Figures S9B and S9C). In line with our hypothesis, we observed a significant reduction in the PYR1 → PV2 TE in the male KI network at lag times of 1–3 ms at all peak values of I_{app} (Figure S9B). This suggests that the effective transfer of information from PYR1 to PV2 is disrupted in the male KI network. This finding was further supported by a significant increase in both the average (Figure S9D) and standard deviation (Figure S9E) of the latency from any given PYR1 spike to the nearest following spike observed in PV2. Consistent with this compromised PYR1 → PV2 communication, because PV2 is the only line of inhibition to PYR2 in the network, the PYR1 → PYR2 TE is also significantly altered in the male KI network (Figure 7D). Namely, we observed a broadening of the lag times over which activity in PYR1 could drive changes in PYR2 activity (Figure 7D), indicating that the precise temporal relationship of PYR1 → PYR2 communication is disrupted in the model male KI network compared to controls.

In KI female mice, we observed a significant increase in the intrinsic excitability of PV cells in response to PV-mC4-OE (Figure 5). Interestingly, we observed no changes in the PV2 FR in the female KI network in either the 200 or 275 pA peak I_{app}, compared to the female controls (Figure 7B, *left*, *middle*). However, when the peak of I_{app} was raised to 350 pA, we observed a significant 9% increase in the FR of PV2 in the female KI network (Figure 7B, *right*), suggesting that at lower peak applied current values, the increase in intrinsic excitability of PV cells in the female KI network—and the potential increase in PV2 FR that may be expected in response to input from PYR1—is neutralized by the increased spiking activity of PV1 (and thus PV1 inhibition to PV2). However, our results suggest that when we applied stronger stimulation, the intrinsic excitability of PV2 and its resulting increase in FR outweighs the influence of increased inhibition.

Notably, in the female KI network, despite observing no change in PV2 FR at peak I_{app} values of 200 and 275 pA, the FR of PYR2 is still significantly decreased compared to controls. Provided that PV2 is the only source of inhibition to PYR2, this finding of a lack of change in PV2 FR but a decrease in FR of PYR2 appears incongruous. To determine if it is not changes in the number of spikes, but in the timing of spikes of PV2 relative to PYR2 that may be driving this decrease in PYR2 FR in the female KI network, we compared the PYR1 → PV2 TE in the female WT and KI networks (Figure S9C). At shorter lag times, we observed a significant increase of approximately 100% in the PYR1 → PV2 TE of the female KI network relative to its control for all peak I_{app} values (Figure S9C).

This increase in TE resulted in a significant reduction in both the mean (Figure S9D) and standard deviation (Figure S9E) of the PYR1xPV2 latency in the female KI network compared to controls, suggesting that the sculpting of the PV2 firing pattern is more precise and consistent in the female KI network than in the female WT network. The net effect of this result is a firing pattern of PV2 that is more effective in suppressing the excitation reaching PYR2 (Figure S9F).

In the female KI network, low-intensity I_{app} did not alter PYR1 → PYR2 TE relative to controls, suggesting intact PYR model cell communication (Figure 7E). However, at a higher I_{app}, we observed significant changes in the PYR1 → PYR2 TE (Figure 7E, *right*), suggesting that neural communication in the female KI network is slightly altered with stronger stimulation compared to controls. These results also suggest that female PYR model cells are more resilient to inhibitory circuit perturbations than male networks.

In total, our results demonstrate that changes in intrinsic properties and synaptic connectivity associated with PV-mC4-OE decrease synaptic fidelity between model PYR and PV cells and cause hyperexcitability in a network model of male mice with increased levels of mC4 in PV cells.

DISCUSSION

Using a new model to overexpress mC4 conditionally, we have discovered that mPFC PV cells in male mice are susceptible to complement dysfunction. Additionally, we have established a connection between the mC4-driven alterations in the circuitry of the mPFC and pathological anxiety-like behavior in male mice. Increased levels of mC4 in PV neurons also disrupted both excitatory and inhibitory inputs to fast-spiking cells in male but not female mice. Furthermore, we have demonstrated that specific OE of mC4 in PV cells led to opposing effects on the excitability of cortical cells. While mC4-OE in PV cells drove a decrease in the excitability of both male fast-spiking cells and PYRs, it led to hyperexcitability of female PV cells. By utilizing a Cre-driver line to induce mC4-OE in all neurons, we also observed that specific mC4 dysfunction in PV cells has a greater adverse effect on anxiety-like behavior than widespread neuronal complement alterations. Using a computational model that describes a simple neuronal network, we demonstrated that PV-mC4-driven inhibitory microcircuit deficits in the male model network led to disrupted neural communication between PYR model cells and hyperexcitability. Overall, these results establish a causative link between the SCZ-associated gene, *C4*, and the vulnerability of fast-spiking cells, which are crucial for the function of the mPFC.

Synaptic alterations in fast-spiking cells with PV-specific mC4 overexpression

Here, we demonstrate that in male mice, conditionally targeting mC4-OE to PV cells leads to a drastic loss of excitatory drive on this inhibitory cell type that is accompanied by increased inhibition. Several lines of evidence point to synaptic dysfunction and pathological excitatory synaptic loss as prominent features of SCZ.[22,70–72] In support of this, our group and others previously demonstrated that increased levels of C4 in developing L2/3 mPFC PYRs are sufficient to cause a significant loss of excitatory synapses, leading to mPFC circuit dysfunction.[34,41] Our results reveal a significant decrease in the frequency of mEPSCs on PV cells without alterations in their amplitude.

Building on prior research[34,41,42] that links elevated C4 levels to reduced connectivity via fewer synapses, we investigated whether the observed decrease in mEPSC frequency within male PV cells stemmed from a decline in the density of excitatory synapses targeting these inhibitory neurons. However, we did not observe alterations in the density of putative synapses with increased levels of mC4 in PV cells. This unexpected result suggests that decreased synaptic input could be driven by other mechanisms, such as alterations in the release probability of excitatory terminals, which cannot be captured using staining methods. It is also possible that excitatory synaptic density in PV cells was indeed altered with mC4 overexpression, but the staining assay was not sensitive enough to capture differences between control and PV-mC4-KI conditions.

While it is yet to be established whether pathological dysfunction in SCZ is confined to specific microcircuitry, a study conducted in SCZ postmortem tissue demonstrated that there is a decrease of excitatory synapses on PFC PV cells relative to control subjects.[22] In support of this, dysregulated ErbB4, a receptor of the SCZ-linked protein neuregulin-1, may contribute to lower activity of PV cells by reducing their excitatory inputs.[73] A decrease in the excitatory drive to fast-spiking interneurons has also been observed in mouse models of AD[74,75] and neurodevelopmental disorders,[76–78] suggesting that dysfunction in feedforward excitatory synapses to fast-spiking cells is a common denominator in brain pathology.

A long-standing hypothesis is that defects in the GABAergic inhibitory system can contribute to SCZ.[79] Additionally, cognitive impairment in SCZ could be the result of dysfunction in the convergence of glutamatergic and GABAergic systems.[80] One possible outcome of decreased excitation on PV cells in the male PV-mC4-KI mouse is a disruption in the dynamics of excitation and inhibition, tipping the scales toward the side of unchecked excitation and excess glutamatergic release. This also aligns well with the NMDA-hypofunction SCZ model,[81–83] where the loss of NMDA receptors, specifically on interneurons, results in the hypoactivity of PV neurons. Alterations in inhibitory circuitry could also alter the timing of excitation and inhibition[84] that controls oscillatory activity and information flow.[10]

We observed a significant increase in the amplitude of mIPSCs in PV cells in PV-mC4-KI male, but not female mice, suggesting an enhancement of inhibitory inputs to fast-spiking cells. Naturally, this effect would amplify the putative decrease in PV cell activity in the male PV-mC4-KI mice, already caused by the reduction in the excitatory drive to this interneuron. As increased inhibition of PV cells is counterintuitive to the effects that increased complement activity would have on inhibitory synapses or a compensatory change to enhance the drive of fast-spiking cells, we can only conclude that these are mC4-driven maladaptive changes in the male brain. Whether this increase in mIPSC amplitude is driven by presynaptic changes in quantal size or postsynaptic changes in GABA receptor subunit composition or sensitivity is unknown and will require deeper investigation.

Microglia-dependent synaptic engulfment is an established mechanism for complement-driven synaptic loss in the normal and diseased brain.[51,85–87] Studies using mice that lack specific complement genes have shown that these immune molecules contribute to synaptic plasticity.[88–90] In fact, complement upregulation has been observed in several neurodegenerative diseases where synaptic loss is a prominent feature.[91–93] A recent study also showed that C1q, the initiating member of the classic complement pathway, binds neuronal activity-regulated pentraxin (Nptx2),[94] an immediate-early gene highly enriched at excitatory synapses on PV cells, where we observed the most drastic phenotype. Furthermore, deletion of Nptx2 caused increased activation of the classical complement pathway and microglia-mediated elimination of excitatory synapses on PV cells,[94] supporting this established mechanism of synaptic loss in excitatory inputs on PV neurons. Still, other non-glia mechanisms could underlie excitatory synaptic loss in interneurons. In support of this, our group[95] used STED imaging in mPFC slices[96] to demonstrate that increased levels of mC4 accelerate the accumulation of the postsynaptic receptor GluR1 in neuronal LAMP1-positive lysosomes, leading to pathological synaptic loss.

In contrast to the alterations observed with elevated levels of mC4 in PV cells, pan-neuronal overexpression of mC4 did not lead to increased sex-dependent anxiety-like behavior or deficits in the excitatory drive to PV cells. Although this result may seem unexpected, it is evidence that specific insults to PV cells are especially detrimental during brain development. One plausible scenario is that increased levels of mC4 in PV cells lead to alterations in the dynamics of excitation and inhibition. However, in the PanN-mC4-KI mouse, there is a hypothetical global decrease in the excitatory and inhibitory synaptic drive. Future research should ascertain whether developmental mechanisms are better equipped to compensate for insults affecting global rather than cell-type-specific C4 functions that could differentially impact the dynamics of excitation and inhibition. Lastly, it is possible that pan-neuronal mC4 alterations lead to perturbations in other neuronal circuits or behaviors that were not measured in this study. In support of this, previous work from our lab[34] and others[41,42] found that increased levels of C4 alter social and cognitive behaviors in mice.

The mPFC and neuropsychiatric disorders

The lifetime prevalence of anxiety disorders is close to 30%[97] and it is highly comorbid with other neuropsychiatric disorders, including SCZ.[59,98,99] Our approach of conditionally targeting mC4 in fast-spiking cells provides a unique example that establishes a causal relation between elevated levels of the SCZ-associated gene, *C4*, in these cells and increased anxiety-like behavior and mPFC circuit dysfunction in male mice, shedding light on the intricate dynamics of neuropsychiatric disorders.

We have focused on the mPFC to establish a connection between altered circuitry and disrupted emotional behavior. Not only have many of the synaptic deficits observed in patients with SCZ been identified specifically in the PFC,[22,71] but genetic insults and chronic stress have lasting effects on the PFC that lead to alterations in cognitive and social function.[34,100–102] In the mouse mPFC, inhibitory neurons respond to a variety of social and emotional stimuli.[103,104] Additionally, PV cells coordinate and enhance the neuronal activity of PFC projection neurons to drive fear expression in the mouse.[105] Consistent with its function in regulating emotional behavior, we observed that the increased levels of mC4 in PV neurons lead to synaptic alterations in fast-spiking cells and opposing effects in the excitability of cortical cells in male and female mice.

The PFC plays a crucial role in social cognition, enabling us to understand and interpret the actions of others, which is fundamental for effective social interaction.[106,107] Here, we show that while increased levels of mC4 in PV cells did not cause a drastic deficit in social behavior, overexpressing mice exhibited deficits in subclasses of exploratory social behavior, linking defects in inhibitory circuits to the initiation of social behaviors. In support of the role of mPFC PV neurons in the regulation of social behavior, Bicks et al.[108] demonstrated that PV cell activity in the mPFC preceded an active social episode, or an episode initiated by the experimental mouse. Similarly, we showed that increased levels of mC4 in PV cells lead to deficits in active but not passive social interactions. Finally, in contrast to the deficits in anxiety-like behavior, mC4-driven social deficits were not sexually dimorphic, suggesting that in mice social deficits might have a distinct etiology from pathological anxiety-like behavior.

Complement dysfunction and the mPFC

Although there is a strong link between immune dysfunction and neuropsychiatric disorders,[51,109–114] more research is needed to establish a connection between complement dysfunction and specific circuitry underlying emotional behavior. Disruption of Csmd1, which is a C4 inhibitor, induces behaviors reminiscent of blunted emotional responses, anxiety, and depression.[115] Additionally, Crider et al.[116] found a significant increase in C3 expression, a downstream effector of C4, in the PFC of depressed suicide subjects. Together with previous results,[34,41] we showed that mC4 alterations in specific cell-types are linked to mPFC-related pathologies. In summary, these results suggest that the PFC is a brain region susceptible to pathological complement activity.

Sex-dependent nature of schizophrenia pathology, complement, and PV cells

Using a new mouse model, we show that targeted OE of mC4, specifically in fast-spiking cells, induces pathological anxiety-like behavior in male mice while sparing females. While the prevalence of anxiety disorders tends to be greater in females than in males,[117–119] it is unclear how the mechanisms driving anxiety disorders may differ from those driving the comorbid anxiety experienced by SCZ patients. Furthermore, it is unclear whether the anxiety experienced by individuals with SCZ is driven by the severity of their symptoms, which may be more significant in males. In humans, there is a marked divergence in the incidence, severity of symptoms, and age of onset of SCZ in males compared to females. This sex-dependent imbalance is most obvious in the prevalence of SCZ between sexes, impacting men vs. women at a rate of roughly 1.4:1[120,121] but is further supported by an earlier onset of symptoms, higher risk, and poorer functional outcome in males.[122–125] Anxiety, specifically, while a common component of SCZ symptomatology, is relatively understudied compared to the positive, negative, and cognitive deficits that have been more widely studied.[61] As such, sex-specific features of comorbid anxiety in SCZ patients are not well understood, and thus, our work provides unique insight into potential sex differences upon manipulation of an SCZ-risk gene.

In humans, there are differences in the complement pathway and the levels of specific complement proteins based on sex. For example, Kamitaki et al. (2020) have shown that the SCZ odds ratio for the four most common *C4* alleles is all higher in men than in women. Additionally, at the protein level, both C4 and its effector, C3, were present at higher levels in the cerebrospinal fluid of men than in women ages 20–50.[126] These findings indicate that there are variations in complement levels depending on sex. As the levels of overexpressed mC4 in our new model are the same between males and females, we concluded that the differences in PV-mC4-KI mice are most likely due to downstream sex-dependent alterations in the machinery that regulates synaptic plasticity.

There are also several sexually dimorphic features of PV function and their response to stress that may be contributing to the results presented in this paper. Not only has the developmental trajectory of PV expression in mice been shown to differ between males and females,[127] but GABA turnover and GABA synthesis in rats are both greater in males than in females.[128] Additionally, during development, the maturation of fast-spiking cells contributes to the wiring of the neural networks, controlling the critical window of plasticity.[129–132] Therefore, alterations in the developmental plasticity windows driven by increased levels of mC4 in PV cells may cause the synaptic and excitability deficits we observed in the mPFC. There are also sex-dependent differences in the developmental cortical mechanisms of plasticity,[133] which are regulated, in part, by PV cell activity, including their feedforward circuits.[130,131]

Of note, microglia activity, which is triggered by complement activation, is sexually dimorphic.[134] In addition, microglia size, density, and resting membrane potential tend to be greater in males than in females, as do class I and II MHC expression in microglia in the cortex, supporting a higher antigen-presenting potential in male mice.[135] These numerous sex-divergent features of microglia are especially relevant here, where microglia-dependent synaptic engulfment is an established mechanism for complement-driven synaptic loss in the normal and diseased brain.[51,85–87] Thus, sexually divergent microglia activity could drive differences in PV cell synaptic elimination between males and females.

Interestingly, there are other mechanisms by which microglia can control synaptic connectivity outside of engulfment, primarily through the secretion of synaptogenic factors that promote synapse formation. For example, the elimination of microglia has been shown to drive learning deficits and reduce synapse formation in mice, a finding replicated when microglial release of brain-derived neurotrophic factor (BDNF) specifically was prevented.[136] Because BDNF has been shown to have sex-specific features and effects in the brain,[137,138] its release by microglia is notable in this context. Moreover, interleukin 10 (IL-10), a cytokine released by microglia, has been shown to induce synapse formation.[139] Potential sex-dependent changes in its release by microglia could certainly drive changes in synaptogenesis in a sexually dimorphic fashion. Finally, direct contact between microglia and dendrites has been shown to drive the formation of filopodia,[140] flexible, transient dendritic spines that orchestrate synapse formation.[141–143] Thus, sex-dependent differences in microglia could certainly drive sexually dimorphic alterations to synapse formation.

It is not clear how, for example, the same genetic manipulation, i.e., increased levels of mC4 in PV cells, could lead to no synaptic effects in females or opposing sex-dependent deficits in the excitability of cortical cells. Since mC4 levels were overexpressed similarly in males and females, our data suggest that the downstream molecular machinery that is receptive to or activated by mC4 is dependent on sex. Alternatively, the different phenotypes observed with increased levels of mC4 are not dependent on the sensitivity of the molecular machinery or neuroimmune pathways of males and females but on differences in developmental compensatory mechanisms between sexes.

Alterations in temporal fidelity and neural communication in SCZ and other neuropsychiatric disease

Using simulations, we showed a significant decrease in the FR of PV model cells and hyperactivity of PYR model cells in the male KI network compared to the male WT network. More critically, we also showed a significant broadening of the lag times over which activity in the presynaptic PYR influences the postsynaptic PYR, a product of defunct inhibition. This deficit in inhibition was evident in the drastic reduction of firing rates of PV2 in the male KI network and was bolstered by a reduction in the PYR1 → PV2 TE compared to that of the male WT network.

During development, neuronal networks are far from static; an ever-dynamic landscape, synaptic connections are constantly being formed, lost, strengthened, or weakened across development.[144–146] The fundamental unit of this plasticity is the information transferred from the presynaptic partner to its postsynaptic partner(s), the efficacy or existence of this connection being largely an activity-dependent factor.[145,147] Moreover, disruptions in spike-timing and consequential deficits in synaptic plasticity are core features of neuropsychiatric diseases, including SCZ.[29,148–151]

Thus, the specific finding of increased PYR1 → PYR2 TE across a broader lag-time window in the male KI network is of particular importance because it suggests a major disruption in the temporal precision of effective information flow. In support of this, disruption of SCZ-associated risk genes that specifically contribute to spike-timing and plasticity in animal models have been shown to evoke a broad spectrum of SCZ-associated behavioral and synaptic deficits.[152–155]

In the case of the female WT and KI networks, a seemingly incompatible result emerged whereby, despite a lack of change in the PV2 FR, the FR of PYR2 was reduced in the KI female condition. However, we observed a significant increase in the PYR1 → PV2 TE in the female KI network that, despite not resulting in a change in the overall number of spikes evoked in PV2, shaped the temporal sequence of when those spikes of PV2 occurred more precisely. As a result, the effective inhibition experienced by PYR2 aligned more strongly with the excitation to PYR2 (from PYR1) in time, leading to an overall decrease in PYR2 FR.

Relevant to several broader hypotheses of SCZ is the convergence of altered neural communication and temporal fidelity. Using the specific experimental changes in intrinsic excitability and synaptic connectivity associated with PV-mC4-OE to guide our computational model, we too were led to exactly this same point of convergence. From the decades-enduring synaptic hypothesis of SCZ first proposed by Irwin Feinberg[70] to modern hypotheses of NMDAR hypofunction,[82,150,156] many of the dominating views of SCZ pathogenesis feature disruptions in spike-timing and resultant deficits in the effective flow of information from one neuron to the next. Moreover, computational models of brain dysfunction relevant to SCZ from other groups consistently converge on this same feature.[150]

Separately, Murray et al.[157] implemented synaptic disinhibition—similar to our model of PV hypofunction—in a local-circuit PFC network model and found that this manipulation caused an increase in PYR FR (as in our model), broadened network activity, and decreased memory precision. Overall, our simulation provides evidence that a genetic alteration in fast-spiking cells leads to unique sex-dependent phenotypes in a model network, highlighting how cellular and synaptic phenotypes interact to produce complex neural network deficits in diseased states.

Limitations of the study

We used a unique genetic approach to increase levels of mC4 in PV cells globally. However, besides the PFC, we did not include recordings in other brain regions related to emotional regulation. Alterations in the inhibitory microcircuitry of other anxiety-related areas may underlie the behavioral effects that we have captured.[158,159] Nevertheless, our findings demonstrate that conditional overexpression of mC4 in fast-spiking cells results in synaptic and excitability deficits that are consistent with the role of mPFC PV cells in regulating emotional behavior.

SCZ is a complex disorder, and it is likely that multiple genetic and non-genetic factors contribute to its pathogenesis, each potentially impacting synaptic function and the excitability of cortical cells in different but converging ways. In light of this caveat, we provide a new mouse model where complement dysfunction in PV cells causes cellular and behavioral dysfunction reminiscent of PFC-associated neurological conditions.

While we used a computational model to understand better how the experimental results we gathered may cause network-level deficits in an intact system, our model has several limitations. First, the model has a simple architecture with strictly feedforward connections. Thus, our ability to capture complex network interactions was limited. Moreover, the model was composed of only four interconnected model neurons, a drastic simplification of the rich connectivity profiles of these cells in the intact rodent brain. Finally, the weights for all synaptic connections were altered in accordance with relative changes observed in the experimental mPSC data recorded in PYRs and PV cells in acute brain slices. However, these changes might not reflect *in vivo* properties. Nevertheless, despite these simplifications and limitations, our simulation of a network with increased levels of mC4 in male fast-spiking cells is consistent with previous models of disrupted neuronal communication and prefrontal circuit dysfunction in schizophrenia.[148]

Closing remarks

Here, we have generated a unique mouse model to overexpress mC4 conditionally. Diseases linked to increased C4 levels often have autoimmune or inflammatory aspects. Therefore, this mouse can be used to target specific cell types and tissues to determine the role of this important gene in various diseases outside of the nervous system or test the efficacy of pharmacology to target complement-related diseases. Together with previous studies, we have established C4 as an important regulator of pathological synaptic loss in the prefrontal cortex, a region associated with several neuropsychiatric disorders. Furthermore, by conditionally overexpressing mC4 in fast-spiking cells, we have identified a connection between dysfunction of inhibitory circuits in the prefrontal cortex and pathological anxiety-like behavior in male mice.

RESOURCE AVAILABILITY

Lead contact

Any additional information or requests for resources pertaining to this research should be directed to and will be satisfied by the lead contact, Dr. Alberto Cruz-Martín (alberto.cruzmartin@cuanschutz.edu).

Materials availability

This study did not generate unique reagents.

Data and code availability

- Data reported in this paper are available https://osf.io/je38k/.
- Custom-written routines are available at https://github.com/CruzMartinLab.
- Any additional information required to reanalyze the data reported in this paper is available from the lead contact upon request.

ACKNOWLEDGMENTS

We want to thank Dr. Todd Blute and the Boston University Biology Imaging Core for providing support for the confocal microscope. We thank members of the Cruz-Martín lab for critical reading of the manuscript and helpful discussions. This work was supported by a National Institutes of Health R01 (NIMH, 5R01MH129732-02) and an industry grant (to generate mC4-KI mouse, Biogen, #55206943) to A.C-M., a Brenton R. Lutz Award to R.A.P., a SURF/NSF-REU program (NSF, REU grant IOS-1659605) to J.R.G. and N.M.P.L., and an NSF Award #2319321 to K.S.

AUTHOR CONTRIBUTIONS

L.A.F. and A.C-M. conceptualized experiments, including formulating the composition, goals, and scope of the paper, as well as the approaches for analysis. L.A.F., R.A.P., M.S., A.B., S.B., J.R.G., and N.M.P.L. collected the data and performed experiments. L.A.F. and R.A.P. performed data curation. L.A.F., R.A.P., A.B., M.S., and A.C.M. analyzed data. L.A.F. and R.A.P. contributed code for data analysis. L.A.F. and A.C-M. contributed to parts of the original draft, including figure design and generation. L.A.F. developed the computational model with the support of J.C.N. and K.S. All authors contributed to the revision and editing of the draft. A.C-M. obtained funding and supervised the project, providing mentorship, oversight, and project administration.

DECLARATION OF INTERESTS

The authors declare that they have no competing interests.

DECLARATION OF GENERATIVE AI AND AI-ASSISTED TECHNOLOGIES IN THE WRITING PROCESS

The authors declare that no AI or AI-assisted technologies were used in the writing process.

STAR★METHODS

Detailed methods are provided in the online version of this paper and include the following:

- KEY RESOURCES TABLE
- EXPERIMENTAL MODEL AND STUDY PARTICIPANT DETAILS
  - Generation of the mC4-KI mouse

  - ○ Breeding
  - ○ Ethics statement
- METHOD DETAILS
  - ○ Multiplex fluorescence *in situ* hybridization
  - ○ PV cell density
  - ○ PV cell synaptic puncta
  - ○ Behavior
  - ○ Anxiety-related assays
  - ○ Sociability assays
  - ○ Behavior analysis
  - ○ Neonatal viral injections
  - ○ Electrophysiology
  - ○ Computational model
- QUANTIFICATION AND STATISTICAL ANALYSIS

SUPPLEMENTAL INFORMATION

Supplemental information can be found online at https://doi.org/10.1016/j.isci.2024.110800.

Received: April 30, 2024
Revised: July 9, 2024
Accepted: August 20, 2024
Published: August 30, 2024

REFERENCES

1. Ferguson, B.R., and Gao, W.-J. (2018). PV Interneurons: Critical Regulators of E/I Balance for Prefrontal Cortex-Dependent Behavior and Psychiatric Disorders. Front. Neural Circuits *12*, 37. https://doi.org/10.3389/fncir.2018.00037.
2. Hu, H., Gan, J., and Jonas, P. (2014). Fast-spiking, parvalbumin+ GABAergic interneurons: From cellular design to microcircuit function. Science *345*, 1255263. https://doi.org/10.1126/science.1255263.
3. Rudy, B., Fishell, G., Lee, S., and Hjerling-Leffler, J. (2011). Three Groups of Interneurons Account for Nearly 100% of Neocortical GABAergic Neurons. Dev. Neurobiol. *71*, 45–61. https://doi.org/10.1002/dneu.20853.
4. Cardin, J.A. (2018). Inhibitory interneurons regulate temporal precision and correlations in cortical circuits. Trends Neurosci. *41*, 689–700. https://doi.org/10.1016/j.tins.2018.07.015.
5. Nocon, J.C., Gritton, H.J., James, N.M., Mount, R.A., Qu, Z., Han, X., and Sen, K. (2023). Parvalbumin neurons enhance temporal coding and reduce cortical noise in complex auditory scenes. Commun. Biol. *6*, 751–814. https://doi.org/10.1038/s42003-023-05126-0.
6. Massi, L., Lagler, M., Hartwich, K., Borhegyi, Z., Somogyi, P., and Klausberger, T. (2012). Temporal Dynamics of Parvalbumin-Expressing Axo-axonic and Basket Cells in the Rat Medial Prefrontal Cortex In Vivo. J. Neurosci. *32*, 16496–16502. https://doi.org/10.1523/JNEUROSCI.3475-12.2012.
7. Wilent, W.B., and Contreras, D. (2005). Dynamics of excitation and inhibition underlying stimulus selectivity in rat somatosensory cortex. Nat. Neurosci. *8*, 1364–1370. https://doi.org/10.1038/nn1545.
8. Jelitai, M., Puggioni, P., Ishikawa, T., Rinaldi, A., and Duguid, I. (2016). Dendritic excitation–inhibition balance shapes cerebellar output during motor behaviour. Nat. Commun. *7*, 13722. https://doi.org/10.1038/ncomms13722.
9. Lam, N.H., Borduqui, T., Hallak, J., Roque, A., Anticevic, A., Krystal, J.H., Wang, X.-J., and Murray, J.D. (2022). Effects of Altered Excitation-Inhibition Balance on Decision Making in a Cortical Circuit Model. J. Neurosci. *42*, 1035–1053. https://doi.org/10.1523/JNEUROSCI.1371-20.2021.
10. Buzsáki, G., and Wang, X.-J. (2012). Mechanisms of Gamma Oscillations. Annu. Rev. Neurosci. *35*, 203–225. https://doi.org/10.1146/annurev-neuro-062111-150444.
11. Howard, M.W., Rizzuto, D.S., Caplan, J.B., Madsen, J.R., Lisman, J., Aschenbrenner-Scheibe, R., Schulze-Bonhage, A., and Kahana, M.J. (2003). Gamma Oscillations Correlate with Working Memory Load in Humans. Cereb. Cortex *13*, 1369–1374. https://doi.org/10.1093/cercor/bhg084.
12. Guan, A., Wang, S., Huang, A., Qiu, C., Li, Y., Li, X., Wang, J., Wang, Q., and Deng, B. (2022). The role of gamma oscillations in central nervous system diseases: Mechanism and treatment. Front. Cell. Neurosci. *16*, 962957.
13. Sohal, V.S., Zhang, F., Yizhar, O., and Deisseroth, K. (2009). Parvalbumin neurons and gamma rhythms enhance cortical circuit performance. Nature *459*, 698–702. https://doi.org/10.1038/nature07991.
14. Kim, K.M., Bong, S.H., Byeon, J., and Kim, J.W. (2022). State and Trait Anxiety Related Gamma Oscillations in Patients With Anxiety Within the Research Domain Criteria Framework. Psychiatry Investig. *19*, 443–450. https://doi.org/10.30773/pi.2022.0011.
15. Lewis, D.A., Hashimoto, T., and Volk, D.W. (2005). Cortical inhibitory neurons and schizophrenia. Nat. Rev. Neurosci. *6*, 312–324. https://doi.org/10.1038/nrn1648.
16. Spencer, K.M., Nestor, P.G., Niznikiewicz, M.A., Salisbury, D.F., Shenton, M.E., and McCarley, R.W. (2003). Abnormal Neural Synchrony in Schizophrenia. J. Neurosci. *23*, 7407–7411. https://doi.org/10.1523/JNEUROSCI.23-19-07407.2003.
17. Murty, D.V., Manikandan, K., Kumar, W.S., Ramesh, R.G., Purokayastha, S., Nagendra, B., ML, A., Balakrishnan, A., Javali, M., Rao, N.P., and Ray, S. (2021). Stimulus-induced gamma rhythms are weaker in human elderly with mild cognitive impairment and Alzheimer's disease. Elife *10*, e61666. https://doi.org/10.7554/eLife.61666.
18. Traikapi, A., and Konstantinou, N. (2021). Gamma Oscillations in Alzheimer's Disease and Their Potential Therapeutic Role. Front. Syst. Neurosci. *15*, 782399.
19. Fagiolini, M., Fritschy, J.-M., Löw, K., Möhler, H., Rudolph, U., and Hensch, T.K. (2004). Specific GABAA circuits for visual cortical plasticity. Science *303*, 1681–1683. https://doi.org/10.1126/science.1091032.
20. Canetta, S.E., Holt, E.S., Benoit, L.J., Teboul, E., Sahyoun, G.M., Ogden, R.T., Harris, A.Z., and Kellendonk, C. (2022). Mature parvalbumin interneuron function in prefrontal cortex requires activity during a postnatal sensitive period. Elife *11*, e80324. https://doi.org/10.7554/eLife.80324.
21. Jiang, B., Huang, Z.J., Morales, B., and Kirkwood, A. (2005). Maturation of GABAergic transmission and the timing of plasticity in visual cortex. Brain Res. Rev. *50*, 126–133. https://doi.org/10.1016/j.brainresrev.2005.05.007.
22. Chung, D.W., Fish, K.N., and Lewis, D.A. (2016). Pathological basis for deficient excitatory drive to cortical parvalbumin interneurons in schizophrenia. Am. J. Psychiatry *173*, 1131–1139. https://doi.org/10.1176/appi.ajp.2016.16010025.
23. Toker, L., Mancarci, B.O., Tripathy, S., and Pavlidis, P. (2018). Transcriptomic evidence for alterations in astrocytes and parvalbumin interneurons in bipolar disorder and schizophrenia subjects. Biol. Psychiatry *84*, 787–796. https://doi.org/10.1016/j.biopsych.2018.07.010.
24. Akbarian, S., and Huang, H.-S. (2006). Molecular and cellular mechanisms of altered GAD1/GAD67 expression in schizophrenia and related disorders. Brain Res. Rev. *52*, 293–304. https://doi.org/10.1016/j.brainresrev.2006.04.001.
25. Beneyto, M., Abbott, A., Hashimoto, T., and Lewis, D.A. (2011). Lamina-Specific Alterations in Cortical GABAA Receptor

Subunit Expression in Schizophrenia. Cereb. Cortex *21*, 999–1011. https://doi.org/10.1093/cercor/bhq169.

26. del Pino, I., García-Frigola, C., Dehorter, N., Brotons-Mas, J.R., Alvarez-Salvado, E., Martínez de Lagrán, M., Ciceri, G., Gabaldón, M.V., Moratal, D., Dierssen, M., et al. (2013). Erbb4 Deletion from Fast-Spiking Interneurons Causes Schizophrenia-like Phenotypes. Neuron *79*, 1152–1168. https://doi.org/10.1016/j.neuron.2013.07.010.
27. Chung, D.W., Wills, Z.P., Fish, K.N., and Lewis, D.A. (2017). Developmental pruning of excitatory synaptic inputs to parvalbumin interneurons in monkey prefrontal cortex. Proc. Natl. Acad. Sci. USA *114*, E629–E637. https://doi.org/10.1073/pnas.1610077114.
28. Seshadri, S., Faust, T., Ishizuka, K., Delevich, K., Chung, Y., Kim, S.-H., Cowles, M., Niwa, M., Jaaro-Peled, H., Tomoda, T., et al. (2015). Interneuronal DISC1 regulates NRG1-ErbB4 signalling and excitatory–inhibitory synapse formation in the mature cortex. Nat. Commun. *6*, 10118. https://doi.org/10.1038/ncomms10118.
29. Ripke, S., Neale, B.M., Corvin, A., Walters, J.T., Farh, K.-H., Holmans, P.A., Lee, P., Bulik-Sullivan, B., Collier, D.A., Huang, H., et al. (2014). Biological Insights From 108 Schizophrenia-Associated Genetic Loci. Nature *511*, 421–427. https://doi.org/10.1038/nature13595.
30. Mokhtari, R., and Lachman, H.M. (2016). The Major Histocompatibility Complex (MHC) in Schizophrenia: A Review. J. Clin. Cell. Immunol. *7*, 479. https://doi.org/10.4172/2155-9899.1000479.
31. Li, J., Yoshikawa, A., Alliey-Rodriguez, N., and Meltzer, H.Y. (2022). Schizophrenia risk loci from xMHC region were associated with antipsychotic response in chronic schizophrenic patients with persistent positive symptom. Transl. Psychiatry *12*, 92–99. https://doi.org/10.1038/s41398-022-01854-9.
32. Datwani, A., McConnell, M.J., Kanold, P.O., Micheva, K.D., Busse, B., Shamloo, M., Smith, S.J., and Shatz, C.J. (2009). Classical MHCI Molecules Regulate Retinogeniculate Refinement and Limit Ocular Dominance Plasticity. Neuron *64*, 463–470. https://doi.org/10.1016/j.neuron.2009.10.015.
33. Sekar, A., Bialas, A.R., de Rivera, H., Davis, A., Hammond, T.R., Kamitaki, N., Tooley, K., Presumey, J., Baum, M., Van Doren, V., et al. (2016). Schizophrenia risk from complex variation of complement component 4. Nature *530*, 177–183. https://doi.org/10.1038/nature16549.
34. Comer, A.L., Jinadasa, T., Sriram, B., Phadke, R.A., Kretsge, L.N., Nguyen, T.P.H., Antognetti, G., Gilbert, J.P., Lee, J., Newmark, E.R., et al. (2020). Increased expression of schizophrenia-associated gene C4 leads to hypoconnectivity of prefrontal cortex and reduced social interaction. PLoS Biol. *18*, e3000604. https://doi.org/10.1371/journal.pbio.3000604.
35. MacDonald, A.W., Carter, C.S., Kerns, J.G., Ursu, S., Barch, D.M., Holmes, A.J., Stenger, V.A., and Cohen, J.D. (2005). Specificity of Prefrontal Dysfunction and Context Processing Deficits to Schizophrenia in Never-Medicated Patients With First-Episode Psychosis. Am. J. Psychiatry *162*, 475–484. https://doi.org/10.1176/appi.ajp.162.3.475.
36. Green, M.F., Horan, W.P., and Lee, J. (2015). Social cognition in schizophrenia. Nat. Rev. Neurosci. *16*, 620–631. https://doi.org/10.1038/nrn4005.
37. Selemon, L.D., and Zecevic, N. (2015). Schizophrenia: a tale of two critical periods for prefrontal cortical development. Transl. Psychiatry *5*, e623. https://doi.org/10.1038/tp.2015.115.
38. Pizzagalli, D.A., and Roberts, A.C. (2022). Prefrontal cortex and depression. Neuropsychopharmacology *47*, 225–246. https://doi.org/10.1038/s41386-021-01101-7.
39. Gamo, N.J., and Arnsten, A.F.T. (2011). Molecular Modulation of Prefrontal Cortex: Rational Development of Treatments for Psychiatric Disorders. Behav. Neurosci. *125*, 282–296. https://doi.org/10.1037/a0023165.
40. Kenwood, M.M., Kalin, N.H., and Barbas, H. (2022). The prefrontal cortex, pathological anxiety, and anxiety disorders. Neuropsychopharmacology *47*, 260–275. https://doi.org/10.1038/s41386-021-01109-z.
41. Druart, M., Nosten-Bertrand, M., Poll, S., Crux, S., Nebeling, F., Delhaye, C., Dubois, Y., Mittag, M., Leboyer, M., Tamouza, R., et al. (2021). Elevated expression of complement C4 in the mouse prefrontal cortex causes schizophrenia-associated phenotypes. Mol. Psychiatry *26*, 3489–3501. https://doi.org/10.1038/s41380-021-01081-6.
42. Yilmaz, M., Yalcin, E., Presumey, J., Aw, E., Ma, M., Whelan, C.W., Stevens, B., McCarroll, S.A., and Carroll, M.C. (2021). Overexpression of schizophrenia susceptibility factor human complement C4A promotes excessive synaptic loss and behavioral changes in mice. Nat. Neurosci. *24*, 214–224. https://doi.org/10.1038/s41593-020-00763-8.
43. Kumar, P., Goettemoeller, A.M., Espinosa-Garcia, C., Tobin, B.R., Tfaily, A., Nelson, R.S., Natu, A., Dammer, E.B., Santiago, J.V., Malepati, S., et al. (2023). Native-state proteomics of Parvalbumin interneurons identifies novel molecular signatures and metabolic vulnerabilities to early Alzheimer's disease pathology. Preprint at bioRxiv. https://doi.org/10.1101/2023.05.17.541038.
44. Kann, O., Papageorgiou, I.E., and Draguhn, A. (2014). Highly Energized Inhibitory Interneurons are a Central Element for Information Processing in Cortical Networks. J. Cereb. Blood Flow Metab. *34*, 1270–1282. https://doi.org/10.1038/jcbfm.2014.104.
45. Ruden, J.B., Dugan, L.L., and Konradi, C. (2021). Parvalbumin interneuron vulnerability and brain disorders. Neuropsychopharmacology *46*, 279–287. https://doi.org/10.1038/s41386-020-0778-9.
46. Whittaker, R.G., Turnbull, D.M., Whittington, M.A., and Cunningham, M.O. (2011). Impaired mitochondrial function abolishes gamma oscillations in the hippocampus through an effect on fast-spiking interneurons. Brain *134*, e180–e181. https://doi.org/10.1093/brain/awr018.
47. Gulyás, A.I., Megías, M., Emri, Z., and Freund, T.F. (1999). Total Number and Ratio of Excitatory and Inhibitory Synapses Converging onto Single Interneurons of Different Types in the CA1 Area of the Rat Hippocampus. J. Neurosci. *19*, 10082–10097. https://doi.org/10.1523/JNEUROSCI.19-22-10082.1999.
48. Mackenzie-Gray Scott, C.A., Pelkey, K.A., Caccavano, A.P., Abebe, D., Lai, M., Black, K.N., Brown, N.D., Trevelyan, A.J., and McBain, C.J. (2022). Resilient Hippocampal Gamma Rhythmogenesis and Parvalbumin-Expressing Interneuron Function Before and After Plaque Burden in 5xFAD Alzheimer's Disease Model. Front. Synaptic Neurosci. *14*, 857608.
49. Palop, J.J., and Mucke, L. (2016). Network abnormalities and interneuron dysfunction in Alzheimer disease. Nat. Rev. Neurosci. *17*, 777–792. https://doi.org/10.1038/nrn.2016.141.
50. Contractor, A., Ethell, I.M., and Portera-Cailliau, C. (2021). Cortical interneurons in autism. Nat. Neurosci. *24*, 1648–1659. https://doi.org/10.1038/s41593-021-00967-6.
51. Comer, A.L., Carrier, M., Tremblay, M.È., and Cruz-Martín, A. (2020). The Inflamed Brain in Schizophrenia: The Convergence of Genetic and Environmental Risk Factors That Lead to Uncontrolled Neuroinflammation. Front. Cell. Neurosci. *14*, 274. https://doi.org/10.3389/fncel.2020.00274.
52. Dolatshad, H., Biggs, D., Diaz, R., Hortin, N., Preece, C., and Davies, B. (2015). A versatile transgenic allele for mouse overexpression studies. Mamm. Genome *26*, 598–608. https://doi.org/10.1007/s00335-015-9602-y.
53. Fischer, M.B., Ma, M., Goerg, S., Zhou, X., Xia, J., Finco, O., Han, S., Kelsoe, G., Howard, R.G., Rothstein, T.L., et al. (1996). Regulation of the B cell response to T-dependent antigens by classical pathway complement. J. Immunol. Baltim. Md, 549–556.
54. Hitoshi, N., Ken-ichi, Y., and Jun-ichi, M. (1991). Efficient selection for high-expression transfectants with a novel eukaryotic vector. Gene *108*, 193–199. https://doi.org/10.1016/0378-1119(91)90434-D.
55. Jun-ichi, M., Satoshi, T., Kimi, A., Fumi, T., Akira, T., Kiyoshi, T., and Ken-ichi, Y. (1989). Expression vector system based on the chicken β-actin promoter directs efficient production of interleukin-5. Gene *79*, 269–277. https://doi.org/10.1016/0378-1119(89)90209-6.
56. Forni, P.E., Scuoppo, C., Imayoshi, I., Taulli, R., Dastrù, W., Sala, V., Betz, U.A.K., Muzzi, P., Martinuzzi, D., Vercelli, A.E., et al. (2006). High levels of Cre expression in neuronal progenitors cause defects in brain development leading to microencephaly and hydrocephaly. J. Neurosci. *26*, 9593–9602. https://doi.org/10.1523/JNEUROSCI.2815-06.2006.
57. Baghdadi, M., Mesaros, A., Purrio, M., and Partridge, L. (2023). Sex-specific effects of Cre expression in Syn1Cre mice. Sci. Rep. *13*, 10037. https://doi.org/10.1038/s41598-023-37029-9.
58. Patel, K.R., Cherian, J., Gohil, K., and Atkinson, D. (2014). Schizophrenia: Overview and Treatment Options. P T. *39*, 638–645.
59. Braga, R.J., Reynolds, G.P., and Siris, S.G. (2013). Anxiety comorbidity in schizophrenia. Psychiatry Res. *210*, 1–7. https://doi.org/10.1016/j.psychres.2013.07.030.
60. Kiran, C., and Chaudhury, S. (2016). Prevalence of comorbid anxiety disorders in

schizophrenia. Ind. Psychiatry J. *25*, 35–40. https://doi.org/10.4103/0972-6748.196045.

61. Hall, J. (2017). Schizophrenia — an anxiety disorder? Br. J. Psychiatry *211*, 262–263. https://doi.org/10.1192/bjp.bp.116.195370.
62. George, M., Maheshwari, S., Chandran, S., Manohar, J.S., and Sathyanarayana Rao, T.S. (2017). Understanding the schizophrenia prodrome. Indian J. Psychiatry *59*, 505–509. https://doi.org/10.4103/psychiatry.IndianJPsychiatry_464_17.
63. Guilloux, J.-P., Seney, M., Edgar, N., and Sibille, E. (2011). Integrated Behavioral Z-Scoring Increases the Sensitivity and Reliability of Behavioral Phenotyping in mice: Relevance to Emotionality and Sex. J. Neurosci. Methods *197*, 21–31. https://doi.org/10.1016/j.jneumeth.2011.01.019.
64. Traynelis, S.F., Wollmuth, L.P., McBain, C.J., Menniti, F.S., Vance, K.M., Ogden, K.K., Hansen, K.B., Yuan, H., Myers, S.J., and Dingledine, R. (2010). Glutamate Receptor Ion Channels: Structure, Regulation, and Function. Pharmacol. Rev. *62*, 405–496. https://doi.org/10.1124/pr.109.002451.
65. Williams, S.R., and Stuart, G.J. (2003). Role of dendritic synapse location in the control of action potential output. Trends Neurosci. *26*, 147–154. https://doi.org/10.1016/S0166-2236(03)00035-3.
66. Alberto, C.O., and Hirasawa, M. (2010). AMPA receptor-mediated miniature EPSCs have heterogeneous time courses in orexin neurons. Biochem. Biophys. Res. Commun. *400*, 707–712. https://doi.org/10.1016/j.bbrc.2010.08.132.
67. Zhan, X., Cao, M., Yoo, A.S., Zhang, Z., Chen, L., Crabtree, G.R., and Wu, J.I. (2015). Generation of BAF53b-Cre transgenic mice with pan-neuronal Cre activities. Genesis *53*, 440–448. https://doi.org/10.1002/dvg.22866.
68. Olave, I., Wang, W., Xue, Y., Kuo, A., and Crabtree, G.R. (2002). Identification of a polymorphic, neuron-specific chromatin remodeling complex. Genes Dev. *16*, 2509–2517. https://doi.org/10.1101/gad.992102.
69. Sherfey, J.S., Soplata, A.E., Ardid, S., Roberts, E.A., Stanley, D.A., Pittman-Polletta, B.R., and Kopell, N.J. (2018). DynaSim: A MATLAB Toolbox for Neural Modeling and Simulation. Front. Neuroinform. *12*, 10.
70. Feinberg, I. (1982). Schizophrenia: Caused by a fault in programmed synaptic elimination during adolescence? J. Psychiatr. Res. *17*, 319–334. https://doi.org/10.1016/0022-3956(82)90038-3.
71. Glantz, L.A., and Lewis, D.A. (2000). Decreased Dendritic Spine Density on Prefrontal Cortical Pyramidal Neurons in Schizophrenia. Arch. Gen. Psychiatry *57*, 65–73. https://doi.org/10.1001/archpsyc.57.1.65.
72. Garey, L.J., Ong, W.Y., Patel, T.S., Kanani, M., Davis, A., Mortimer, A.M., Barnes, T.R., and Hirsch, S.R. (1998). Reduced dendritic spine density on cerebral cortical pyramidal neurons in schizophrenia. J. Neurol. Neurosurg. Psychiatry *65*, 446–453. https://doi.org/10.1136/jnnp.65.4.446.
73. Chung, D.W., Volk, D.W., Arion, D., Zhang, Y., Sampson, A.R., and Lewis, D.A. (2016). Dysregulated ErbB4 Splicing in Schizophrenia: Selective Effects on Parvalbumin Expression. Am. J. Psychiatry *173*, 60–68. https://doi.org/10.1176/appi.ajp.2015.15020150.
74. Caccavano, A., Bozzelli, P.L., Forcelli, P.A., Pak, D.T.S., Wu, J.-Y., Conant, K., and Vicini, S. (2020). Inhibitory Parvalbumin Basket Cell Activity is Selectively Reduced during Hippocampal Sharp Wave Ripples in a Mouse Model of Familial Alzheimer's Disease. J. Neurosci. *40*, 5116–5136. https://doi.org/10.1523/JNEUROSCI.0425-20.2020.
75. Park, K., Lee, J., Jang, H.J., Richards, B.A., Kohl, M.M., and Kwag, J. (2020). Optogenetic activation of parvalbumin and somatostatin interneurons selectively restores theta-nested gamma oscillations and oscillation-induced spike timing-dependent long-term potentiation impaired by amyloid β oligomers. BMC Biol. *18*, 7. https://doi.org/10.1186/s12915-019-0732-7.
76. Sauer, J.-F., Strüber, M., and Bartos, M. (2015). Impaired fast-spiking interneuron function in a genetic mouse model of depression. Elife *4*, e04979. https://doi.org/10.7554/eLife.04979.
77. Perova, Z., Delevich, K., and Li, B. (2015). Depression of Excitatory Synapses onto Parvalbumin Interneurons in the Medial Prefrontal Cortex in Susceptibility to Stress. J. Neurosci. *35*, 3201–3206. https://doi.org/10.1523/JNEUROSCI.2670-14.2015.
78. Mao, W., Watanabe, T., Cho, S., Frost, J.L., Truong, T., Zhao, X., and Futai, K. (2015). Shank1 regulates excitatory synaptic transmission in mouse hippocampal Parvalbumin-expressing inhibitory interneurons. Eur. J. Neurosci. *41*, 1025–1035. https://doi.org/10.1111/ejn.12877.
79. Roberts, E. (1972). Prospects for research on schizophrenia. An hypotheses suggesting that there is a defect in the GABA system in schizophrenia. Neurosci. Res. Program Bull. *10*, 468–482.
80. Lewis, D.A., and Moghaddam, B. (2006). Cognitive Dysfunction in Schizophrenia: Convergence of γ-Aminobutyric Acid and Glutamate Alterations. Arch. Neurol. *63*, 1372–1376. https://doi.org/10.1001/archneur.63.10.1372.
81. Kehrer, C., Maziashvili, N., Dugladze, T., and Gloveli, T. (2008). Altered excitatory-inhibitory balance in the NMDA-hypofunction model of schizophrenia. Front. Mol. Neurosci. *1*, 6.
82. Nakazawa, K., and Sapkota, K. (2020). The origin of NMDA receptor hypofunction in schizophrenia. Pharmacol. Ther. *205*, 107426. https://doi.org/10.1016/j.pharmthera.2019.107426.
83. Olney, J.W., and Farber, N.B. (1995). Glutamate Receptor Dysfunction and Schizophrenia. Arch. Gen. Psychiatry *52*, 998–1007. https://doi.org/10.1001/archpsyc.1995.03950240016004.
84. Cruz-Martín, A., and Schweizer, F.E. (2008). Imbalance between excitation and inhibition among synaptic connections of CA3 pyramidal neurons in cultured hippocampal slices. Eur. J. Neurosci. *27*, 1353–1363. https://doi.org/10.1111/j.1460-9568.2008.06106.x.
85. Gomez-Arboledas, A., Acharya, M.M., and Tenner, A.J. (2021). The Role of Complement in Synaptic Pruning and Neurodegeneration. ImmunoTargets Ther. *10*, 373–386. https://doi.org/10.2147/ITT.S305420.
86. Druart, M., and Le Magueresse, C. (2019). Emerging Roles of Complement in Psychiatric Disorders. Front. Psychiatry *10*, 573.
87. Hammond, T.R., Robinton, D., and Stevens, B. (2018). Microglia and the Brain: Complementary Partners in Development and Disease. Annu. Rev. Cell Dev. Biol. *34*, 523–544. https://doi.org/10.1146/annurev-cellbio-100616-060509.
88. Stevens, B., Allen, N.J., Vazquez, L.E., Howell, G.R., Christopherson, K.S., Nouri, N., Micheva, K.D., Mehalow, A.K., Huberman, A.D., Stafford, B., et al. (2007). The Classical Complement Cascade Mediates CNS Synapse Elimination. Cell *131*, 1164–1178. https://doi.org/10.1016/j.cell.2007.10.036.
89. Dejanovic, B., Wu, T., Tsai, M.-C., Graykowski, D., Gandham, V.D., Rose, C.M., Bakalarski, C.E., Ngu, H., Wang, Y., Pandey, S., et al. (2022). Complement C1q-dependent excitatory and inhibitory synapse elimination by astrocytes and microglia in Alzheimer's disease mouse models. Nat. Aging *2*, 837–850. https://doi.org/10.1038/s43587-022-00281-1.
90. Schafer, D.P., Lehrman, E.K., Kautzman, A.G., Koyama, R., Mardinly, A.R., Yamasaki, R., Ransohoff, R.M., Greenberg, M.E., Barres, B.A., and Stevens, B. (2012). Microglia Sculpt Postnatal Neural Circuits in an Activity and Complement-Dependent Manner. Neuron *74*, 691–705. https://doi.org/10.1016/j.neuron.2012.03.026.
91. Liddelow, S.A., Guttenplan, K.A., Clarke, L.E., Bennett, F.C., Bohlen, C.J., Schirmer, L., Bennett, M.L., Münch, A.E., Chung, W.-S., Peterson, T.C., et al. (2017). Neurotoxic reactive astrocytes are induced by activated microglia. Nature *541*, 481–487. https://doi.org/10.1038/nature21029.
92. Lian, H., Yang, L., Cole, A., Sun, L., Chiang, A.C.-A., Fowler, S.W., Shim, D.J., Rodriguez-Rivera, J., Taglialatela, G., Jankowsky, J.L., et al. (2015). NFκB-Activated Astroglial Release of Complement C3 Compromises Neuronal Morphology and Function Associated with Alzheimer's Disease. Neuron *85*, 101–115. https://doi.org/10.1016/j.neuron.2014.11.018.
93. Lee, J.D., Kamaruzaman, N.A., Fung, J.N.T., Taylor, S.M., Turner, B.J., Atkin, J.D., Woodruff, T.M., and Noakes, P.G. (2013). Dysregulation of the complement cascade in the hSOD1G93A transgenic mouse model of amyotrophic lateral sclerosis. J. Neuroinflammation *10*, 119. https://doi.org/10.1186/1742-2094-10-119.
94. Zhou, J., Wade, S.D., Graykowski, D., Xiao, M.-F., Zhao, B., Giannini, L.A.A., Hanson, J.E., van Swieten, J.C., Sheng, M., Worley, P.F., and Dejanovic, B. (2023). The neuronal pentraxin Nptx2 regulates complement activity and restrains microglia-mediated synapse loss in neurodegeneration. Sci. Transl. Med. *15*, eadf0141. https://doi.org/10.1126/scitranslmed.adf0141.
95. Phadke, R.A., Kruzich, E., Fournier, L.A., Brack, A., Sha, M., Picard, I., Johnson, C., Stroumbakis, D., Salgado, M., Yeung, C., et al. (2023). C4 induces pathological synaptic loss by impairing AMPAR trafficking. Preprint at bioRxiv. https://doi.org/10.1101/2023.09.09.556388.
96. Kruzich, E., Phadke, R.A., Brack, A., Stroumbakis, D., Infante, O., and Cruz-Martín, A. (2023). A pipeline for STED super-resolution imaging and Imaris analysis of nanoscale synapse organization in mouse cortical brain slices. STAR Protoc. *4*, 102707. https://doi.org/10.1016/j.xpro.2023.102707.

97. Kessler, R.C., Berglund, P., Demler, O., Jin, R., Merikangas, K.R., and Walters, E.E. (2005). Lifetime Prevalence and Age-of-Onset Distributions of DSM-IV Disorders in the National Comorbidity Survey Replication. Arch. Gen. Psychiatry *62*, 593–602. https://doi.org/10.1001/archpsyc.62.6.593.
98. Calhoon, G.G., and Tye, K.M. (2015). Resolving the neural circuits of anxiety. Nat. Neurosci. *18*, 1394–1404. https://doi.org/10.1038/nn.4101.
99. Bandelow, B., Michaelis, S., and Wedekind, D. (2017). Treatment of anxiety disorders. Dialogues Clin. Neurosci 19, 93–107.
100. Arnsten, A.F.T. (2009). Stress signalling pathways that impair prefrontal cortex structure and function. Nat. Rev. Neurosci. *10*, 410–422. https://doi.org/10.1038/nrn2648.
101. Duffney, L.J., Zhong, P., Wei, J., Matas, E., Cheng, J., Qin, L., Ma, K., Dietz, D.M., Kajiwara, Y., Buxbaum, J.D., and Yan, Z. (2015). Autism-like Deficits in Shank3-Deficient Mice Are Rescued by Targeting Actin Regulators. Cell Rep. *11*, 1400–1413. https://doi.org/10.1016/j.celrep.2015.04.064.
102. Sceniak, M.P., Lang, M., Enomoto, A.C., James Howell, C., Hermes, D.J., and Katz, D.M. (2016). Mechanisms of Functional Hypoconnectivity in the Medial Prefrontal Cortex of Mecp2 Null Mice. Cereb. Cortex *26*, 1938–1956. https://doi.org/10.1093/cercor/bhv002.
103. Johnson, C., Kretsge, L.N., Yen, W.W., Sriram, B., O'Connor, A., Liu, R.S., Jimenez, J.C., Phadke, R.A., Wingfield, K.K., Yeung, C., et al. (2022). Highly unstable heterogeneous representations in VIP interneurons of the anterior cingulate cortex. Mol. Psychiatry *27*, 2602–2618. https://doi.org/10.1038/s41380-022-01485-y.
104. Lee, A.T., Cunniff, M.M., See, J.Z., Wilke, S.A., Luongo, F.J., Ellwood, I.T., Ponnavolu, S., and Sohal, V.S. (2019). VIP Interneurons Contribute to Avoidance Behavior by Regulating Information Flow across Hippocampal-Prefrontal Networks. Neuron *102*, 1223–1234.e4. https://doi.org/10.1016/j.neuron.2019.04.001.
105. Courtin, J., Chaudun, F., Rozeske, R.R., Karalis, N., Gonzalez-Campo, C., Wurtz, H., Abdi, A., Baufreton, J., Bienvenu, T.C.M., and Herry, C. (2014). Prefrontal parvalbumin interneurons shape neuronal activity to drive fear expression. Nature *505*, 92–96. https://doi.org/10.1038/nature12755.
106. Bicks, L.K., Koike, H., Akbarian, S., and Morishita, H. (2015). Prefrontal Cortex and Social Cognition in Mouse and Man. Front. Psychol. 6, 1805.
107. Forbes, C.E., and Grafman, J. (2010). The role of the human prefrontal cortex in social cognition and moral judgment. Annu. Rev. Neurosci. *33*, 299–324. https://doi.org/10.1146/annurev-neuro-060909-153230.
108. Bicks, L.K., Yamamuro, K., Flanigan, M.E., Kim, J.M., Kato, D., Lucas, E.K., Koike, H., Peng, M.S., Brady, D.M., Chandrasekaran, S., et al. (2020). Prefrontal parvalbumin interneurons require juvenile social experience to establish adult social behavior. Nat. Commun. *11*, 1003. https://doi.org/10.1038/s41467-020-14740-z.
109. Bennett, F.C., and Molofsky, A.V. (2019). The immune system and psychiatric disease: a basic science perspective. Clin. Exp. Immunol. *197*, 294–307. https://doi.org/10.1111/cei.13334.
110. Hodes, G.E., Kana, V., Menard, C., Merad, M., and Russo, S.J. (2015). Neuroimmune mechanisms of depression. Nat. Neurosci. *18*, 1386–1393. https://doi.org/10.1038/nn.4113.
111. Miller, A.H., and Raison, C.L. (2016). The role of inflammation in depression: from evolutionary imperative to modern treatment target. Nat. Rev. Immunol. *16*, 22–34. https://doi.org/10.1038/nri.2015.5.
112. Estes, M.L., and McAllister, A.K. (2015). Immune mediators in the brain and peripheral tissues in autism spectrum disorder. Nat. Rev. Neurosci. *16*, 469–486. https://doi.org/10.1038/nrn3978.
113. Hou, R., and Baldwin, D.S. (2012). A neuroimmunological perspective on anxiety disorders. Hum. Psychopharmacol. *27*, 6–14. https://doi.org/10.1002/hup.1259.
114. Aw, E., Zhang, Y., Yalcin, E., Herrmann, U.S., and Carroll, M.C. (2021). Chapter Two - Neuropsychiatric disorders: An immunological perspective. In Advances in Immunology, F.W. Alt and K.M. Murphy, eds. (Academic Press), pp. 83–155. https://doi.org/10.1016/bs.ai.2021.09.002.
115. Steen, V.M., Nepal, C., Ersland, K.M., Holdhus, R., Nævdal, M., Ratvik, S.M., Skrede, S., and Håvik, B. (2013). Neuropsychological Deficits in Mice Depleted of the Schizophrenia Susceptibility Gene CSMD1. PLoS One *8*, e79501. https://doi.org/10.1371/journal.pone.0079501.
116. Crider, A., Feng, T., Pandya, C.D., Davis, T., Nair, A., Ahmed, A.O., Baban, B., Turecki, G., and Pillai, A. (2018). Complement component 3a receptor deficiency attenuates chronic stress-induced monocyte infiltration and depressive-like behavior. Brain Behav. Immun. *70*, 246–256. https://doi.org/10.1016/j.bbi.2018.03.004.
117. McLean, C.P., Asnaani, A., Litz, B.T., and Hofmann, S.G. (2011). Gender Differences in Anxiety Disorders: Prevalence, Course of Illness, Comorbidity and Burden of Illness. J. Psychiatr. Res. *45*, 1027–1035. https://doi.org/10.1016/j.jpsychires.2011.03.006.
118. Bahrami, F., and Yousefi, N. (2011). Females Are More Anxious Than Males: a Metacognitive Perspective. Iran. J. Psychiatry Behav. Sci. 5, 83–90.
119. Remes, O., Brayne, C., van der Linde, R., and Lafortune, L. (2016). A systematic review of reviews on the prevalence of anxiety disorders in adult populations. Brain Behav. *6*, e00497. https://doi.org/10.1002/brb3.497.
120. Aleman, A., Kahn, R.S., and Selten, J.-P. (2003). Sex Differences in the Risk of Schizophrenia: Evidence From Meta-analysis. Arch. Gen. Psychiatry *60*, 565–571. https://doi.org/10.1001/archpsyc.60.6.565.
121. McGrath, J., Saha, S., Welham, J., El Saadi, O., MacCauley, C., and Chant, D. (2004). A systematic review of the incidence of schizophrenia: the distribution of rates and the influence of sex, urbanicity, migrant status and methodology. BMC Med. *2*, 13. https://doi.org/10.1186/1741-7015-2-13.
122. Li, X., Zhou, W., and Yi, Z. (2022). A glimpse of gender differences in schizophrenia. Gen. Psychiatr. *35*, e100823. https://doi.org/10.1136/gpsych-2022-100823.
123. Giordano, G.M., Bucci, P., Mucci, A., Pezzella, P., and Galderisi, S. (2021). Gender Differences in Clinical and Psychosocial Features Among Persons With Schizophrenia: A Mini Review. Front. Psychiatry *12*, 789179.
124. Ayesa-Arriola, R., de la Foz, V.O.-G., Setién-Suero, E., Ramírez-Bonilla, M.L., Suárez-Pinilla, P., Son, J.M., Vázquez-Bourgon, J., Juncal-Ruiz, M., Gómez-Revuelta, M., Tordesillas-Gutiérrez, D., et al. (2020). Understanding sex differences in long-term outcomes after a first episode of psychosis. Npj Schizophr *6*, 1–8. https://doi.org/10.1038/s41537-020-00120-5.
125. Gogos, A., Sbisa, A.M., Sun, J., Gibbons, A., Udawela, M., and Dean, B. (2015). A Role for Estrogen in Schizophrenia: Clinical and Preclinical Findings. Int. J. Endocrinol. *2015*, 615356. https://doi.org/10.1155/2015/615356.
126. Kamitaki, N., Sekar, A., Handsaker, R.E., de Rivera, H., Tooley, K., Morris, D.L., Taylor, K.E., Whelan, C.W., Tombleson, P., Loohuis, L.M.O., et al. (2020). Complement genes contribute sex-biased vulnerability in diverse disorders. Nature *582*, 577–581. https://doi.org/10.1038/s41586-020-2277-x.
127. Wu, Y.C., Du, X., van den Buuse, M., and Hill, R.A. (2014). Sex differences in the adolescent developmental trajectory of parvalbumin interneurons in the hippocampus: A role for estradiol. Psychoneuroendocrinology *45*, 167–178. https://doi.org/10.1016/j.psyneuen.2014.03.016.
128. Searles, R.V., Yoo, M.-J., He, J.-R., Shen, W.B., and Selmanoff, M. (2000). Sex differences in GABA turnover and glutamic acid decarboxylase (GAD65 and GAD67) mRNA in the rat hypothalamus. Brain Res. *878*, 11–19. https://doi.org/10.1016/S0006-8993(00)02648-2.
129. Hensch, T.K., and Bilimoria, P.M. (2012). Re-opening Windows: Manipulating Critical Periods for Brain Development. Cerebrum *2012*, 11.
130. Hensch, T.K. (2014). Bistable Parvalbumin Circuits Pivotal for Brain Plasticity. Cell *156*, 17–19. https://doi.org/10.1016/j.cell.2013.12.034.
131. Donato, F., Rompani, S.B., and Caroni, P. (2013). Parvalbumin-expressing basket-cell network plasticity induced by experience regulates adult learning. Nature *504*, 272–276. https://doi.org/10.1038/nature12866.
132. Aronitz, E.M., Kamermans, B.A., and Duffy, K.R. (2021). Development of parvalbumin neurons and perineuronal nets in the visual cortex of normal and dark-exposed cats. J. Comp. Neurol. *529*, 2827–2841. https://doi.org/10.1002/cne.25127.
133. Dachtler, J., and Fox, K. (2017). Do cortical plasticity mechanisms differ between males and females? J. Neurosci. Res. *95*, 518–526. https://doi.org/10.1002/jnr.23850.
134. Lynch, M.A. (2022). Exploring Sex-Related Differences in Microglia May Be a Game-Changer in Precision Medicine. Front. Aging Neurosci. *14*, 868448.
135. Guneykaya, D., Ivanov, A., Hernandez, D.P., Haage, V., Wojtas, B., Meyer, N., Maricos, M., Jordan, P., Buonfiglioli, A., Gielniewski, B., et al. (2018). Transcriptional and Translational Differences of Microglia from Male and Female Brains. Cell Rep. *24*, 2773–2783.e6. https://doi.org/10.1016/j.celrep.2018.08.001.
136. Parkhurst, C.N., Yang, G., Ninan, I., Savas, J.N., Yates, J.R., Lafaille, J.J., Hempstead, B.L., Littman, D.R., and Gan, W.-B. (2013).

Microglia promote learning-dependent synapse formation through BDNF. Cell *155*, 1596–1609. https://doi.org/10.1016/j.cell.2013.11.030.

137. Hayley, S., Du, L., Litteljohn, D., Palkovits, M., Faludi, G., Merali, Z., Poulter, M.O., and Anisman, H. (2015). Gender and brain regions specific differences in brain derived neurotrophic factor protein levels of depressed individuals who died through suicide. Neurosci. Lett. *600*, 12–16. https://doi.org/10.1016/j.neulet.2015.05.052.
138. Hill, R.A., and van den Buuse, M. (2011). Sex-dependent and region-specific changes in TrkB signaling in BDNF heterozygous mice. Brain Res. *1384*, 51–60. https://doi.org/10.1016/j.brainres.2011.01.060.
139. Lim, S.-H., Park, E., You, B., Jung, Y., Park, A.-R., Park, S.G., and Lee, J.-R. (2013). Neuronal Synapse Formation Induced by Microglia and Interleukin 10. PLoS One *8*, e81218. https://doi.org/10.1371/journal.pone.0081218.
140. Miyamoto, A., Wake, H., Ishikawa, A.W., Eto, K., Shibata, K., Murakoshi, H., Koizumi, S., Moorhouse, A.J., Yoshimura, Y., and Nabekura, J. (2016). Microglia contact induces synapse formation in developing somatosensory cortex. Nat. Commun. *7*, 12540. https://doi.org/10.1038/ncomms12540.
141. Cruz-Martín, A., Crespo, M., and Portera-Cailliau, C. (2010). Delayed Stabilization of Dendritic Spines in Fragile X Mice. J. Neurosci. *30*, 7793–7803. https://doi.org/10.1523/JNEUROSCI.0577-10.2010.
142. Mao, Y.-T., Zhu, J.X., Hanamura, K., Iurilli, G., Datta, S.R., and Dalva, M.B. (2018). Filopodia Conduct Target Selection in Cortical Neurons Using Differences in Signal Kinetics of a Single Kinase. Neuron *98*, 767–782.e8. https://doi.org/10.1016/j.neuron.2018.04.011.
143. Pchitskaya, E., and Bezprozvanny, I. (2020). Dendritic Spines Shape Analysis—Classification or Clusterization? Perspective. Front. Synaptic Neurosci. *12*, 31. https://doi.org/10.3389/fnsyn.2020.00031.
144. Selemon, L.D. (2013). A role for synaptic plasticity in the adolescent development of executive function. Transl. Psychiatry *3*, e238. https://doi.org/10.1038/tp.2013.7.
145. Chaudhury, S., Sharma, V., Kumar, V., Nag, T.C., and Wadhwa, S. (2016). Activity-dependent synaptic plasticity modulates the critical phase of brain development. Brain Dev. *38*, 355–363. https://doi.org/10.1016/j.braindev.2015.10.008.
146. Kourosh-Arami, M., Hosseini, N., and Komaki, A. (2021). Brain is modulated by neuronal plasticity during postnatal development. J. Physiol. Sci. *71*, 34. https://doi.org/10.1186/s12576-021-00819-9.
147. Citri, A., and Malenka, R.C. (2008). Synaptic Plasticity: Multiple Forms, Functions, and Mechanisms. Neuropsychopharmacology *33*, 18–41. https://doi.org/10.1038/sj.npp.1301559.
148. Zick, J.L., Crowe, D.A., Blackman, R.K., Schultz, K., Bergstrand, D.W., DeNicola, A.L., Carter, R.E., Ebner, T.J., Lanier, L.M., Netoff, T.I., and Chafee, M.V. (2022). Disparate insults relevant to schizophrenia converge on impaired spike synchrony and weaker synaptic interactions in prefrontal local circuits. Curr. Biol. *32*, 14–25.e4. https://doi.org/10.1016/j.cub.2021.10.009.
149. Zick, J.L., Blackman, R.K., Crowe, D.A., Amirikian, B., DeNicola, A.L., Netoff, T.I., and Chafee, M.V. (2018). Blocking NMDAR Disrupts Spike Timing and Decouples Monkey Prefrontal Circuits: Implications for Activity-Dependent Disconnection in Schizophrenia. Neuron *98*, 1243–1255.e5. https://doi.org/10.1016/j.neuron.2018.05.010.
150. Crowe, D.A., Willow, A., Blackman, R.K., DeNicola, A.L., Chafee, M.V., and Amirikian, B. (2024). A prefrontal network model operating near steady and oscillatory states links spike desynchronization and synaptic deficits in schizophrenia. Elife *13*, e79352. https://doi.org/10.7554/eLife.79352.
151. Daskalakis, Z.J., Christensen, B.K., Fitzgerald, P.B., and Chen, R. (2008). Dysfunctional Neural Plasticity in Patients With Schizophrenia. Arch. Gen. Psychiatry *65*, 378–385. https://doi.org/10.1001/archpsyc.65.4.378.
152. Papaleo, F., Yang, F., Paterson, C., Palumbo, S., Carr, G.V., Wang, Y., Floyd, K., Huang, W., Thomas, C.J., Chen, J., et al. (2016). Behavioral, Neurophysiological, and Synaptic Impairment in a Transgenic Neuregulin1 (NRG1-IV) Murine Schizophrenia Model. J. Neurosci. *36*, 4859–4875. https://doi.org/10.1523/JNEUROSCI.4632-15.2016.
153. Crabtree, G.W., Sun, Z., Kvajo, M., Broek, J.A.C., Fénelon, K., McKellar, H., Xiao, L., Xu, B., Bahn, S., O'Donnell, J.M., and Gogos, J.A. (2017). Alteration of Neuronal Excitability and Short-Term Synaptic Plasticity in the Prefrontal Cortex of a Mouse Model of Mental Illness. J. Neurosci. *37*, 4158–4180. https://doi.org/10.1523/JNEUROSCI.4345-15.2017.
154. Kvajo, M., McKellar, H., Drew, L.J., Lepagnol-Bestel, A.-M., Xiao, L., Levy, R.J., Blazeski, R., Arguello, P.A., Lacefield, C.O., Mason, C.A., et al. (2011). Altered axonal targeting and short-term plasticity in the hippocampus of Disc1 mutant mice. Proc. Natl. Acad. Sci. USA *108*, E1349–E1358. https://doi.org/10.1073/pnas.1114113108.
155. Tang, T.T.-T., Yang, F., Chen, B.-S., Lu, Y., Ji, Y., Roche, K.W., and Lu, B. (2009). Dysbindin regulates hippocampal LTP by controlling NMDA receptor surface expression. Proc. Natl. Acad. Sci. USA *106*, 21395–21400. https://doi.org/10.1073/pnas.0910499106.
156. Nakazawa, K., Jeevakumar, V., and Nakao, K. (2017). Spatial and temporal boundaries of NMDA receptor hypofunction leading to schizophrenia. NPJ Schizophr. *3*, 7. https://doi.org/10.1038/s41537-016-0003-3.
157. Murray, J.D., Anticevic, A., Gancsos, M., Ichinose, M., Corlett, P.R., Krystal, J.H., and Wang, X.-J. (2014). Linking Microcircuit Dysfunction to Cognitive Impairment: Effects of Disinhibition Associated with Schizophrenia in a Cortical Working Memory Model. Cereb. Cortex *24*, 859–872. https://doi.org/10.1093/cercor/bhs370.
158. Babaev, O., Piletti Chatain, C., and Krueger-Burg, D. (2018). Inhibition in the amygdala anxiety circuitry. Exp. Mol. Med. *50*, 1–16. https://doi.org/10.1038/s12276-018-0063-8.
159. Krabbe, S., Gründemann, J., and Lüthi, A. (2018). Amygdala Inhibitory Circuits Regulate Associative Fear Conditioning. Biol. Psychiatry *83*, 800–809. https://doi.org/10.1016/j.biopsych.2017.10.006.
160. Schneider, C.A., Rasband, W.S., and Eliceiri, K.W. (2012). NIH Image to ImageJ: 25 years of image analysis. Nat. Methods *9*, 671–675. https://doi.org/10.1038/nmeth.2089.
161. Stirling, D.R., Swain-Bowden, M.J., Lucas, A.M., Carpenter, A.E., Cimini, B.A., and Goodman, A. (2021). CellProfiler 4: improvements in speed, utility and usability. BMC Bioinf. *22*, 433. https://doi.org/10.1186/s12859-021-04344-9.
162. Phadke, R.A., Wetzel, A.M., Fournier, L.A., Sha, M., Padró-Luna, N.M., and Cruz-Martín, A. (2023). REVEALS: An Open Source Multi Camera GUI For Rodent Behavior Acquisition. Preprint at bioRxiv. https://doi.org/10.1101/2023.08.22.554365.
163. Ito, S., Hansen, M.E., Heiland, R., Lumsdaine, A., Litke, A.M., and Beggs, J.M. (2011). Extending Transfer Entropy Improves Identification of Effective Connectivity in a Spiking Cortical Network Model. PLoS One *6*, e27431. https://doi.org/10.1371/journal.pone.0027431.
164. Soriano, P. (1999). Generalized lacZ expression with the ROSA26 Cre reporter strain. Nat. Genet. *21*, 70–71. https://doi.org/10.1038/5007.
165. McQuin, C., Goodman, A., Chernyshev, V., Kamentsky, L., Cimini, B.A., Karhohs, K.W., Doan, M., Ding, L., Rafelski, S.M., Thirstrup, D., et al. (2018). CellProfiler 3.0: Next-generation image processing for biology. PLoS Biol. *16*, e2005970. https://doi.org/10.1371/journal.pbio.2005970.
166. Reference Atlas: Allen Brain Atlas: Mouse Brain https://mouse.brain-map.org/static/atlas.
167. Paxinos, G., and Franklin, B.J. (2012). Paxinos and Franklin's the Mouse Brain in Stereotaxic Coordinates, 4th ed. (Academic Press).
168. Data Acquisition Software - UCLA Miniscope http://miniscope.org/index.php/Data_Acquisition_Software.
169. Mathis, A., Mamidanna, P., Cury, K.M., Abe, T., Murthy, V.N., Mathis, M.W., and Bethge, M. (2018). DeepLabCut: markerless pose estimation of user-defined body parts with deep learning. Nat. Neurosci. *21*, 1281–1289. https://doi.org/10.1038/s41593-018-0209-y.
170. Fuhrmann, G., Markram, H., and Tsodyks, M. (2002). Spike frequency adaptation and neocortical rhythms. J. Neurophysiol. *88*, 761–770. https://doi.org/10.1152/jn.2002.88.2.761.
171. Doischer, D., Hosp, J.A., Yanagawa, Y., Obata, K., Jonas, P., Vida, I., and Bartos, M. (2008). Postnatal Differentiation of Basket Cells from Slow to Fast Signaling Devices. J. Neurosci. *28*, 12956–12968. https://doi.org/10.1523/JNEUROSCI.2890-08.2008.
172. Okaty, B.W., Miller, M.N., Sugino, K., Hempel, C.M., and Nelson, S.B. (2009). Transcriptional and Electrophysiological Maturation of Neocortical Fast-Spiking GABAergic Interneurons. J. Neurosci. *29*, 7040–7052. https://doi.org/10.1523/JNEUROSCI.0105-09.2009.
173. Fanselow, E.E., and Connors, B.W. (2010). The Roles of Somatostatin-Expressing (GIN) and Fast-Spiking Inhibitory Interneurons in up-down States of Mouse Neocortex. J. Neurophysiol. *104*, 596–606. https://doi.org/10.1152/jn.00206.2010.
174. Dayan, P., and Abbott, L.F. (2001). Theoretical Neuroscience: Computational and Mathematical Modeling of Neural Systems (Massachusetts Institute of Technology Press).
175. Liu, L., Xu, H., Wang, J., Li, J., Tian, Y., Zheng, J., He, M., Xu, T.-L., Wu, Z.-Y., Li, X.-M., et al. (2020). Cell type–differential modulation of

prefrontal cortical GABAergic interneurons on low gamma rhythm and social interaction. Sci. Adv. *6*, eaay4073. https://doi.org/10.1126/sciadv.aay4073.

176. Wang, T., Yan, R., Zhang, X., Wang, Z., Duan, H., Wang, Z., and Zhou, Q. (2023). Paraventricular Thalamus Dynamically Modulates Aversive Memory via Tuning Prefrontal Inhibitory Circuitry. J. Neurosci. *43*, 3630–3646. https://doi.org/10.1523/JNEUROSCI.1028-22.2023.
177. Kee, T., Sanda, P., Gupta, N., Stopfer, M., and Bazhenov, M. (2015). Feed-Forward versus Feedback Inhibition in a Basic Olfactory Circuit. PLoS Comput. Biol. *11*, e1004531. https://doi.org/10.1371/journal.pcbi.1004531.
178. Ly, C., and Doiron, B. (2017). Noise-enhanced coding in phasic neuron spike trains. PLoS One *12*, e0176963. https://doi.org/10.1371/journal.pone.0176963.
179. Magee, J.C. (2001). Dendritic Mechanisms of Phase Precession in Hippocampal CA1 Pyramidal Neurons. J. Neurophysiol. *86*, 528–532. https://doi.org/10.1152/jn.2001.86.1.528.
180. Blundon, J.A., Bayazitov, I.T., and Zakharenko, S.S. (2011). Presynaptic Gating of Postsynaptically Expressed Plasticity at Mature Thalamocortical Synapses. J. Neurosci. *31*, 16012–16025. https://doi.org/10.1523/JNEUROSCI.3281-11.2011.
181. Elhilali, M., Fritz, J.B., Klein, D.J., Simon, J.Z., and Shamma, S.A. (2004). Dynamics of Precise Spike Timing in Primary Auditory Cortex. J. Neurosci. *24*, 1159–1172. https://doi.org/10.1523/JNEUROSCI.3825-03.2004.
182. Lu, T., Liang, L., and Wang, X. (2001). Temporal and rate representations of time-varying signals in the auditory cortex of awake primates. Nat. Neurosci. *4*, 1131–1138. https://doi.org/10.1038/nn737.
183. Nocon, J.C., Gritton, H., Han, X., and Sen, K. (2022). Differential Inhibitory Responses to Temporal Features Enhance Cortical Coding of Dynamic Stimuli: A Network Model. Preprint at bioRxiv. https://doi.org/10.1101/2022.09.22.509092.
184. Seay, M.J., Natan, R.G., Geffen, M.N., and Buonomano, D.V. (2020). Differential Short-Term Plasticity of PV and SST Neurons Accounts for Adaptation and Facilitation of Cortical Neurons to Auditory Tones. J. Neurosci. *40*, 9224–9235. https://doi.org/10.1523/JNEUROSCI.0686-20.2020.
185. Moore, A.K., Weible, A.P., Balmer, T.S., Trussell, L.O., and Wehr, M. (2018). Rapid Rebalancing of Excitation and Inhibition by Cortical Circuitry. Neuron *97*, 1341–1355.e6. https://doi.org/10.1016/j.neuron.2018.01.045.
186. Toader, O., von Heimendahl, M., Schuelert, N., Nissen, W., and Rosenbrock, H. (2020). Suppression of Parvalbumin Interneuron Activity in the Prefrontal Cortex Recapitulates Features of Impaired Excitatory/Inhibitory Balance and Sensory Processing in Schizophrenia. Schizophr. Bull. *46*, 981–989. https://doi.org/10.1093/schbul/sbz123.
187. Agetsuma, M., Hamm, J.P., Tao, K., Fujisawa, S., and Yuste, R. (2018). Parvalbumin-Positive Interneurons Regulate Neuronal Ensembles in Visual Cortex. Cereb. Cortex *28*, 1831–1845. https://doi.org/10.1093/cercor/bhx169.
188. Schreiber, T. (2000). Measuring Information Transfer. Phys. Rev. Lett. *85*, 461–464. https://doi.org/10.1103/PhysRevLett.85.461.

STAR★METHODS

KEY RESOURCES TABLE

REAGENT or RESOURCE	SOURCE	IDENTIFIER
Antibodies		
Rabbit polyclonal anti parvalbumin	Abcam	Cat#ab11427
Mouse monoclonal anti PSD95	Novus	Cat#NB300-556
Guinea pig polyclonal anti bassoon	Synaptic Systems	Cat#141004
Anti-rabbit 488	Jackson	Cat#111-545-144
Anti-mouse STAR ORANGE	Abberior	Cat#STORANGE
Anti-rabbit STAR RED	Abberior	Cat#STRED
Anti-guinea pig STAR RED	Abberior	Cat#STRED
Bacterial and virus strains		
pAAV-FLEX-tdTomato	Gift from Edward Boyden	Addgene AAV1; Cat#28306; RRID:Addgene_28306
pAAV-S5E2-dTom-nlsdTom	Gift from Jordane Dimidschstein	Addgene AAV9; Cat #135630; RRID:Addgene_135630
Chemicals, peptides, and recombinant proteins		
Tetrodotoxin	Tocris	Cat#1069
Picrotoxin	HelloBio	Cat#HB0506
6-Cyano-7-nitroquinoxaline-2,3-dione disodium (CNQX)	Tocris	Cat#1045
DL-2-Amino-5-phosphonopentanoic acid (DL-AP5)	Tocris	Cat#0105
RNAscope fluorescent probe for Mm-C4b	Advanced Cell Diagnostics	Cat#445161
RNAscope fluorescent probe for Mm-Pvalb	Advanced Cell Diagnostics	Cat#421931
RNAscope fluorescent probe for Mm-SST	Advanced Cell Diagnostics	Cat#404631
RNAscope fluorescent probe for Mm-Rbfox3	Advanced Cell Diagnostics	Cat#313311
RNAscope DAPI	Advanced Cell Diagnostics	Cat#320858
ProLong Diamond Antifade Mountant	ThermoFisher	Cat#P36961
Phosphate-buffered saline 10×	Gibco	Cat#70011044
Triton X-100	Sigma-Aldrich	Cat#9036-19-5
DAPI Fluoromount	ThermoFisher	Cat#00-4959-52
Optimal Cutting Temperature (O.C.T.)	Tissue-Tek	Cat#4583
Critical commercial assays		
RNAscope Multiplex Fluorescent v1	Advanced Cell Diagnostics	Cat#320850
RNAscope Multiplex Fluorescent v2	Advanced Cell Diagnostics	Cat#323100
Deposited data		
Raw data	This paper	https://osf.io/je38k/
Experimental models: Organisms/strains		
Mouse: CD-1	Charles River Laboratories	Cat#022; RRID:IMSR_CRL:022
Mouse: mC4-KI	Cyagen/Taconic; This paper	N/A
Mouse: C57BL/6J	The Jackson Laboratory	Cat#000664; RRID:IMSR_JAX:000664
Mouse: B6.129P2-Pvalb$^{tm1(cre)Arbr}$/J	The Jackson Laboratory	Cat#017320; RRID:IMSR_JAX:017320
Mouse: STOCK Tg(Actl6b-Cre)4092Jiwu/J	The Jackson Laboratory	Cat#027826; RRID:IMSR_JAX:027826
Software and algorithms		
NisElements	Nikon Instruments	N/A
ImageJ	Schneider et al.[160]	https://imagej.nih.gov/ij/

(*Continued on next page*)

Continued

REAGENT or RESOURCE	SOURCE	IDENTIFIER
CellProfiler	Stirling et al.[161]	N/A
Imaris	Oxford Instruments	RRID:SCR_007370
MATLAB	MathWorks	RRID: SCR_001622
UCLA Miniscope Data Acquisition Software	UCLA	N/A
REVEALS	Phadke et al.[162]	N/A
Multiclamp 700B	Molecular Devices	Cat#2500-0157
pCLAMP	Molecular Devices	Cat#5060221
Electrophysiology and behavioral analysis routines	This paper	https://github.com/CruzMartinLab
Transfer Entropy MATLAB Toolbox	Ito et al.[163]	N/A
Prism	Graphpad	N/A
Other		
Cryostat	Leica	Cat#CM1800
Fisherbrand Superfrost Plus microscope slides	Fisher Scientific	Cat#1255015
Nikon Eclipse Ti with C2Si+ laser scanning confocal	Nikon Instruments	N/A
Nikon Ti2-E with Yokogawa spinning disk confocal	Nikon Instruments	N/A
Freezing stage sliding microtome	Leica	Cat#SM2000R
Microscope slides	Globe Scientific	Cat#1324
Light meter	Dr. meter	Cat#LX1330B
C922x Pro Stream Webcams	Logitech	Cat#960-001087
Flea3 USB3 camera	Teledyne	Cat#FL3-U3-13E4C-C
Borosilicate pipettes	Sutter Instrument	Cat#BF150-117-10
Nanoject II	Drummond	Cat#3-000-204/205A/206A
Electrophysiology brightfield Lumen 200	Prior Scientific	Cat#L200
Rolera-Bolt CMOS camera	QImaging	Cat#0I-ROL-BOLT-*M*-12
Fixed-stage electrophysiology microscope	Olympus	Cat#BX51WI

EXPERIMENTAL MODEL AND STUDY PARTICIPANT DETAILS

All mice were group-housed (2–4 animals/cage). The light/dark cycle was adjusted depending on the behavioral task (see below). Unless otherwise stated, food and water were provided *ad libitum* to all mice. Experimental offspring were reared in the cage with the dam until weaning at postnatal day (P) 21. Stimulus CD-1 (Charles River Laboratories, strain code: 022, RRID:IMSR_CRL:022) mice 3–5 weeks of age were used in social assays. During experiments and analysis, the experimenter was blinded to mouse genotype and experimental conditions whenever possible.

Generation of the mC4-KI mouse

Generation of the mC4-KI mouse was accomplished using Cyagen/Taconic services (Santa Clara, CA). Briefly, the "adenovirus SA-Frt-CAG promoter-Frt-loxP-3*polyA-loxP-Kozak-mouse C4b CDS-polyA" cassette was cloned into intron 1 of ROSA26. The homology arms were generated by PCR using BAC clones as templates. C57BL/6 ES cells were used for gene targeting. In the targeting vector, the positive selection marker (*Neo*) is flanked by SDA (self-deletion anchor) sites. Diphtheria toxin A (DTA) was used for negative selection. Targeted ES cells were injected into C57BL/6J albino embryos, which were then re-implanted into CD-1 pseudo-pregnant females. Founder animals were identified by their coat color, and their germline transmission was confirmed by breeding with C57BL/6J females and subsequent genotyping of the offspring. Male and female heterozygous targeted mice were generated from clone 1F3 and were bred to establish a colony. Lastly, the constitutive KI cell allele was obtained after Cre-mediated recombination (see breeding section).

Breeding

C57BL/6J (Jackson Laboratory, strain #: 000664, RRID:IMSR_JAX:000664) mice were paired with heterozygous mC4-KI transgenics of the same genetic background. Genotyping (Transnetyx) was used to plan breeding schemes and identify specific genotypes. Heterozygous mC4-KI transgenics were paired with homozygous PV-Cre mice (Jackson Laboratory, B6.129P2-Pvalb$^{tm1(cre)Arbr}$/J, strain #: 017320, RRID:IMSR_JAX:017320). Our breeding scheme generated mice that inherited the floxed mC4-KI allele, and thus overexpress (OE) mC4 in PV cells (PV-mC4-KI, or simply KI), and wild type littermates, which were used as control mice (PV-mC4-WT, or simply WT).

To OE mC4 in all neurons, heterozygous mC4-KI transgenic mice were paired with homozygous BAF53b Pan-neuronal-Cre (Jackson Laboratory, STOCK Tg(Actl6b-Cre)4092Jiwu/J, Strain #:027826, RRID:IMSR_JAX:027826[67]) mice. Breeding these two mouse lines yielded mice that inherited the floxed mC4-KI allele, and thus OE mC4 in all neurons (PanN-mC4-KI), and wild type control littermates (PanN-mC4-WT).

Our breeding scheme ensured that all experimental mice carried the cre recombinase gene to control for its effects. PV-mC4-KI or PanN-mC4-KI mice did not exhibit any gross brain abnormalities, indistinguishable from controls. Additionally, KI mice had weights similar to those of their controls, suggesting that besides the described cellular and behavioral deficits, these mice were otherwise healthy and had no significant defects.

A strength of the mC4-KI transgenic mouse is that more moderate levels of mC4-OE can be driven in a cell-specific manner by crossing the mC4-KI mice to Flp transgenic mice, which substitutes the strong CAG promoter for the weaker ROSA26 promoter,[52,164] allowing the effects of more moderate transgene expression to be studied.

Ethics statement

All experimental protocols were conducted according to the National Institutes of Health (NIH) guidelines for animal research and were approved by the Boston University Institutional Animal Care and Use Committee (IACUC; protocol #2018–539).

METHOD DETAILS

Multiplex fluorescence *in situ* hybridization

Tissue preparation and staining

For multiplex fluorescence *in situ* hybridization (M-FISH) experiments, brains of PV-mC4-WT and PV-mC4-KI mice P21-22 or P58-65, or brains of PanN-mC4-WT and PanN-mC4-KI mice P41-61, were extracted and immediately embedded in O.C.T. (Tissue-Tek, 4583), flash-frozen on dry ice, and stored in −80°C until being cut. Prior to slicing, brains were moved to −20°C for 30 min. Slices were cut on a Leica CM 1800 cryostat at 16 μm at −16 to −19°C and adhered directly onto microscope slides (Fisher Brand Superfrost Plus, #1255015), which were then stored in −80°C until ready for M-FISH (<1 week). M-FISH experiments were then performed as directed by the commercially available kit (RNAScope, Advanced Cell Diagnostics), from which all probes and reagents were purchased. Experiments involving PV-mC4-OE used the Reagent Kit v1 (320850), and experiments involving PanN-mC4-OE used the Reagent Kit v2 (323100) with fluorescent probes for *mC4* (Mm-C4b, 445161), parvalbumin (Mm-Pvalb-C2, 421931-C2), somatostatin (Mm-Sst-C3, 404631-C3), and/or Rbfox3 (Mm-Rbfox3-C3, 313311-C3). To confirm cell bodies in the slice, nuclei were stained with RNAScope DAPI (320858). After staining, the slices were mounted with ProLong Diamond Antifade Mountant (ThermoFisher, P36961). Each round of M-FISH performed contained tissue from both PV-mC4-WT and PV-mC4-KI mice. M-FISH for all PanN-mC4-OE samples was performed together.

Imaging and analysis

M-FISH images were acquired on one of two confocal systems: 1) a Nikon C2+ Si spectral laser scanning microscope (LSM) with Nikon Plan Apo λ 40×, water-immersion objective, and step size 0.4 μm, or 2) a Nikon Ti2-E body with Yokogawa Spinning Disk and Nikon CFI Apo LWD 40×/1.15NA, water immersion objective, and step size 0.3 μm. Only one system was used for a specific experimental condition. For each round of M-FISH, consistent imaging parameters were used. Tissue slices imaged and analyzed belonged to mPFC divisions (prelimbic (PrL), infralimbic (IL), and anterior cingulate (AC) cortices) of the mouse brain. Images predominantly included L2/3, though deeper cortical layers were also included in the region of interest (ROI). For analysis, a maximum intensity projection of each z stack was made (ImageJ,[160] National Institute of Health, Bethesda, Maryland) and transferred into CellProfiler[161,165] (Broad Institute). Cells were identified and segmented using DAPI, and the contour was expanded by 10 pixels (approximately 3.1 μm) to capture the majority of PV, SST, Rbfox3, and mC4 puncta surrounding the nucleus. Cells were classified as PV or SST cells if their expanded contour contained an empirically derived minimum of 13 or 10 PV- or SST-positive puncta, respectively. Cells were classified as Rbfox3-positive if mean Rbfox3 intensity exceeded an empirically derived threshold; Rbfox3-negative cells were classified as such if their Rbfox3 intensity was below this threshold and thus contained zero Rbfox3 puncta. Once identified as a PV, SST, non-PV/non-SST DAPI+ 'Other' cell, Rbfox3-positive, or Rbfox3-negative cell, CellProfiler was used to quantify the number of mC4-positive puncta within each contour (i.e., within each cell).

PV cell density

Perfusion and immunohistochemistry

Mice P55-74 were anesthetized with a 4% isoflurane-oxygen mixture (v/v) and perfused transcardially with phosphate-buffered saline (PBS, Gibco, Life Science Technologies, 70011044) followed by 4% paraformaldehyde (PFA) in PBS. Extracted brains were further fixed in PFA for 24 h before being transferred to a 30% (w/v) sucrose solution and stored at 4°C. Brain slices were cut at 40 μm on a freezing stage sliding microtome (Leica SM2000) and stored in PBS. From each mouse, two brain slices were selected for immunostaining: one at approximately bregma +1.98 mm and another at bregma +0.98 mm along the anterior-posterior (A-P) axis. Slices were first blocked and made permeable in a solution containing 10% donkey serum (Sigma-Aldrich, S30-100ML) and 1% Triton X-100 (Sigma-Aldrich, X100-100ML) in PBS. Next, after applying the primary antibody (rabbit anti-PV, Abcam, ab11427) at a 1:250 dilution, slices were placed on a shaker at 4°C for 48 h. Slices were then washed 4 × 15 min with 0.025% Triton X-100 in PBS. Next, the secondary antibody was applied (anti-rabbit STAR RED, Abberior, STRED) at a 1:500 dilution and returned to the shaker for 48 h at 4°C. Slices were then washed 4 × 15 min in PBS, and mounted onto 1 mm microscope slides (Globe Scientific, #1324) with DAPI Fluoromount (Thermo Fisher Scientific, Cat. #: 00-4959-52).

Imaging and analysis

Cell density imaging was acquired (laser lines 405 and 640 nm) using the LSM listed above at a step size of 1 μm for nearly the entire thickness of the tissue slice (40 μm). For each animal, the mPFC was imaged at 20× in both the slice at bregma +1.98 mm (6 ROIs total, 3/hemisphere, that include the PrL, IL, and AC cortices) and the slice more posterior at bregma +0.98 mm (4 ROIs, 2/hemisphere, all AC). Consistent imaging parameters were maintained across all imaging sessions. Images were analyzed as TIFFs in ImageJ and compared to a brain atlas to identify brain regions.[166,167] The intensity value in the PV channel for each ROI (in a brain slice) and the average background signal for each brain slice were quantified. To binarize cells as PV-positive, we calculated an intensity threshold and classified cells as PV-positive if their intensity value was higher than this threshold. These data were used to calculate the number of PV cells that were positive. To calculate density, we determined the area (excluding L1) of the ROI in which PV cells were counted and calculated the 3D volume (in mm^3) by multiplying the 2D area of each slice by the depth of the tissue imaged (the z stack).

PV cell synaptic puncta

Perfusion and immunohistochemistry

PV-mC4-WT and PV-mC4-KI mice P45-55 were perfused, and their brains were extracted, stored, sliced, and selected for staining as before. The immunohistochemical staining procedure was performed exactly as listed above. Primary antibodies used included rabbit anti-PV (1:500), mouse anti-PSD95 (1:250, Novus, NB300-556), and guinea pig anti-bassoon (1:1000, Synaptic Systems, #141004). Secondary antibodies used included anti-rabbit488 (1:1000, Jackson, 111-545-144), anti-mouse STAR ORANGE (1:300, Abberior, STORANGE), and anti-guinea pig STAR RED (1:1000, Abberior, STRED).

Imaging and Imaris analysis

PV cells and synaptic puncta of L2/3 of the mPFC were acquired (LSM as listed above, laser lines 488, 560, and 640 nm) at a step size of 0.2 μm. For each sex within each condition, 12 PV cells were imaged (4 PV cells per animal, 3 animals per sex per condition). All analyses were performed using the Imaris software.[96] Following correction for Z-stretch and deconvolution of PSD95 and bassoon puncta, PV cells were reconstructed as 'surfaces'. All PSD95 and bassoon puncta in the image were reconstructed as 'spots', and the spots of each were filtered to retain only those that were within 1 μm of the PV cell surface. Of the remaining PSD95 and bassoon spots, colocalization was defined as instances whereby the distance between the centers of any two spots was below 0.8 μm.

Behavior

General experimental conditions

P40-60 mice were used for all behavioral assays, group housed in sets of 2–3 mice per cage. Mice were used in either (1) a series of anxiety-related assays or (2) a series of sociability assays. The specific sequence of anxiety-related assays that mice were exposed to was consistent across all mice and proceeded in the following order: open field (OF) and elevated zero maze (EZM, performed on the same day), light-dark box (LDB), and novelty-suppressed feeding (NSF) (Novel arena and cage NSF, performed back-to-back).

Similarly, the specific sequence of sociability assays that mice were exposed to was also consistent across all mice: Object and juvenile interaction (performed immediately back-to-back for each mouse, see object and social interaction) was followed by the three-chamber sociability assay.

Seven days prior to the first day of handling (see handling below), mice were genotyped (Transnetyx), transferred to a fresh cage, and placed with a *Do Not Handle* card to minimize human handling and stress. Mice were reliably identified using a set of ear hole punches throughout behavioral experiments.

All behavioral assays were performed at a similar time of the day. Mice used in anxiety-related assays were reared on a 12 h light/dark cycle with lights on at 7 a.m. and lights off at 7 p.m., and assays were performed under white light (Adorama, 13″ Dimmable LED Ring Light). The intensity of light used for each assay was consistent each time the assay was performed, but varied depending on the assay (see specific assays below). Each day, the lux was measured and adjusted to the appropriate level for the assay being performed (Dr.meter LX1330B). Mice used in sociability assays were reared on an inverted light/dark schedule, with lights on at 7 p.m. and lights off at 7 a.m. Assays were performed under red light (Amazon Basics 60W Equivalent, Red) to minimize the stress-inducing effects of bright white light and to remain consistent with their inverted light/dark schedule. Behavioral assays in a given series were always separated by at least two days but never more than four days. On all days of behavioral experiments and handling, mice were retrieved from the facility and left in the behavior room to acclimate to the environment for at least 1 h. Once all mice in a cage completed the assay, all were returned to their original home cage.

Acquisition of behavior data for all anxiety-related assays and the three-chamber assay was recorded using Logitech C922x Pro Stream Webcams at 30 frames per second (fps) via the open-source UCLA miniscope software.[168] Acquisition of object and juvenile interaction data were recorded at 30 fps using a Teledyne Flea3 USB3 camera (Model: FL3-U3-13E4C-C: 1.3 MP, e2v EV76C560) via an in-house, python-based, open-source video acquisition software, REVEALS (https://github.com/CruzMartinLab/REVEALS).[162]

Throughout all components of behavioral assays and handling, gloves and a lab coat were worn. Gloves, behavioral arenas, and any relevant objects or cups used during the assay were sprayed with 70% ethanol in between handling mice or between each new mouse performing a given assay.

All behavioral assays were performed blind to condition, and analysis was performed via custom code written in MATLAB (MathWorks) (see behavior analysis below).

Handling

The first assay of each series was always preceded by three consecutive days of handling. Mice involved in anxiety-related assays were handled under standard, ambient room lighting (270 lux), and mice involved in sociability assays were handled under red light.

Anxiety-related assays

Anxiety-inducing arenas were custom-made as described by Johnson et al.[103]

Open field (OF)

Mice were placed in the center of a custom-made OF, a (45 × 45 × 38 cm, length x width x height) black arena under 200 lux of white light, and were free to explore for 10 min. The OF was used to measure locomotion by measuring the distance traveled by the mice.

Elevated zero maze (EZM)

The EZM is an elevated (63 cm) circular platform with a 5 cm track width and diameter of 60 cm. It is comprised of two closed arms with a wall height of 14 cm and two open arms that lack walls. The EZM was run under 200 lux of white light for 10 min.

Light-dark box (LDB)

The LDB uses the frame of the OF, but inserted into the OF is a black divider (45 × 38 cm, length x height) that divides the OF into two distinct zones 1/3 and 2/3 the width of the OF, but features a small passage-way at the bottom (7.6 × 7.6 cm, width x height) to allow the mice to move freely between zones. Over the smaller zone (45 × 15 cm, length x width) is a black lid that blocks all light: this is the dark zone. Because there is no lid over the remaining 2/3 of the OF (45 × 30 cm, length x width), this is the light zone. The LDB was run under 300 lux of white light for 10 min.

Novelty-suppressed feeding (NSF)

24 h before the start of experimentation, mice were transferred to a clean cage that possessed no food. During the assay, mice were placed in a novel, open arena (50 × 35.5 × 15 cm, length × width × height) with a single, fresh food pellet strapped down in the center of the arena with a rubber band. The experimenter watched the live video feed to observe when the mouse traveled to the center of the maze and began feeding on the food pellet, which concluded the assay. Simple investigation or sniffing of the pellet was not considered feeding. The NSF was the only hand-scored assay, and was done so by a trained, blinded experimenter. To measure the latency to feed, the researcher watched the trial back and determined the exact frame that the mouse first bit the pellet. In the rare event that the mouse did not eat the pellet in the time allotted (10 min recording), that mouse was excluded from the NSF analysis. The NSF was run under 200 lux of white light.

Cage NSF

Immediately following the NSF, mice were placed in a fresh cage with approximately 10 food pellets placed in one corner of the cage. Again, the latency to feed was recorded by the experimenter. The Fresh Cage NSF served to determine and verify the anxiety-inducing nature of the arena relative to the more familiar environment of a standard mouse cage.

Z-anxiety quantification

Z-Anxiety quantification was adapted from Guilloux et al.[63] For each individual assay, the mean (μ) and standard deviation (σ) of the relevant metric for that assay (e.g., EZM: time spent in open arms) for all WT animals was calculated. For any given mouse in any single assay, whose performance in that assay (e.g., EZM: time spent in open arms) is given by x, the Z score is the following:

$$z - score_{assay} = \frac{x - \mu}{\sigma}$$

To be consistent with a positive Z score being indicative of increased anxiety, the sign of the Z score in the EZM and LDB was multiplied by -1. In this way, less time spent in the open arms (EZM) or in the light zone (LDB), indicators of increased anxiety-like behavior, yielded positive Z score values. For the NSF, because an increased latency to feed was indicative of anxiety-like behavior, these z-scores were not multiplied by -1. Each animal's Z-Anxiety is simply an average across all three assays, given by the following:

$$Z - Anxiety = \frac{(z - score_{EZM} * -1) + (z - score_{LDB} * -1) + (z - score_{NSF})}{3}$$

For the sex-separated quantification of Z-Anxiety, the only modification made was that the *Z* score for each assay for all males was found in reference to the WT male average and standard deviation; likewise, z-scores for females were made in reference to the WT female average and standard deviation for each assay.

Sociability assays

Object and social interaction

Mice were habituated to the empty, clear arena (46 × 23 cm). Once 120 s elapsed, a single novel object made from two glued 6-well plates was temporarily secured at one end of the arena with a magnet. Mice were free to explore this object for another 120 s. After this time elapsed, the novel object was removed, and was immediately replaced by a novel, juvenile (3–5 weeks old), sex-matched CD-1 stimulus mouse. These mice were then free to interact with one another unencumbered for 120 s.

Three-chamber sociability assay

One day prior to the three-chamber assay, mice were habituated to the three-chamber apparatus (three 46 × 23 cm chambers connected by passageways 10 cm wide). These mice were free to explore the entire three-chamber arena with an empty wire-mesh pencil cup in each of the two end chambers for 5 min. On that same day, stimulus CD-1 mice were habituated to being placed underneath these wire-mesh pencil cups for 5 min. The next day, the three-chamber assay was performed as follows. A novel, juvenile, sex-matched CD-1 stimulus mouse was placed underneath a cup in the chamber at one end of the arena, and an empty cup was placed in the chamber at the other end of the arena. Weights sat on top of the cups to ensure that the CD-1 stimulus mouse was secure in the cup and that the experimental mouse would not move either cup. To begin the assay, dividers were placed in the three-chamber passageways to block movement between chambers, and the experimental mouse was placed in the center chamber. After the mouse explored the center chamber for 120 s, the inserts were removed, and the mouse was free to explore the entire three-chamber arena, as well as the empty cup and mouse cup, for 10 min. The chambers in which the mouse cup and empty cup were placed were alternated randomly across mice. The percent time spent in each of the three chambers was scored. The social index (SI) was found by taking the difference between the percent time spent in the mouse chamber and the percent time spent in the empty chamber and dividing it by the sum of the percent time spent in the mouse- and empty chambers.

Behavior analysis

In all behavioral assays (except for the NSF and Fresh Cage NSF), mice and relevant behavioral arena components were tracked using DeepLabCut (DLC).[169] To ensure the accuracy of tracking by DLC, a random sampling of videos from each day of experimentation was inspected. Next, a trained experimenter watched annotated videos to verify consistent tracking of fiducial points. Fiducial points included the snout, the nose bridge, the head, left and right ears, and five points that ran along the sagittal axis of the mouse body from the neck to the base of the tail. All corners of all arenas were labeled, as well as any relevant features of the arenas, including corners of objects and cups, and the thresholds separating the open and closed arms of the EZM. To calculate the interaction times, binary behavior matrices (vectorized behavior) indicating the location of the relevant key points of the mouse with respect to relevant key points of the arena (e.g., head of the mouse and corner of an object) were created using custom MATLAB scripts, available at (https://github.com/CruzMartinLab/PV-mC4_Project/tree/main/behavior_code).

Neonatal viral injections

To genetically tag and identify PV cells in electrophysiology experiments, P1-3 PV-mC4-WT and PV-mC4-KI pups were injected with 360 nL of AAV1-FLEX-tdTomato (titer: 2.5 × 1013 vg/mL, Addgene #28306) per cortical hemisphere. To identify PV cells in electrophysiology experiments involving PanN-mC4-WT and PanN-mC4-KI mice, P1-3 pups were injected with 360 nL of AAV9-S5E2-dTom-nlsdTom (titer: × 1013 vg/mL, Addgene #135630) per cortical hemisphere. Borosilicate pipettes (BF150-117-10, Sutter Instrument Co., Novato, California) were pulled to a fine tip (approximately 3–15 μm) and back-filled with mineral oil and inserted into the Nanoject Injector (Drummond, Nanoject II, 3-000-204/205A/206A). After cutting the tip of the pipette and emptying roughly half of the mineral oil, the pipette was filled with virus solution from the open tip. Prior to injection, pups were anesthetized via a cold-plate (approximately 15 min) and remained on the cold surface of an ice pack during injection to ensure continued anesthesia throughout the entire process. The mPFC was targeted along the anterior-posterior axis and hit consistently using empirically derived landmarks and the Allen Brain Atlas.[166] From here, the tip of the pipette was moved medially into position immediately adjacent to the midline. Injections at several depths were made to ensure effective labeling of the entire dorsal-ventral depth of mPFC target sub-regions. Fine spatial navigation of the tip was made using a stereotax (Kopf Instruments, Tujunga, California). Post-injection, pups recovered in a plastic chamber that was placed on top of a heated blanket. Pups were returned to the dam once fully recovered.

Electrophysiology

Acute slice preparation and recording

PV-mC4-WT and PV-mC4-KI mice (P40-62) and PanN-mC4-WT and PanN-mC4-KI mice (P42-55) were anesthetized with a 4% isoflurane-oxygen mixture (v/v) and perfused intracardially with ice-cold Perfusion/Slicing artificial cerebrospinal fluid (P/S-aCSF) bubbled with 95% O_2/5%

CO_2 containing the following (in mM): 3 KCl, 26 $NaHCO_3$, 1.25 NaH_2PO_4, 212 sucrose, 10 glucose, 0.2 $CaCl_2$, and 7 $MgCl_2$ (300–310 mOsm). Thirty min before slicing, 200 mL of P/S-aCSF was transferred to −20°C until turned to a slushy consistency. Coronal slices 300-μm thick were cut in this slushy P/S-aCSF using a VT1000 S (Leica) vibratome and were then transferred to a Recording aCSF (R-aCSF) solution bubbled with 95% O_2/5% CO_2 containing the following (in mM): 125 NaCl, 2.5 KCl, 25 $NaHCO_3$, 1.4 NaH_2PO_4, 16 glucose, 0.4 Na-ascorbate, 2 Na-pyruvate, 2 $CaCl_2$, and 1 $MgCl_2$ (300–310 mOsm). Slices were incubated in this R-aCSF for 30 min at 35°C before being allowed to recover at room temperature for 1 h prior to recording.

Whole-cell voltage- and current-clamp recordings were performed in Layer (L) 2/3 of the PrL, IL, and AC cortex divisions of the mPFC.[34] For all recordings, tdTomato-positive PV cells were identified using a Prior Lumen 200 Light Source (Prior Scientific) and a CMOS camera (Rolera-Bolt-*M*-12; 1.3 MP, Mono, 12-BIT, Uncooled, QImagingBolt) mounted on an Olympus BX51WI microscope (Olympus America, Inc.). Pyramidal neurons (PYRs) were identified based on morphological and electrophysiological properties. All recordings were performed at 29°C–31°C. Signals were recorded with a 5× gain, low-pass filtered at 6 kHz, and digitized at 10 kHz using a patch-clamp amplifier (Multiclamp 700B, Molecular Devices). Nearly all recordings were made using 3–5 MΩ borosilicate pipettes (Sutter, BF-150-117-10). Series (R_s) and input resistance (R_{in}) were monitored throughout the experiment by measuring the capacitive transient and steady-state deflection in response to a −5 mV test pulse, respectively. Liquid junction potentials were calculated and left uncompensated.

Miniature postsynaptic currents (mPSCs)

For recording miniature excitatory postsynaptic currents (mEPSCs), borosilicate pipettes were filled with an internal recording solution that contained the following (in mM): 120 Cs-methane sulfonate, 8 NaCl, 10 HEPES, 10 CsCl, 10 Na_2-phosphocreatine, 3 QX-314-Cl, 2 Mg^{2+}-ATP, and 0.2 EGTA (292mOsm, adjusted to pH 7.3 with CsOH). PV cells and PYRs were voltage clamped at −70 mV in the presence of tetrodotoxin (TTX, 1 μM, Tocris) and picrotoxin (PTX, 100 μM, HelloBio). 6–9 mice per sex per condition from 3 to 4 litters were used to collect all mEPSC data for PV cells and PYRs.

For recording miniature inhibitory postsynaptic currents (mIPSCs), borosilicate pipettes were filled with a high-chloride internal recording solution that contained the following (in mM): 60 Cs-methane sulfonate, 8 NaCl, 70 CsCl, 10 HEPES, 10 Na_2-phosphocreatine, 0.2 EGTA, and 2 Mg^{2+}-ATP (290 mOsm, adjusted to pH 7.3 with CsOH). PV cells and PYRs were voltage clamped at −70 mV in the presence of TTX (1 μM), CNQX (20 μM, Tocris), and DL-APV (50 μM, Tocris). Because this high-chloride internal solution has a chloride reversal potential of −13 mV, mIPSCs were inward. 4–6 mice per sex per condition from 3 to 5 litters were used to collect all mIPSC data for PV cells and PYRs.

mPSC analysis

mPSCs were identified and their amplitude, frequency, rise, and decay were determined using custom scripts written in MATLAB. At least 120 s were analyzed for each cell. All mPSC raw traces were first lowpass filtered in Clampfit (Molecular Devices) using a boxcar filter. Next, local minima in the trace were recognized by identifying potential synaptic events using the native *islocalmin()* MATLAB function. After these events were filtered, a series of steps were taken to remove false positives while simultaneously limiting the number of false negatives. More specifically, we calculated a threshold based on the standard deviation of the noise of the raw trace within a 1 s temporal window to differentiate the background noise from mPSCs, thus setting an amplitude threshold. Next, a series of thresholds based on the rise and decay times were used to filter subsequent postsynaptic events. For all remaining mPSCs, the amplitude is given as the difference between the baseline current value (determined using a highly smoothed line of the raw data that effectively serves as a moving baseline of the trace) at the time when the peak reaches a minimum current value and the average of the 10 points around the absolute minimum of that mPSC peak.

Frequency (in Hz) of postsynaptic events is given by the number of mPSCs per second. $Rise_{10\text{-}90}$ is defined as the time (ms) it takes for the mPSC to progress from 10 to 90% of the peak of that mPSC. To find the $Decay_{tau}$, for each event, the trace from the peak of the mPSC to its return to baseline is isolated and fit to a single-term exponential.

Between groups, differences in R_s values for each cell type were not statistically significant. R_s for PV cells in PV-mC4-WT and PV-mC4-KI mice (mEPSCs) were as follows (in MΩ): WT males: 16.85 ± 1.17; WT females: 17.35 ± 1.26; KI males: 16.27 ± 1.33; KI females: 15.56 ± 1.21. R_s for PV cells (mIPSCs) were as follows (in MΩ): WT males: 15.79 ± 1.06; WT females: 13.93 ± 1.09; KI males: 15.40 ± 1.46; KI females: 14.07 ± 0.79. R_s for PYRs (mEPSCs) were as follows (in MΩ): WT males: 15.94 ± 0.92; WT females: 14.81 ± 0.75; KI males: 15.07 ± 0.73; KI females: 15.00 ± 0.80. R_s for PYRs (mIPSCs) were as follows (in MΩ): WT males: 14.43 ± 1.05; WT females: 13.81 ± 0.92; KI males: 16.13 ± 1.34; KI females: 14.88 ± 1.26. R_s for PV cells in PanN-mC4-WT and PanN-mC4-KI mice (mEPSCs) were as follows (in MΩ): PanN-mC4-WT: 15.24 ± 1.28; PanN-mC4-KI: 14.11 ± 1.34.

Active and passive properties

To determine the active and passive properties of PV cells and PYRs, borosilicate pipettes were filled with an internal solution that contained the following (in mM): 119 K-gluconate, 6 KCl, 10 HEPES, 0.5 EGTA, 10 Na_2-phosphocreatine, 4 Mg^{2+}-ATP, and 0.4 Na-GTP (292 mOsm, adjusted to pH 7.3 with KOH). Cells were held at −65 mV during recording, and the bath was perfused with CNQX (20 μM), DL-APV (50 μM), and PTX (100 μM). Excitability was assessed by measuring membrane voltage changes (i.e., current-evoked Action Potentials (APs)) to a spiking protocol that applied 500 ms square current pulses to the patched cell, beginning at −250 pA and increasing in 30 pA steps to a max current injection of 470 pA. Passive properties of the patched cells were determined via a 500 ms, −20 pA square pulse that preceded the square pulse of increasing current amplitude. This protocol was run and recorded 2–3 times per cell, and final values were averaged across recordings for each cell. 5–7 mice per sex per condition from 4 to 5 litters were used to collect all active and passive properties data for PV cells and PYRs.

Active properties analysis

To quantify spike frequency (Hz), the number of spikes (temporally defined as when the rising phase of the spike crossed 0 mV) was divided by the length of the current pulse (0.5 s). Rheobase was defined as the minimum current injection that evoked at least a single AP. The inter-spike interval (ISI) was determined by finding the difference (in ms) between the crossing of 0 mV of one spike and the crossing of 0 mV by the next spike. To capture time-dependent changes in the frequency of APs, ISI 1/9 and 4/9 were determined by dividing the first ISI by the fourth and ninth ISI, respectively. ISI ratios were taken from the first sweep with at least 10 spikes. To determine the threshold voltage (V_{thresh}) for an AP, for all spikes at each current injection, the derivative of the membrane voltage was taken across time to find the inflection point that corresponded with the beginning of the rising phase (i.e., threshold). Threshold voltages for all spikes were then averaged to arrive at a single value of V_{thresh}. Reset voltage (V_{reset}) was defined as the minimum voltage value between spikes. A single value for V_{reset} was obtained in the same way as was done for V_{thresh}.

Passive properties analysis

To obtain the R_{in}, the difference between the baseline voltage (holding membrane voltage of approximately −65 mV) and the average voltage response to a −20 pA injection (measured at steady state) was divided by that current injection value of 20 pA. The membrane time constant, $\boldsymbol{\tau}_m$, was the fitted response to the −20 pA injection. Membrane Capacitance (C_m) was determined by dividing $\boldsymbol{\tau}_m$ by the R_{in}. The resting membrane potential (V_m) was measured as the potential before any current was injected. Finally, the Voltage Sag Ratio was determined by dividing the difference between the minimum voltage at the peak deflection to a −500 pA current injection and the voltage of the steady-state response by the difference between the minimum voltage at the peak deflection and the baseline voltage.

Electrophysiological data were analyzed using custom routines written in MATLAB, available at (https://github.com/CruzMartinLab/PV-mC4_Project/tree/main/ephys_code).

Computational model

Model neurons

Using the DynaSim toolbox,[69] PYR and PV cells for each of the four networks – PV-mC4-WT and PV-mC4-KI male, and PV-mC4-WT and PV-mC4-KI female – were modeled as leaky integrate-and-fire neurons whose membrane voltage, V_m, as a function of time, t, were given by the following:

$$\frac{dV_m}{dt} = \frac{(E_L - V_m) - R_m g_{sra}(V_m - E_K) - R_m i_{syn} + R_m i_t}{\tau_m} \qquad \text{(Equation 1)}$$

where E_L is the equilibrium potential, R_m is the membrane resistance, g_{sra} is the spike-rate adaptation, E_K is the potassium reversal potential, i_{syn} is the synaptic input, i_t is the applied current, and $\boldsymbol{\tau}_m$ is the product of R_m and membrane capacitance (C_m). Values used for E_L, R_m, E_K (−102 mV), and C_m were derived from the experimental data, and differed from network to network only when there was a significant difference in the value of that variable between WT and KI mice overall or within-sex. If no significant difference was identified in a given parameter, the average across all sexes and conditions was taken and used uniformly across all networks.

Establishing model neurons

For each of the four conditions, and by extension, each of the four networks, a single model PYR and single model PV cell were generated. To create each model neuron, a waveform (i_t) was matched to a subsection of the spiking protocol used during the experiment. The i_t waveform consisted of 17 sweeps of a square current pulse (500 ms) beginning at −10 pA, increasing in 30 pA steps, and finishing at 470 pA. From here, firing rates were extracted to construct frequency-current (FI) curves for each model cell that were used to compare to the experimental FI curves. An additional term, $R_m{*}i_{std}$, was added to the numerator of Equation 1. This term served to shift the baseline voltage from V_m to −65 mV during the simulation, replicating the experimental conditions of current clamp under which the experimental data were acquired. i_t was multiplied by a scale factor, I_{act}, representing active conductances and other intrinsic excitability properties, which improved the fitting of the modeled FI curve to that of its experimental counterpart. This same scale factor was used for i_{syn} to model the changes in intrinsic excitability. Reset voltage (V_{reset}) and threshold voltages (V_{thresh}) were determined experimentally, and the selection of the specific values used in each model cell followed the same logic as that for E_L, R_m, and C_m. An increase in V_m above V_{thresh} constituted a spike, and V_m was then reduced to V_{reset} for an absolute refractory period, t_{ref}, of 1 ms.

For all PYR and PV cells, spike rate adaptation time constants ($\boldsymbol{\tau}_{sra}$) were set to 100 and 5 ms, respectively, reflecting the strong adaptation observed in regular-spiking PYRs and nominal levels of adaptation in fast-spiking PV cells.[170–172] Implementation of spike-rate adaptation was accomplished by the following[173]:

$$\frac{dg_{sra}}{dt} = -\frac{g_{sra}}{\tau_{sra}} \qquad \text{(Equation 2)}$$

$$g_{sra} \rightarrow g_{sra} + \Delta g_{sra} \qquad \text{(Equation 3)}$$

Moreover, spike-rate adaptation conductance was increased by an increment, Δg_{sra}, which returns to zero in time τ_{sra}.[174] All model cells closely matched their experimental counterparts.

Establishing networks

Simulating network noise. All PYR and PV model cells received random input to simulate network noise at levels that caused these model cells to fire at typical spontaneous rates observed experimentally, 3–4 Hz for PYRs and 28–35 Hz for PV cells.[175,176] For each simulation, a random number of brief current pulses within a specified range to evoke the aforementioned basal firing rates was selected for PYR and PV model cells. Moreover, for each simulation, the time at which these pulses were applied to each cell were randomized as well.

Network architecture. Individual networks were built to simulate WT male, KI male, WT female, and KI female conditions. For each of the four networks, fifteen 3 s simulations were run, the simulations serving as our statistical replicates.

Each network consisted of a PYR and PV circuit in a generalized input and output layer. In the input layer, PYR1 and PV1 simultaneously received an identical applied current, $i_{t.}$ In all network simulations, i_t consisted of a 4 Hz, fixed-amplitude sine wave atop the final 2 s of a 2.5 s, 50 pA DC component. The use of a non-varying DC component combined with a phasic sine wave input was used here to model dynamic input in an interpretable way[177,178] while preserving biological relevance[179–182] in our model. The first and final 250 ms of each simulation had no applied current. For all data plotted, only the 2 s in which the sine wave was applied was considered for analysis. Each of the fifteen simulations for a given network contained three trials in which the only variable altered was the peak of the sine wave (i.e., the peak of the applied current, i_t): 200, 275, and 350 pA.

With respect to network connectivity, PYR1 synapses onto both PYR2 and PV2, in the output layer. PV1 synapses onto PV2. PV2 synapses onto PYR2. This specific feedforward arrangement was selected such that all four basic connectivity sub-types (E– > E, E– > I, I- > E, and I- > I) sampled experimentally via mEPSCs and mIPSCs recorded in both PYR and PV cells could be included and thus be leveraged to understand better the effects of increased levels of mC4 in PV cells on the firing properties of model neurons. This feedforward network architecture is an adaptation of that used by Nocon et al.,[183] but was further modified using arrangement principles similar to those used by Seay et al.[184] and Moore et al.[185] Notably, our model lacks feedback circuitry and classical inhibitory action of other interneuron types, and favors single synapses over a population construction. Motivating these explicit simplifications for our current model was the benefit of interpreting the changes in the output model cells and acknowledging that the experimental data upon which many aspects of the model are founded come from *ex vivo*, rather than *in vivo*, data.

Synaptic connectivity. To model postsynaptic currents (PSCs), after first setting all synaptic weights to the same fixed value across all four networks, weights were altered by adjusting the conductance of the inputs only where there were significant changes in the experimental mEPSC and/or mIPSC data recorded in PYR and PV cells. These weights were adjusted by the same percent change as that observed in the mEPSC or mIPSC frequency or amplitude of the experimental data. In line with previous models,[174,183,184] short-term depression was employed in all synapses. PSCs were modeled via the difference of two decaying exponential functions[183] featuring time constants where $\tau_1 > \tau_2$:

$$s(t) = B\left(e^{-\frac{t}{\tau_1}} - e^{-\frac{t}{\tau_2}}\right)u(t) \qquad \text{(Equation 4)}$$

where B is a normalization constant, s = 1 at maximum, and u(t) is the unit step. From here, s can be represented by the following two ordinary differential equations:

$$\frac{ds}{dt} = \frac{\left(\frac{\tau_2}{\tau_1}\right)^{\frac{\tau_1}{\tau_2 - \tau_1}} * x - s}{\tau_2} \qquad \text{(Equation 5)}$$

$$\frac{dx}{dt} = -\frac{x}{\tau_1} \qquad \text{(Equation 6)}$$

When a presynaptic spike is detected by a postsynaptic cell, x (spike inputs to that postsynaptic cell) is increased by P – representing synaptic strength – which is then reduced by f_p, a fraction of its value.[174,183]

$$x \rightarrow x + P \qquad \text{(Equation 7)}$$

$$P \rightarrow (1 - f_p)P \qquad \text{(Equation 8)}$$

Recovery of P to 1 is defined by the time constant, τ_p, where:

$$\frac{dP}{dt} = -\frac{(1 - P)}{\tau_p} \qquad \text{(Equation 9)}$$

PSC rise (τ_1) and decay (τ_2) kinetics were derived from experimental values. Values used for f_p and τ_p were the same as those in Nocon et al.[183] In total, PSCs were modeled as:

$$i_{syn}(V_m, i) = g_{syn} \times s \times (V_m - E_{syn}) \times netcon \qquad \text{(Equation 10)}$$

where g_{syn} is synaptic conductance, s is the time-dependent PSC defined above, E_{syn} is the reversal potential of the synaptic conductances, and netcon is a binary connectivity matrix in which rows represent sources and columns represent targets.

Additional network noise. An increase in network-level noise in response to suppression of PV cells has been directly demonstrated by multiple groups.[5,186,187] After using our model to demonstrate PV cell hypoactivity in the male KI network, the basal network noise (3–4 Hz) delivered to PYR2 exclusively was increased by a factor of 1.5×.[183] This increase in the mean firing rate of PYR2 – representing an increase in network noise in response to PV cell hypoactivity – has been used in previous models[183] and was set in order to match *in vivo* experimentally derived changes in basal firing rates in response to PV suppression.[5]

Analysis of network parameters

For each of the four networks and the three peak values of the applied current, analysis was performed on 15 independent simulations.

Firing rate (FR). The firing rate was calculated as the average number of spikes per second (Hz) during the 2 s in which the sine wave stimulus of the applied current occurred.

Transfer Entropy (TE). TE is a metric used to determine connectivity in complex networks, which is considered to describe the effective flow of information between neurons.[163,188] To determine the dependency of the spike train of PYR2 or PV2 on the spike train of PYR1 more directly, we calculated the TE[148] using a MATLAB Toolbox.[163]

PYR1xPV2 latency. Custom scripts written in MATLAB were used to determine the PYR1xPV2 latency. For each simulation, for each spike occurring in PYR1, the time (in ms) to the nearest spike in PV2 that followed the spike in PYR1 was calculated. The mean latency and latency standard deviation were calculated by averaging- or taking the standard deviation of, respectively, all latencies for a given simulation.

QUANTIFICATION AND STATISTICAL ANALYSIS

All statistical analyses were completed in GraphPad Prism 8.0, and the threshold for significance for all tests was set to 0.05 ($\alpha = 0.05$). Full statistical reports for all plots are available in the Statistical Supplement document. Briefly, all behavior and electrophysiology plots representing sex-pooled data (WT males and females as one group being compared to KI males and females together as a second group) were analyzed by t-tests, t-tests with Welch's correction, or Mann-Whitney tests. Moreover, all behavior and electrophysiology plots representing sex-separated data were analyzed by two-way ANOVA's with a Šídák's multiple comparisons test only executed when appropriate (interaction and/or main effects $p < 0.05$). Cumulative frequency plots were analyzed with a Kolmogorov-Smirnov (KS) test. Frequency-current (FI) curves were analyzed using Repeated Measure Two-way ANOVAs. PV cell density was analyzed using a Mann-Whitney test. MFISH data were analyzed by Mann-Whitney tests or Two-way ANOVAs with Šídák's multiple comparisons. Computational data were analyzed by Two-way ANOVAs with Šídák's multiple comparison tests (firing rate and latency plots) and by Repeated Measure Two-way ANOVAs (transfer entropy plots). For all statistical analyses relating to the computational model, any $p < 0.05$ was denoted in the figure by a '#' sign – exact *p*-values can be found in the Statistical Supplement document. Figures were prepared using CorelDRAW Graphics Suite X8 (Corel Corporation) and ImageJ (NIH). Data are presented as the mean ± SEM, unless otherwise noted.